# Squeezing in Optical Fibers

by

Luc Boivin

Submitted to the Department of Physics
in partial fulfillment of the requirements for the degree of

Doctor of Philosophy

at the

MASSACHUSETTS INSTITUTE OF TECHNOLOGY

February 1996





Author ..... .....
Department of Physics
December 6 1995

Certified by..... .....
Hermann A. Haus
Institute Professor
Thesis Supervisor

Certified by. .....
John W. Negele
W. A. Coolidge Professor of Physics
Thesis Supervisor

Accepted by ..... .....
George F. Koster
Chairman, Departmental Committee on Graduate Students

# Squeezing in Optical Fibers

by

Luc Boivin

Submitted to the Department of Physics
on December 6 1995, in partial fulfillment of the
requirements for the degree of
Doctor of Philosophy

## Abstract

The generation of squeezed radiation in single-mode optical fibers is discussed. A self-consistent theory for the quantum propagation of pulses in dispersive and Raman active fibers is developed. A numerical implementation of the corresponding linearized noise theory is presented. This code was used to design a new fiber squeezer operating at $830nm$. A closed-form solution to the nonlinear, stochastic and integro-differential equation for the quantum envelope is found at zero dispersion. We use this solution to study the resonance-fluorescence spectrum of a fiber excited by a monochromatic laser field. We also evaluate the mean field and the squeezing level for fiber lengths where the linearized approximation is no longer valid. The predictions of this continuous-time theory are compared with those of the discretized-time model. We show that quantum revivals predicted by the latter are spurious. We show that the linearized approximation in the soliton regime is valid for nonlinear phase shifts up to $n_0^{1/4}$. The noise of the four soliton operators is shown to be minimized in a Poisson-Gaussian soliton state. We propose a new method for generating squeezed vacuum using a low birefringence fiber. This method relies on cross-phase modulation between modes with orthogonal polarizations, and does not require a interferometric geometry. We predict the nonlinear depolarization of an intense linearly polarized pulse coupled into a low birefringence fiber due to its interaction with quantum noise. Finally, progress in the construction of a fiber squeezer driven by a high repetition rate modelocked Ti:Sapphire laser is reported.

Thesis Supervisor: Hermann A. Haus
Title: Institute Professor

Thesis Supervisor: John W. Negele
Title: W. A. Coolidge Professor of Physics

# Acknowledgments

My stay at MIT has been a truly enjoyable experience, in large part because of the people I had the chance to work with in the Ultrafast Optics Group. This group provided a nurturing environment that I shall miss dearly. I would like to express my deepest gratitude to Professor Hermann Haus for his guidance, his advice as well as for his many contributions to the present thesis. His warm and energetic manners enhanced the pleasure of working with such an insightful and inquisitive person. Professor Haus embodies for me the spirit of the true scholar, seeking knowledge beyond the narrow boundaries set by academic departments. I would also like to acknowledge Professor E. P. Ippen who, together with Professor Haus, created for me numerous opportunities which have expanded the frontiers of my knowledge and moved my career ahead. I am also indebted to Dr. Franz. X. Kärtner who patiently introduced me to optics and to quantum optics. Franz's incredible resourcefulness in dealing with complex problems and his optimistic attitude toward work rekindled my love of physics at a time when I badly needed it. I am also grateful to Chris R. Doerr who thought me everything I know about experimental quantum optics. Chris also initiated the numerical work on dispersive squeezing and was kind enough to make me beneficiate from his experience. I am grateful to Prof. J. H. Shapiro for graciously making me a co-author of his paper on four-wave mixing and for supporting me in my career. I would also like to thank Prof. Negele for easing my transition to optics. I appreciated his insight on the quantum nonlinear Schrödinger equation. I acknowledge the help of Dr. Bret Bouma in modelocking my laser. Bret also lended me his titanium-sapphire laser and helped me with the positive dispersion squeezing experiment. I thank Lynn Nelson for her help in setting up my laser and with whom I had the pleasure to share a lab for a few months. I also thank Dave Dougherty for sharing with me his insight on Raman gain. Finally, I am indebted to my wife Julie de Sève who's love and companionship supported me during all my studies at MIT.

Ce mémoire est dédié à Julie de Sève

# Contents

# List of Figures

# Chapter 1

# Introduction

## 1.1 Quantum Noise

One of the most profound result of quantum mechanics is the fact that any system, no matter how carefully prepared, displays a minimum amount of randomness. This element of uncertainty manifests itself, for example, when two "non-compatible" (i.e. non-commuting) measurements are performed on identically prepared systems. The theory predicts that the outcome of at least one of these two types of measurements cannot be predicted with certainty. This conclusion has challenged the minds of three generations of physicists since its precise formulation by W. Heisenberg in 1927 [1]. The Heisenberg uncertainty principle takes the form of a constraint on the *product* of the variances of non-compatible variables. For that reason, it does not prevent a single variable from having a well-defined value and a predictable behavior under measurement. In general however, the price to pay to reduce the uncertainty on one variable of a system is an increase in the uncertainty of the variables that do not commute with it.

A squeezed state of a quantum system can loosely be defined as one for which the uncertainty on one of the dynamical variables is inferior to what one would expect from a uniform distribution of quantum noise according to the Heisenberg principle. A more precise definition in the context of quantum optics will be given in the next chapter. It appears from the above definition however that squeezed states are quite

familiar objects in quantum theory. Indeed, according to our definition, an eigenstate of any observable is a squeezed state since the outcome of a measurement of that observable gives a predictable result. According to the von Neumann postulate, an ideal measurement in quantum mechanics results in an eigenstate of the observable being measured. Hence it appears that the generation of squeezed states can be realized easily when an ideal measuring device is available.

## 1.2 Squeezed Light

Squeezed states of the electromagnetic field have been the focus of considerable research over the last twenty five years [2, 3, 4, 5, 6]. Each mode of this field can be thought of as a quantized harmonic oscillator with non-commuting "position" and "momentum" operators. These operators, when properly normalized, are referred to as quadratures. As will be explained in Chapter 2, the definition of a quadrature can be extended when several modes of the electromagnetic field are considered. States of light for which the level of quantum fluctuations of at least one quadrature of the field is inferior to the level observed in vacuum are called quadrature-squeezed states. These states constitute the main topic of this thesis. A particularly important role will be played by squeezed vacuua, which are quadrature-squeezed states with no coherent excitation.

The special interest devoted to the electromagnetic field is justified for two reasons. First, most physical systems are affected, in one way or another by this field. The interaction of the quantized Maxwell field with atomic systems thus leads to a rich array of phenomena in laser physics, in spectroscopy and in statistical mechanics. Squeezed light provides new initial conditions from which this light-matter interaction can be studied. Although several new effects have been predicted in the last decade [7, 8, 9, 10, 11, 12, 13, 14, 15], no experiment has yet been reported confirming these new phenomena. The possibility to demonstrate experimentally new physical phenomena arising from the interaction of squeezed light with matter has a strong appeal. Very few groups around the world have pushed in this direction, in large part

because of the difficulties associated with squeezed light generation. For this reason, this field still offers many opportunities for new discoveries.

The main engineering motivation for the experimental research on squeezed light has been its potential in high precision measurements. Interferometric schemes are ubiquitous in spectroscopy and in the measurement of the optical properties of partially transmitting samples. Interferometers also have numerous applications as ultra-sensitive motion sensors, like gyroscopes and vibration monitoring devices. For a number of reasons, these systems sometimes need to operate with short integration times or with low light levels. In such conditions, interferometers rapidly become limited by the quantum noise of the electromagnetic field. This noise puts a lower bound on the magnitude of a signal that can be detected and therefore limits the sensitivity of the interferometer. Caves showed in 1981 how one could use squeezed vacuum to overcome this so-called standard quantum limit[16]. A number of experiments based on Caves's original idea have been implemented in several laboratories, including MIT [17, 18, 19, 20]. Other improvements in measurement sensitivity based on the use of squeezed vacuum include frequency-modulation spectroscopy[21] which was demonstrated experimentally at Caltech[22], and imaging of faint phase objects[23] which was not yet observed. The hope to use squeezed light to operate an optical fiber gyroscope [24, 25] has been the main motivation for the funding and the research done on squeezed states at MIT and is an ongoing project in our group.

## 1.3 Generation of Squeezed Vacuum

As the previous discussion indicates, a squeezer aiming at improving the signal-to-noise ratio of an interferometer must produce a squeezed vacuum. As it turns out, the generation of these quantum states has not been as easy as the discussion of Section 1.1 might suggest. In fact, no ideal quantum measuring device for the quadrature of the electromagnetic field exists. Most measurements of the optical field involve photodetectors which absorb the photons being detected and therefore destroy the state of the field. One cannot therefore prepare a quadrature eigenstate as one would,

for example, prepare a spin eigenstate using a Stern-Gerlarch apparatus. Up to now, all generation schemes for squeezed light have relied on some form of parametric process in nonlinear optical media. The various squeezers demonstrated in laboratory can be divided in two broad categories, depending on the nature of the nonlinear material used. The most widely studied squeezers use $\chi^{(2)}$ materials which mediate interactions involving three photons. These crystals can convert, for example, one high frequency photon into two photons of longer wavelengths, as in parametric amplification[26]. They can also be used to mediate the inverse process where two low frequency photons combine to produce a high energy photon. This property is routinely used, for example, to produce blue light from semiconductor lasers operating around $0.9\mu m$. Squeezed vacuum generation has been observed in both parametric amplification[27, 28] and second harmonic generation [29]. In both cases, a squeezed vacuum can be obtained by driving the crystals just below the threshold for the emission of coherent radiation. A detailed discussion of the mechanism responsible for the compression of quantum noise in these systems is outside of the scope of this thesis. The impact of optical nonlinearities on quantum noise will however be made plausible in Chapter 3. A number of excellent reviews can be found which address the $\chi^{(2)}$ squeezers specifically[30].

The second class of squeezers uses the $\chi^{(3)}$ nonlinearity of fused silica or of semiconductors. Although fused silica has a very small Kerr coefficient, powerful optical pulses focused on meter-long optical fibers with diameters on the micron scale can result in significant nonlinear effects. Fiber squeezers based on the Sagnac interferometer design[31] were first demonstrated at MIT[32, 33, 35] and IBM[34]. The use of semiconductor waveguide in Sagnac squeezers was also investigated recently[38, 36, 37]. The Kerr effect in these devices is several orders of magnitude larger than in fused silica, so that very short squeezer can in principle be built. The detrimental effect of guided acoustical wave Brillouin scattering (GAWBS) can in principle be eliminated in this case. To avoid excess losses due to two-photon absorption, the carrier frequency of the pulses is chosen below half the transition frequency corresponding to the bandgap energy of the semiconductor.

## 1.4 Objectives and Organization of this Thesis

This thesis will provide a thorough discussion of the equations describing the evolution of quantum noise in Kerr waveguides. Particular emphasis is given to the description of pulses short enough to experience stimulated Raman scattering and to dispersion regimes where no analytic solution of the field equations can be found.

Chapter 2 introduces basic concepts and definitions related to squeezed states. The measurement of squeezing levels for optical pulses using balanced homodyne detection is reviewed in that chapter. Section 3.1 reviews the operation of the Sagnac loop squeezer[31]. The linearized theory of self-phase modulation is presented in Section 3.2. Our treatment includes a response function for the Kerr nonlinearity and a Raman noise source. The main goal of this thesis was to develop ways to overcome the 5 $dB$ noise floor affecting the experiment of Bergman *et al* [32, 33]. It turns out that operating the Sagnac squeezer at wavelengths where fused silica is dispersive makes it possible to overcome this saturation. Section 3.3 outlines the numerical approach used to study dispersive squeezing using parametric Green's functions.

Section 4.1 presents a self-consistent quantum theory of Raman-active waveguides that we developed. The exact relation between the response function and Raman noise is explained. Section 4.2 investigates the dispersionless regime where the nonlinear stochastic field equation can be solved in closed-form. This solution is used to analyze the resonance-fluorescence spectrum of fused silica, the evolution of the mean-field and the squeezing of quantum noise beyond the linearized approximation. These predictions are compared with those obtained from a coarse-grained time model. Section 4.3 investigates in more details the relation between the linearized and exact theories.

Chapter 5 deals with the quantized solitons of the nonlinear Schrödinger equation. These states of bound photons form in standard optical fibers at wavelengths longer than $1.3\mu m$. We consider Poisson-Gaussian superpositions of Bethe eigenstates for this equation (Section 5.2). We evaluate the soliton squeezing level at large nonlinear phase shifts for these states and we probe the domain of validity of the the linearized

theory (Section 5.3). In Section 5.4, we compare the noise properties of Poisson-Gaussian solitons with those of coherent states with identical initial mean fields. We show in particular that contrary to the latter, Poisson-Gaussian soliton minimize the fluctuations of the four collective soliton operators.

As part of this thesis, a new method to generate a squeezed vacuum in a fiber was developed. This method presented in Section 6.1, uses cross-phase modulation (XPM) between a linearly polarized pump and the vacuum fluctuations of the modes polarized perpendicularly in a low-birefringence fiber. This technique avoids the interferometric geometry used in Sagnac squeezers. Polarization XPM squeezing has not yet been demonstrated experimentally. Section 6.2 discusses the depolarization caused by the interaction of a linearly polarized pulse with quantum noise in a low-birefringence fiber. We predict a power-dependent depolarization rate depending on the square of the propagation distance.

Chapter 7 reviews progress in the ongoing construction of a new Sagnac squeezer at $830nm$, of a high repetition rate Ti:Sapphire laser and of a balanced detector. Chapter 8 summarizes the results presented in this thesis and suggests avenues for further investigations.

# Chapter 2

# Squeezed States of the Electromagnetic Field

This chapter introduces basic concepts and definitions that will be useful in later chapters. In Section 2.1, the quadrature operators of a single harmonic oscillator are defined. These operators are used to describe the electric field of a single mode of Maxwell's equations. Coherent states and squeezed states are then defined and their noise properties are considered. An experimental definition of squeezed states in terms of balanced homodyne detection is also given. In Section 2.2, quadrature operators and squeezed states are generalized to the multimode case corresponding to pulsed optical excitations. Pulsed squeezed states will be the main topic of subsequent chapters. More complete discussions of squeezed states can be found in the original paper of Yuen [2] or in the recent book by Walls and Milburn[30].

## 2.1 Single-Mode Squeezed States

### 2.1.1 Quadratures

Consider a system with non-commuting observables $\hat{X}_1$ and $\hat{X}_2$. Let $\left\langle \Delta^2 \hat{X}_1 \right\rangle$ and $\left\langle \Delta^2 \hat{X}_2 \right\rangle$ denote the variances for a series of measurements of these two operators

performed on identically prepared systems

$$\left\langle \Delta^2 \hat{X}_i \right\rangle \equiv \left\langle \hat{X}_i^2 \right\rangle - \left\langle \hat{X}_i \right\rangle^2, \tag{2.1}$$

for $i = 1, 2$. The Heisenberg uncertainty principle implies that the product of theses variances satisfies the inequality [39]

$$\left\langle \Delta^2 \hat{X}_1 \right\rangle \left\langle \Delta^2 \hat{X}_2 \right\rangle \geq \frac{1}{4} \left| \left\langle [\hat{X}_1, \hat{X}_2] \right\rangle \right|^2. \tag{2.2}$$

A familiar example of this inequality arises in the context of a quantized particle with position $\hat{X}$ and momentum $\hat{P}$. The commutator of these two operators being $i\hbar$, we find that the product of their variances must be larger than $\hbar^2/4$.

Consider a single quantized harmonic oscillator with annihilation operator

$$\hat{a} = \sqrt{\frac{m\omega}{2\hbar}} \hat{X} + i \sqrt{\frac{1}{2m\hbar\omega}} \hat{P}. \tag{2.3}$$

From the commutator of $\hat{X}$ and $\hat{P}$, we find

$$[\hat{a}, \hat{a}^\dagger] = 1. \tag{2.4}$$

The quadrature operators, $\hat{Q}(\theta)$, for this system are defined as linear combinations of $\hat{a}$ and $\hat{a}^\dagger$ parameterized by a phase $\theta$

$$\hat{Q}(\theta) = \frac{e^{-i\theta}\hat{a} + e^{i\theta}\hat{a}^\dagger}{\sqrt{2}}. \tag{2.5}$$

The normalization factor was chosen such that

$$\left[ \hat{Q}(\theta), \hat{Q}\left(\theta + \frac{\pi}{2}\right) \right] = i. \tag{2.6}$$

Using this expression and the general form of the Heisenberg inequality, we find

$$\left\langle \Delta^2 \hat{Q}(\theta) \right\rangle \left\langle \Delta^2 \hat{Q}\left(\theta + \frac{\pi}{2}\right) \right\rangle \geq \frac{1}{4}. \tag{2.7}$$

From (2.3) and (2.5), $\hat{Q}(0)$ and $\hat{Q}(\pi/2)$ are seen to be proportional to $\hat{X}$ and $\hat{P}$ respectively. Contrary to these operators however, the quadratures are dimensionless. The Heisenberg inequality (2.7) has therefore a more symmetric interpretation. Quadratures corresponding to arbitrary phases $\theta$ are linear combinations of $\hat{X}$ and $\hat{P}$. Any pair of quadratures with phases differing by ninety degrees can provide the two independent degrees of freedom of the oscillator. The Hamiltonian for example takes the form

$$\hat{H} = \frac{\hbar\omega}{2}\left\{\hat{Q}^2(\theta) + \hat{Q}^2(\theta + \pi/2)\right\}, \tag{2.8}$$

for any $\theta$. We note here that the quadratures being Hermitean operators, they can be measured, at least in principle. We will present in Section 2.1.4 an explicit measurement apparatus for these operators in the context of optical fields.

### 2.1.2 Quantized Electromagnetic Modes

The quantized harmonic oscillator is the fundamental building block of quantum electrodynamics. Each mode of the electromagnetic field is a quantized oscillator and can be described by a pair of non-commuting quadratures. As a result this field is affected by quantum noise which originates from the impossibility of specifying simultaneously the state of these quadratures.

Consider the electric field operator corresponding to one mode of Maxwell's equations in a cubical volume $V = L^3$. Assuming periodic boundary conditions, we have[30]

$$\hat{E}(\hat{\mathbf{r}}, t) = \sqrt{\frac{\hbar\omega}{\epsilon_0 V}}\left[\hat{Q}(0)\cos(\omega t - \mathbf{k}\cdot\mathbf{r}) - \hat{Q}\left(\frac{\pi}{2}\right)\sin(\omega t - \mathbf{k}\cdot\mathbf{r})\right], \tag{2.9}$$

where $\omega = c\,|k|^2$, and

$$k_x = \frac{2\pi n_x}{L}, \quad k_y = \frac{2\pi n_y}{L}, \quad k_z = \frac{2\pi n_z}{L}, \tag{2.10}$$

are obtained from the integers $n_x$, $n_y$ and $n_z$. The variance of this operator in a

general quantum state is given by

$$\left\langle \Delta^2 \hat{E}(\mathbf{r},t) \right\rangle = \left(\frac{\hbar\omega}{\epsilon_0 V}\right)\left\{\left\langle \Delta^2 \hat{Q}(0)\right\rangle \cos^2(\omega t - \mathbf{k}\cdot\mathbf{r}) + \left\langle \Delta^2 \hat{Q}\left(\frac{\pi}{2}\right)\right\rangle \sin^2(\omega t - \mathbf{k}\cdot\mathbf{r}) - \mathrm{Cov}\left(\hat{Q}(0), \hat{Q}\left(\frac{\pi}{2}\right)\right)\sin(2\omega t - 2\mathbf{k}\cdot\mathbf{r})\right\}. \quad (2.11)$$

In this expression, we defined the covariance of two operators, $\hat{A}$ and $\hat{B}$, as the symmetric combination

$$\mathrm{Cov}\left(\hat{A},\hat{B}\right) = \frac{\left\langle \hat{A}\hat{B} + \hat{B}\hat{A}\right\rangle}{2} - \left\langle \hat{A}\right\rangle\left\langle \hat{B}\right\rangle. \quad (2.12)$$

Expression (2.11) indicates that the variance of the electric field at a given point varies periodically at twice the optical frequency. Below, we consider this expression in more detail for coherent and squeezed states.

### 2.1.3 Coherent States and Squeezed States

The coherent states of an harmonic oscillator are defined as eigenstates of the annihilation operator [39]

$$\hat{a}\,|\alpha\rangle = \alpha\,|\alpha\rangle. \quad (2.13)$$

Since $\hat{a}$ is not Hermitean, its eigenvalues $\alpha$ are complex numbers. The vacuum state is clearly a coherent state with $\alpha = 0$. The variance of a series of quadrature measurements for a system in a coherent state is

$$\left\langle \Delta^2 \hat{Q}\right\rangle = \frac{1}{2}, \quad (2.14)$$

which is independent from $\theta$ and $\alpha$. Hence, in a coherent state, all quadratures are affected in the same way by quantum noise. Recalling the Heisenberg inequality (2.7), one sees that $|\alpha\rangle$ is at the lower limit of the noise product imposed by the uncertainty relation. The eigenstate relation (2.13) also implies that quadratures at

ninety degrees from one another are uncorrelated

$$\mathrm{Cov}\left(\hat{Q}(\theta), \hat{Q}\left(\theta + \frac{\pi}{2}\right)\right) = 0. \tag{2.15}$$

Coherent states are of fundamental importance in quantum optics because they approximate the output field state of a single-mode laser[40]. Consider expression (2.11) for a mode of the electromagnetic field in a coherent state

$$\left\langle \Delta^2 \hat{E}(\mathbf{r}, t) \right\rangle = \frac{\hbar\omega}{2\epsilon_0 V}. \tag{2.16}$$

Hence, the fluctuations of the electric field in a coherent state are stationary in both space and time. The dependence of the variance on the quantization volume has been investigated experimentally and leads to the Casimir effect[41]. The above expression is independent of $\alpha$. This indicates that the magnitude of the field fluctuations in laser light is the same as that of vacuum so that this source of radiation is extremely quiet.

Squeezed states of the harmonic oscillator can be defined in a way analogous to coherent states. Let $\hat{b}$ and $\hat{b}^\dagger$ denote creation and annihilation operators related to $\hat{a}$ by

$$\hat{a} = \mu\hat{b} + \nu\hat{b}^\dagger, \tag{2.17}$$

where the complex numbers $\mu$ and $\nu$ satisfy the constraint

$$|\mu|^2 - |\nu|^2 = 1. \tag{2.18}$$

This constraint is necessary if $\hat{b}$ and $\hat{b}^\dagger$ are to satisfy the same commutation relations as $\hat{a}$ and $\hat{a}^\dagger$. Squeezed states of the $\hat{a}$-oscillator are defined as eigenstates of the operator $\hat{b}$ [2]

$$\hat{b}\,|\mu, \nu, \alpha\rangle = \alpha\,|\mu, \nu, \alpha\rangle\,. \tag{2.19}$$

Taking into account the two real numbers specifying $\alpha$ and the extra two real numbers needed to label all transformations compatible with (2.18), one can see that squeezed

states form a family parameterized by four real numbers. For later convenience, an explicit parameterization of $\mu$ and $\nu$ is given by the following expressions

$$\mu = \cosh\eta, \tag{2.20}$$

$$\nu = e^{2i\gamma}\sinh\eta. \tag{2.21}$$

A squeezed vacuum is defined as a squeezed state with $\alpha = 0$.

The mean deviation of quadratures of $\hat{a}$ in a squeezed state can be computed using (2.5), (2.17) and (2.19). One finds the following expression

$$\left\langle \Delta^2 \hat{Q}(\theta) \right\rangle = \frac{1 + 2\left|\nu\right|^2 + 2\mathrm{Re}\left(e^{-2i\theta}\mu\nu\right)}{2}. \tag{2.22}$$

As for coherent states, the noise level of the quadratures in a squeezed state is independent of $\alpha$. Consider the explicit parameterization of $\mu$ and $\nu$ given by (2.20) and (2.21). The minimum noise level in (2.22) occurs when

$$2(\theta_{\min} - \gamma) = \pi, \tag{2.23}$$

in which case we have

$$\left\langle \Delta^2 \hat{Q}(\theta_{\min}) \right\rangle = \frac{1 - 2e^{-|\eta|}\sinh\left|\eta\right|}{2}. \tag{2.24}$$

This noise level is lower than the vacuum level $1/2$ for any non-vanishing value of $\eta$, and decreases monotonically to zero when $|\eta| \to \infty$. For this reason, $\eta$ is known as the *squeeze parameter*. The phase $\gamma$ on the other hand does not affect the minimum level of fluctuations. It determines however the phase of the quadrature for which the minimum fluctuations are observed. Figure 2-1 shows the variance of $\hat{Q}$ as a function of $\theta$ for a number of values of the squeeze parameter and for $\gamma = 0$. As can be seen from this figure, the reduced noise of one quadrature is compensated by an increase in the fluctuations of the quadrature at ninety degrees. In fact, one verifies from (2.22)

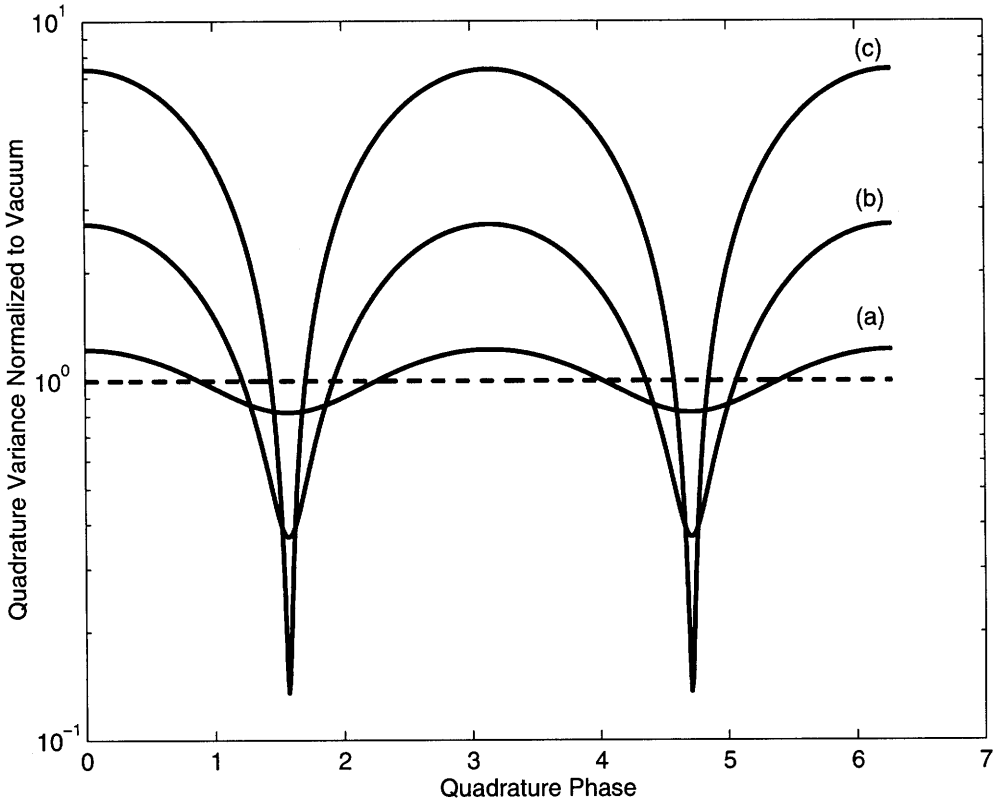


Figure 2-1: Normalized quadrature variance, $\left\langle \Delta^2 \hat{Q}(\theta) \right\rangle / \langle 0| \Delta^2 \hat{Q} |0\rangle$, as a function of $\theta$. (a) $\eta = 0.2$, (b) $\eta = 1$, (c) $\eta = 2$.

that

$$\left\langle \Delta^2 \hat{Q}(\theta) \right\rangle \left\langle \Delta^2 \hat{Q}\left(\theta + \frac{\pi}{2}\right) \right\rangle = \frac{1 + \sinh^2 2\eta \sin^2\left(2(\gamma - \theta)\right)}{4}, \tag{2.25}$$

which is always larger than $1/4$, unless $\theta = \gamma + n\pi/4$, with $n$ integer. The uncertainty relation (2.7) is therefore satisfied. One can also see from Fig. 2-1 that, as the squeeze parameter increases, the range of phases over which quantum noise reduction occurs shrinks. Using (2.12) and (2.19), one can show that

$$\mathrm{Cov}\left(\hat{Q}(\theta), \hat{Q}\left(\theta + \frac{\pi}{2}\right)\right) = \frac{\sinh 2\eta \sin\left(2(\gamma - \theta)\right)}{2}. \tag{2.26}$$

This result indicates that, unless $\theta = \gamma + n\pi/4$, with $n$ integer, the quadratures at ninety degrees are correlated.

Consider a mode of the electromagnetic field in a squeezed state. The next chapter will indicate how such states can be created using optical fibers. Assuming that $\gamma = -\pi/2$ (i.e. $\theta_{\min} = 0$) and that $\eta > 0$ for definiteness, we find, using the general

expression (2.11) in conjunction with (2.24), (2.25) and (2.26),

$$\left\langle \Delta^2 \hat{E}(\mathbf{r},t) \right\rangle = \frac{\hbar\omega}{2\epsilon_0 V}\left\{1 + 2\sinh\eta\left(e^{\eta}\sin^2(\omega t - \mathbf{k}\cdot\mathbf{r}) - e^{-\eta}\cos^2(\omega t - \mathbf{k}\cdot\mathbf{r})\right)\right\}. \tag{2.27}$$

Normalizing this expression to the constant vacuum level, we find that it reaches a minimum given by

$$\frac{\min\left\langle \Delta^2 \hat{E} \right\rangle}{\langle 0|\, \Delta^2 \hat{E}\, |0\rangle} = \frac{1 - 2e^{-|\eta|}\sinh|\eta|}{2}. \tag{2.28}$$

Hence, the fluctuations of the electric field can be reduced momentarily below those of the vacuum. As time evolves however, the level of fluctuations of the electric field at a given point cycles through quiet and noisy phases at twice the optical frequency. This time dependence, which is too fast to be resolved by standard detectors, must be canceled by mixing the squeezed field with an optical field having the same carrier frequency. This is accomplished through balanced homodyne detection.

### 2.1.4 The Balanced Homodyne Detector

Consider the arrangement depicted on Figure 2-2 [42, 43]. A weak monochromatic signal, $\hat{E}_S$ with annihilation operator $\hat{a}_S$ is mixed with an optical field $\hat{E}_L$ with annihilation operator $\hat{a}_L$ using a 50/50 beamsplitter. The two fields are assumed to have the same frequency and the same linear polarization. The beamsplitter outputs are detected with photodetectors producing photocurrents that are electronically subtracted. The resulting difference photocurrent is then proportional to a quadrature of the signal field, with the phase of the quadrature corresponding to the relative phase between the signal and the local oscillator. To derive this result explicitly, we express $\hat{Q}(0)$ and $\hat{Q}(\pi/2)$ in (2.9) in terms of creation and annihilation operators using (2.5). We find, for the signal at the surface of the beamsplitter

$$\hat{E}_S(t) = \left(\frac{\hbar\omega}{2\epsilon_0 V}\right)^{1/2}\left(\hat{a}_S e^{i\omega t} + \hat{a}_S^{\dagger} e^{-i\omega t}\right). \tag{2.29}$$

A similar expression is obtained for the local oscillator field, but with $\hat{a}_S$ replaced

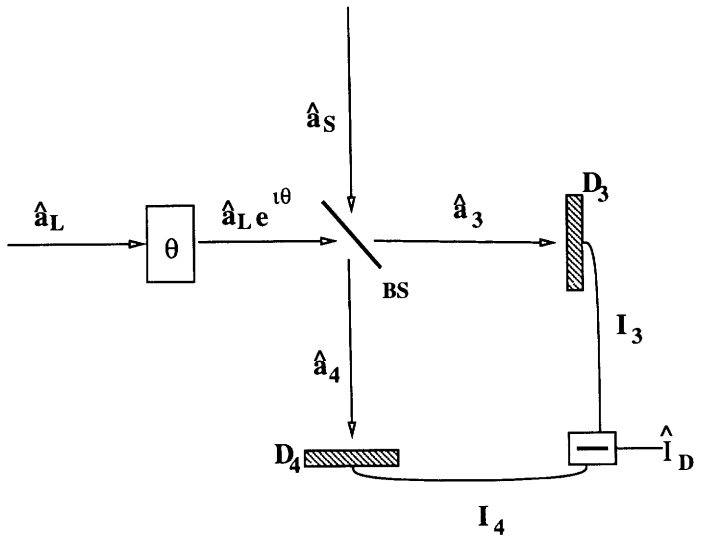


Figure 2-2: Balanced homodyne detector. BS is a 50/50 beamsplitter, $D_3$ and $D_4$ are slow photodetectors, $\hat{I}_D = \hat{I}_3 - \hat{I}_4$.

by $e^{i\theta}\hat{a}_L$. The additional phase is introduced to take into account the relative phase between the signal and the local oscillator. In practice, $\theta$ can be adjusted by controlling the optical path length of the local oscillator. A phase shifter was introduced for that purpose in Fig. 2-2. In general, the signal and the local oscillator can also have different transverse profiles. For the situations considered in this thesis however, both optical fields are extracted from the same optical fiber and therefore have identical profiles.

The beamsplitter is a lossless device mixing linearly the fields of the signal and of the local oscillator. The explicit transformation relating the input and output annihilation operators on Figure 2-3 is given by[42, 44, 45]

$$\hat{a}_3 = r\hat{a}_1 + t\hat{a}_2 \tag{2.30}$$

$$\hat{a}_4 = t\hat{a}_1 - r\hat{a}_2 \tag{2.31}$$

where $r$ and $t$ are the reflection and transmission amplitude coefficients satisfying $|r|^2 + |t|^2 = 1$, in accordance with power conservation. In the example considered on

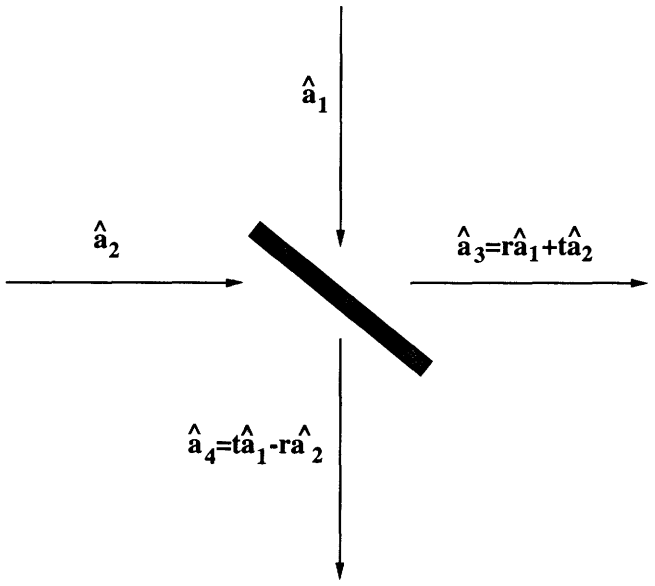


Figure 2-3: Transformation of amplitudes by a lossless beamsplitter

Fig. 2-2, we have $\hat{a}_1 = \hat{a}_S$, $\hat{a}_2 = e^{i\theta}\hat{a}_L$ and $r = t = 1/\sqrt{2}$, so that

$$\hat{a}_3 = \frac{1}{\sqrt{2}}\left(\hat{a}_S + e^{i\theta}\hat{a}_L\right), \tag{2.32}$$

$$\hat{a}_4 = \frac{1}{\sqrt{2}}\left(\hat{a}_S - e^{i\theta}\hat{a}_L\right). \tag{2.33}$$

Assuming perfect quantum efficiencies for detectors $D_3$ and $D_4$, each photon in beams 3 and 4 generates an electron in the corresponding detector. The photocurrents are then

$$\hat{I}_i = I_0 \hat{a}_i^\dagger \hat{a}_i \tag{2.34}$$

for $i = 3, 4$. Note that no fast temporal dependence appears in the expression of the photocurrents because the local oscillator and the signal have the same frequency. The constant $I_0$ is the current generated by a single electron in the circuit. The difference between the photocurrents can now be seen to be proportional to $\hat{a}_3^\dagger\hat{a}_3 - \hat{a}_4^\dagger\hat{a}_4$. Inserting the beamsplitter transformation (2.32) and (2.33) in this expression, we find the

difference photocurrent

$$\hat{I}_D = I_0 \left( e^{-i\theta} \hat{a}_L^\dagger \hat{a}_S + e^{i\theta} \hat{a}_L \hat{a}_S^\dagger \right). \tag{2.35}$$

In balanced homodyne detection, the signal is very weak and the local oscillator is an intense laser beam described by the coherent state $|A_{LO}\rangle$. One can express the annihilation operator of this field as $\hat{a}_L = A_{LO} + \Delta\hat{a}_L$. The second term is the annihilation operator of an oscillator in vacuum

$$\Delta\hat{a}_L |A_{LO}\rangle = (\hat{a}_L - A_{LO}) |A_{LO}\rangle = 0. \tag{2.36}$$

The operator $\Delta\hat{a}_L$, which measures the small quantum noise affecting the laser field, is needed for $\hat{a}_L$ to satisfy the commutation relation (2.4). Since it is small, it contributes to second order in the difference photocurrent and can therefore be neglected. We can assume without loss of generality that $A_{LO}$ is real since we have already introduced the relative phase $\theta$. We then have

$$\hat{I}_D(\theta) = \sqrt{2} I_0 |A_{LO}| \hat{Q}_S(\theta), \tag{2.37}$$

i.e. the difference photocurrent is proportional to a quadrature of the signal with a phase controlled by $\theta$. As can be seen, the local oscillator acts like an amplifier since its strength appears in the proportionality factor between these quantities [42]. Unlike the electric field in the previous paragraph, the photocurrent is a "DC" quantity. We therefore have a direct means to monitor the variance of the quadratures.

Assume that the signal port is left unexcited. The photocurrent produced by balanced homodyne detection will vanish in average, but a series of measurements will produce small values scattered around zero with a dispersion

$$\left\langle \Delta^2 \hat{I}_{\text{shot}} \right\rangle = I_0^2 |A_{LO}|^2, \tag{2.38}$$

where (2.14) was used. This expression is known as the shot noise level and is inde-

pendent of the phase $\theta$. When the input signal is a squeezed vacuum and when the phase $\theta$ is stabilized so that the quiet quadrature is measured, one observes reduced fluctuations of the photocurrent. Using (2.24) we have

$$\left\langle \Delta^2 \hat{I}_{\min} \right\rangle = \left\langle \Delta^2 \hat{I}_{\text{shot}} \right\rangle \left(1 - 2e^{-|\eta|} \sinh |\eta|\right). \tag{2.39}$$

The reduction of balanced homodyne photocurrent fluctuations below the shot noise level can be considered as the experimental definition of a squeezed state.

## 2.2 Pulsed Squeezed Light

Squeezed light generation results from nonlinear optical processes which are intrinsically weak. In order to achieve measurable degrees of squeezing, optical fields with large intensities must be used. In practice, the powers needed can only be reached with pulsed lasers. In this paragraph, we generalized the previous definitions of quadratures and of squeezed light to take into account the multimode nature of pulsed excitations. In particular, we will consider the noise level of a balanced homodyne detector when the signal and the local oscillator are both pulsed [46, 47]. Our main interest is in the mode-matched signals and local oscillators produced by fiber squeezers. We will assume that a narrow band of frequencies is excited around a carrier frequency $\omega_0$. Since the bandwidth is measured relative to $\omega_0$, pulses as short as a few tens of femtoseconds can still be considered as narrow band because of the very short optical cycle ($\sim 1fs$). The waveguide is assumed single-mode and lossless in the band of excited frequencies. This set of assumptions constitutes a very good model for communication-grade optical fibers in the wavelength region between $700nm$ and $1.8nm$.

In Appendix B, we introduced the quantum envelope operator defined by

$$\hat{A}(z,t) = e^{i\omega_0 t - i\beta_0 z} \int_{-\infty}^{\infty} d\beta \sqrt{\frac{v_g(\beta)}{2\pi}} \hat{a}(\beta,t) e^{i\beta z}. \tag{2.40}$$

This scalar field is the quantum analog of the slowly-varying envelope familiar from

nonlinear optics[53, 54, 55]. We showed how to recover the electric field operator from the envelope and its spatial derivatives (see (B.12)). We also introduced the retarded time as

$$\tau = t - z/v_g, \tag{2.41}$$

where $v_g$ is the group velocity. We indicated that if the dynamics of the field inside the fiber does not couple forward and backward propagating modes, the following *equal-space* commutation relations were verified

$$\begin{aligned} \left[\hat{A}(z,\tau), \hat{A}(z,\tau')\right] &= 0 \\ \left[\hat{A}(z,\tau), \hat{A}^\dagger(z,\tau')\right] &= \delta(\tau - \tau'). \end{aligned} \tag{2.42}$$

We finally showed how the photocurrent produced by a slow photodetector excited by an optical pulse could be simply related to the envelope by

$$\hat{I} = I_0 \int_{-\infty}^{\infty} d\tau \hat{A}^\dagger(\tau)\hat{A}(\tau). \tag{2.43}$$

### 2.2.1 Pulsed Quadratures and Pulsed Squeezed States

We consider the envelope at some point $z$, and we denote by $\hat{A}(\tau)$ the corresponding field. In the case of a single harmonic oscillator, only two independent quadrature operators can be defined, corresponding to the number of independent degrees of freedom of this system. The quantum field $\hat{A}(\tau)$ has an infinite number of degrees of freedom and, consequently, one can define an infinite number of independent quadratures. We first define the annihilation operator for the field mode $f$

$$\hat{a}_f = \frac{1}{\sqrt{2}} \int_{-\infty}^{\infty} d\tau\, f^*(\tau)\hat{A}(\tau), \tag{2.44}$$

where $f$ is a normalized square integrable function

$$1 = \int_{-\infty}^{\infty} d\tau\, |f(\tau)|^2 . \tag{2.45}$$

Using (2.42), we have

$$\left[\hat{a}_f, \hat{a}_f^\dagger\right] = 1. \tag{2.46}$$

The quadratures of this mode are defined by

$$\begin{aligned}\hat{Q}_f(\theta) &= \frac{e^{-i\theta}\hat{a}_f + e^{i\theta}\hat{a}_f^\dagger}{\sqrt{2}} \\ &= \frac{1}{\sqrt{2}}\int_{-\infty}^{\infty} d\tau \left\{e^{-i\theta} f^*(\tau)\hat{A}(\tau) + e^{i\theta} f(\tau)\hat{A}^\dagger(\tau)\right\},\end{aligned} \tag{2.47}$$

and obey the commutator

$$\left[\hat{Q}_f(\theta), \hat{Q}_f\left(\theta + \frac{\pi}{2}\right)\right] = i. \tag{2.48}$$

The minimum quadrature variance associated with $f$ leads to

$$\min_\theta \left\langle \Delta^2 \hat{Q}_f(\theta)\right\rangle = \frac{1}{2} + \left\langle \hat{a}_f^\dagger \hat{a}_f\right\rangle - \left\langle \hat{a}_f^\dagger\right\rangle \left\langle \hat{a}_f\right\rangle - \left|\left\langle \hat{a}_f^{\dagger 2}\right\rangle - \left\langle \hat{a}_f^\dagger\right\rangle^2\right|. \tag{2.49}$$

Pulsed coherent states are defined as eigenstates of $\hat{A}(\tau)$

$$\hat{A}(\tau)\,|\alpha\rangle = \alpha(\tau)\,|\alpha\rangle\,. \tag{2.50}$$

In free space, the field operator depends only on $\tau$ and the above coherent states are equivalent to usual spatial coherent states in the distant past $t_0 \to -\infty$

$$\hat{A}(z, t_0)|\alpha> = \hat{A}(\tau = t_0 - z/v_g)|\alpha> = \alpha(t_0 - z/v_g)|\alpha>\,. \tag{2.51}$$

One can therefore prepare a pulsed coherent state at the input of a fiber by forming a spatial coherent state in the distant past and letting it propagate toward the fiber end. Coherent states describe approximately the output of modelocked lasers. We note however that no quantum theory of modelocked lasers has yet been developed. Although the exact nature of the quantum state of the field at the output of a multimode laser is not known, coherent states are used as an approximation throughout the literature and have led to results consistent with experiments. This

assumption generalizes the well-known result for single-mode lasers. We shall make this approximation in this thesis, except in Chapter 5 where quantized solitons are described.

The fluctuations of all pulsed quadratures in a coherent state are easily shown to have a variance

$$\left\langle \Delta^2 \hat{Q}_f(\theta) \right\rangle = \frac{1}{2}. \tag{2.52}$$

This result is identical to the single-mode variance and follows from the normalization condition imposed on $f$. Note in particular that the above expression is independent of $\alpha(\tau)$ and therefore applies for a field in vacuum. It is also independent of the function $f$, so that all quadratures have the same fluctuation level in any coherent states.

Pulsed squeezed states for the field $\hat{A}(\tau)$ are defined in a way analogous to the single-mode case. We first introduce a canonical transformation

$$\hat{A}(\tau) = \int d\tau' \left\{ \mu(\tau;\tau')\hat{A}_i(\tau') + \nu(\tau;\tau')\hat{A}_i^\dagger(\tau') \right\}, \tag{2.53}$$

where the fields $\hat{A}_i(\tau)$ and $\hat{A}_i^\dagger(\tau)$ obey

$$[\hat{A}_i(\tau), \hat{A}_i^\dagger(\tau')] = \delta(\tau - \tau'), \tag{2.54}$$

and the complex functions $\mu$ and $\nu$ satisfy the constraint

$$\delta(\tau - \tau') = \int d\tau'' \left\{ \mu(\tau;\tau'')\mu^*(\tau',\tau'') - \nu(\tau;\tau'')\nu^*(\tau',\tau'') \right\}. \tag{2.55}$$

Pulsed squeezed states are eigenstates of the field $\hat{A}_i(\tau)$

$$\hat{A}_i(\tau) \left| \mu, \nu, \alpha \right\rangle = \alpha(\tau) \left| \mu, \nu, \alpha \right\rangle \tag{2.56}$$

In particular, a pulsed squeezed vacuum of the $\hat{A}$-field satisfies the above relation with $\alpha = 0$. An infinite number of such states can obviously be defined since the constraint (2.55) is highly degenerate.

As for the single-mode case, pulsed squeezed states are characterized by reduced levels of quantum fluctuations for certain quadratures. In fact, a more general definition of squeezed states would include any state displaying a reduced level of quadrature fluctuations for at least one function $f$ and at least one phase $\theta$. In the context of fiber squeezing, the field $\hat{a}(\tau)$ will be identified as the envelope at the input of the fiber, i.e $\hat{A}_i(\tau) = \hat{A}(0,\tau)$. The functions $\mu$ and $\nu$ will be Green's functions describing the evolution of the envelope through the fiber, and the field $\hat{A}(\tau)$ will be the envelope at the output of the fiber, i.e. $\hat{A}(\tau) = \hat{A}(z,\tau)$. Hence, a coherent state for the input field will be a squeezed state for the output field.

Because of the infinite number of degrees of freedom in the present problem, the formal analysis of general squeezed states is tedious and will not be carried out here. Consider however the special case where the functions $\mu$ and $\nu$ are proportional to delta functions

$$\mu(\tau;\tau') = \delta(\tau - \tau')\mu(\tau), \quad \nu(\tau;\tau') = \delta(\tau - \tau')\nu(\tau), \tag{2.57}$$

with

$$1 = |\mu(\tau)|^2 - |\nu(\tau)|^2 . \tag{2.58}$$

This type of canonical transformation occurs in dispersionless fiber squeezing and implies that the noise properties of the field at each point across the pulse are completely decoupled. Consider for example the variance of $\hat{Q}_f(\theta)$

$$\left\langle \Delta^2 \hat{Q}_f(\theta) \right\rangle = \int d\tau \, |f(\tau)|^2 \left\{ \frac{1 + 2\,|\nu(\tau)|^2 + 2\mathrm{Re}\left[ e^{-2i\left(\theta + \theta_f(\tau)\right)} \mu(\tau)\nu(\tau) \right]}{2} \right\}, \tag{2.59}$$

where $\theta_f(\tau)$ is the time dependent phase of $f(\tau)$. Comparing this expression with (2.22), we see that the pulsed variance is the weighted sum of single-mode variances associated with each value of $\tau$. The function $\theta_f(\tau)$ changes the phase of the quadrature associated with each point of the pulse. The fluctuations of $\hat{Q}_f(\theta)$ are minimized when $\theta$ and the phase of $f$, are chosen so that the fluctuations of each oscillator are

minimized. In general, the phases of $\mu$ and $\nu$ will be time dependent, and $\theta_f(\tau)$ must vary to cancel this dependence. When this is realized, we find

$$\left\langle \Delta^2 \hat{Q}_{f_0}(\theta_0) \right\rangle = \int d\tau \, |f_0(\tau)|^2 \left\{ \frac{1 - 2e^{-|\eta(\tau)|} \sinh |\eta(\tau)|}{2} \right\}, \tag{2.60}$$

where the time dependent squeeze parameter is defined such that $|\mu(\tau)|^2 = \cosh^2 \eta(\tau)$, and $f_0$ is any normalized square integrable function with the optimum phase profile.

### 2.2.2 Pulsed Homodyne Detection

Consider again Figure 2.2, and assume that both the signal and the local oscillator are pulsed. By linearity, the transformations (2.32) and (2.33) apply for each frequency component of the fields. Since by assumption the signal and the local oscillator have the same carrier frequency and the same transverse profile, we find that the beamsplitter transformation can be applied directly to the envelope fields. Hence, the fields incident on detectors $D_3$ and $D_4$ have the envelopes

$$\begin{aligned} \hat{A}_3(\tau) &= \frac{1}{\sqrt{2}} \left( \hat{A}_S(\tau) + e^{i\theta} \hat{A}_L(\tau) \right), \\ \hat{A}_4(\tau) &= \frac{1}{\sqrt{2}} \left( \hat{A}_S(\tau) - e^{i\theta} \hat{A}_L(\tau) \right). \end{aligned} \tag{2.61}$$

Using formula (B.17) for the photocurrent generated by a pulse, we find, for the balanced homodyne photocurrent

$$\hat{I}_D = I_0 \int d\tau \left\{ e^{-i\theta} \hat{A}_L^\dagger(\tau) \hat{A}_S(\tau) + e^{i\theta} \hat{A}_S^\dagger(\tau) \hat{A}_L(\tau) \right\}. \tag{2.62}$$

Once again, balanced homodyne detection is usually performed on a weak signal and with a strong local oscillator. Neglecting the quantum fluctuations of the latter, we find [46, 47]

$$\begin{aligned} \hat{I}_D &= I_0 \int d\tau \left\{ e^{-i\theta} A_{LO}^*(\tau) \hat{A}_S(\tau) + e^{i\theta} A_{LO}(\tau) \hat{A}_S^\dagger(\tau) \right\} \\ &= I_0 \sqrt{2n_0} \hat{Q}_f(\theta), \end{aligned} \tag{2.63}$$

where the modal function is

$$f(\tau) = \frac{A_{LO}(\tau)}{\sqrt{n_0}}, \tag{2.64}$$

and the photon number is

$$n_0 = \int d\tau \, |A_{LO}|^2 \, . \tag{2.65}$$

Once again, the homodyne photocurrent is proportional to a quadrature of the field.

We showed in the last paragraph that the quadrature fluctuations were minimized in the dispersionless case when the phase profile of $f$ is chosen to cancel that of $\mu\nu$. In practice it is very difficult to generate a local oscillator with this optimum phase profile. For this reason, squeezing experiments are rarely able to detect the maximum degree of squeezing of the field.

# Chapter 3

# The Dispersive Sagnac Fiber Squeezer

In Chapter 2, we introduced the concept of squeezed vacuum for optical pulses. As was pointed out in Chapter 1, these states are a fundamental ingredient of Caves's scheme to make interferometric measurements beyond the standard quantum limit. In the present chapter, we explain how one can generate a squeezed vacuum using a nonlinear Sagnac interferometer. This device is presented in Section 3.1. Section 3.2 introduces the linearized equations for the evolution of quantum noise in single-mode optical fibers. The solution of these equations at zero dispersion is also given. In Section 3.3, a numerical implementation of the linearized equations for general dispersion conditions is presented. We show in this final section that the saturation in squeezing observed in current set-ups can be eliminated by operating the squeezer either with optical solitons, or in the positive dispersion regime. The material of Sections 3.1 can be considered as a review and follows closely the presentation of [51]. The linearized equations presented in Section 3.2 are somewhat novel as they incorporate the finite response time of the nonlinearity and Raman noise to be further discussed in Chapter 4. Linearized noise equations have however been used long ago by Carter [58], Shirasaki and Haus [31] and Haus and Lai [60]. Section 3.3 introduces new results which were published only partially in [91, 92].

## 3.1 The Nonlinear Sagnac Squeezer

The propagation of an initially coherent pulse in a single-mode optical fiber results in a pulsed squeezed state. As large optical intensities are required to achieve significant squeezing levels, these squeezed states usually have large mean fields (i.e $|\alpha(\tau)|^2 \ll 1$ in (2.56)). In order to produce a squeezed vacuum, an interferometric scheme based on the Sagnac loop must be used [31]. In this section, we review the operation of this squeezer following the discussion of [51]. We obtain an expression for the balanced homodyne photocurrent variance in terms of correlation functions of the field at the output of the fiber. As we do not explicitly use the input-output relation for the envelope, the formula we obtain is independent of the dispersion conditions in the fiber, does not assume that the input state is coherent and does not rely on the linearized approximation. We will use this expression in latter sections and in Chapter 4. Other treatments of the Sagnac squeezer can also be found. In [31] for example, the zero-dispersion case is considered in the linearized limit for input coherent states. In [48, 49], the same case is analyzed, but without the linearized approximation. A discretized-time quantization was implicit in these papers (see Section 4.2 for a discussion of the limitations of this approach). In [50], a method to treat non-coherent input states was developed.

### 3.1.1 Principle of Operation

The Sagnac squeezer uses the coherence properties of two identical pulses in an interferometer to separate a squeezed vacuum in one of its output ports. Fig 3-1 shows a fiber loop interferometer made of polarization maintaining fiber and of a 50/50 fiber coupler. This passive device is excited with a linearly polarized pulse coupled through port A. The input field splits into two identical pulses at the 3dB coupler. Each of these pulses travels the loop in opposite directions. When the pulses recombine at the fiber coupler, their classical parts add coherently in port A and destructively in port B. As a result, essentially all the optical power exits through the input port A. No interference occurs for the uncorrelated quantum fluctuations of the two pulses.

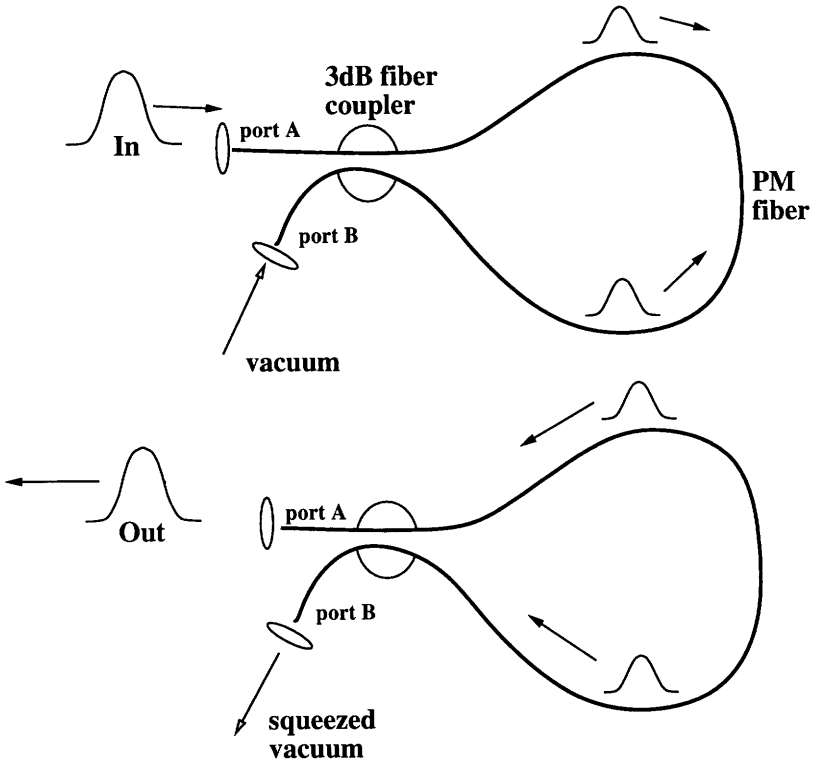


Figure 3-1: Sagnac fiber squeezer

For this reason, squeezed fluctuations exit both ports of the device. The net result is a squeezed vacuum in port B and a squeezed pulse with a large mean field in port A. The above picture derives from the linearized approximation and is not valid when very large nonlinear phase shifts are achieved in the loop. In this limit, quantum noise significantly smears the phase of the pulses which do not interfere properly at the fiber coupler. When this regime is reached, significant optical power exits through port B and the nonlinear Sagnac interferometer no longer produces a squeezed vacuum. The analysis below is not limited to the linearized approximation.

### 3.1.2 Sagnac Noise Reduction Ratio

Figure 3-2 shows a balanced Mach-Zehnder interferometer followed by a balanced homodyne receiver. Identical fibers were introduced in both arms of the interferometer. This device is equivalent to the Sagnac loop except for the brief nonlinear interaction taking place when the pulses meet halfway around the Sagnac loop. This effect is irrelevant because it affects both pulses in the same manner (i.e. it is reciprocal) and does not imbalance the interferometer. In practice, Mach-Zehnder interferometers

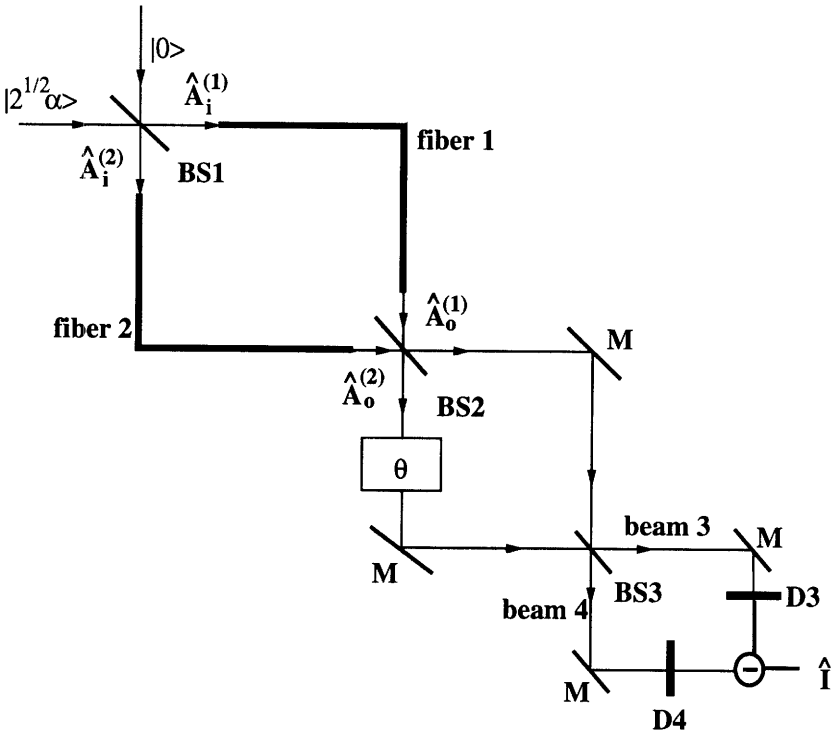


Figure 3-2: Balanced nonlinear Mach-Zehnder interferometer followed by homodyne receiver. BS denotes a 50-50 beamsplitter, $D_3$ and $D_4$ are slow but perfect photodetectors, and $M$ are perfect mirrors.

are difficult to balance and for this reason, no squeezer uses that geometry. It has however a pedagogical value because all the modes of interest are spatially distinct and can be labelled easily. One port of BS1 is excited by a short pulse. We are interested in the resulting fluctuation level of the photocurrent $\hat{I}$ obtain as the difference between the photocurrents produced by detectors 3 and 4. We assume that the two detectors are slow compared with the duration of the pulse and that their quantum efficiency is 1. We will denote by $\hat{A}_o^{(1)}(\tau)$ and $\hat{A}_o^{(2)}(\tau)$ the envelopes at the output of fiber 1 and 2 respectively. Using the beamsplitter transformation (2.61) at BS2 and BS3, the flux of beams 3 and 4 can be related to the fluxes $\hat{A}_o^{(1)\dagger}\hat{A}_o^{(1)}$ and $\hat{A}_o^{(2)\dagger}\hat{A}_o^{(2)}$. The difference photocurrent of the Sagnac squeezer is therefore

$$\hat{I} = I_0 \int d\tau \cos\theta \left(\hat{A}_o^{(1)\dagger}\hat{A}_o^{(1)} - \hat{A}_o^{(2)\dagger}\hat{A}_o^{(2)}\right) + i \sin\theta \left(\hat{A}_o^{(1)\dagger}\hat{A}_o^{(2)} - \hat{A}_o^{(2)\dagger}\hat{A}_o^{(1)}\right), \qquad (3.1)$$

where $I_0$ is a constant and $\theta$ is the adjustable relative phase between the two input beams to BS3. Since both fibers are excited symmetrically, the moments of $\hat{A}_o^{(1)}$

and $\hat{A}_o^{(2)}$ are identical and the expectation value of $\hat{I}$ vanishes. Measurements of this photocurrent for a large number of pulses prepared in the same quantum state give data scattered with a variance [51, 52]

$$\left\langle \hat{I}^2 \right\rangle = I_0^2 \left\{ 2F_0 + 2F_1 \sin^2\theta + F_2 \sin 2\theta \right\}. \tag{3.2}$$

where $F_0$ is the width of the photostatistics in each arm of the interferometer

$$F_0 = \left\langle \hat{n}_0^2 \right\rangle - \langle \hat{n}_0 \rangle^2 \tag{3.3}$$

with

$$\hat{n}_0 = \int d\tau \hat{A}_o^\dagger(\tau)\hat{A}_o(\tau), \tag{3.4}$$

and the expectation values $F_1$ and $F_2$ are given by

$$F_1 = \int d\tau_1 d\tau_2 \left\{ \left| \left\langle \hat{A}_o^\dagger(\tau_1)\hat{A}_o(\tau_2) \right\rangle \right|^2 - \left| \left\langle \hat{A}_o(\tau_1)\hat{A}_o(\tau_2) \right\rangle \right|^2 \right\}, \tag{3.5}$$

$$F_2 = 4Im \int d\tau_1 d\tau_2 \left\langle \hat{A}_o^\dagger(\tau_2)\hat{A}_o(\tau_2)\hat{A}_o(\tau_1) \right\rangle \left\langle \hat{A}_o^\dagger(\tau_1) \right\rangle. \tag{3.6}$$

In these expressions we dropped the superscripts "(1)" and "(2)" since both fields have the same moments and either one can be used in $F_0$, $F_1$ and $F_2$. We will show in the next section that the photostatistics is preserved by the evolution of the field in the Kerr medium. As a result, $F_0$ can be evaluated directly from the input field. So far we did not assume a specific input state for the envelope. If we restrict ourselves to the case of Poisson input photostatistics, we have $F_0 = n_0$, where $n_0 \equiv \langle \hat{n}_0 \rangle$. For $\theta = 0$ or $\pi$, no mixing of beams 1 and 2 occurs and $\left\langle \hat{I}^2 \right\rangle = 2I_0^2 n_0$. This is the shot noise level. To display photocurrent fluctuations below that level, we minimize (3.2) with respect to $\theta$ and we normalize to $2I_0^2 n_0$

$$R_{Sagnac} = \frac{\min_\theta < \hat{I}^2(\theta) >}{2I_0^2 n_0} = 1 + \frac{1}{2n_0}F_1 - \frac{1}{2n_0}\sqrt{F_1^2 + F_2^2}. \tag{3.7}$$

Sub-shot noise fluctuations occur whenever $F_2$ is different from zero. Expression (3.7) is the main result of this section. It is valid beyond the small noise approximation and for any dispersion regime. We shall come back to this expression in Chapter 4. In the following, we assume that quantum noise is much smaller than the mean field. In this case the above formula can be simplified. Let us write the output envelopes as

$$\hat{A}_o^{(1,2)}(\tau) = \left\langle \hat{A}_o(\tau) \right\rangle + \hat{a}_o^{(1,2)}(\tau). \tag{3.8}$$

The photocurrent is then

$$\begin{aligned} \hat{I} &= I_0 \int d\tau e^{-i\theta} \left\langle \hat{A}_o(\tau) \right\rangle^* \hat{a}_o^{(1)}(\tau) + e^{i\theta} \left\langle \hat{A}_o(\tau) \right\rangle \hat{a}_o^{(1)\dagger}(\tau) \\ &- I_0 \int d\tau e^{-i\theta} \left\langle \hat{A}_o(\tau) \right\rangle^* \hat{a}_o^{(2)}(\tau) + e^{i\theta} \left\langle \hat{A}_o(\tau) \right\rangle \hat{a}_o^{(2)\dagger}(\tau) \\ &+ I_0 \int d\tau \cos\theta \left( \hat{a}_o^{(1)\dagger} \hat{a}_o^{(1)} - \hat{a}_o^{(2)\dagger} \hat{a}_o^{(2)} \right) + i \sin\theta \left( \hat{a}_o^{(1)\dagger} \hat{a}_o^{(2)} - \hat{a}_o^{(2)\dagger} \hat{a}_o^{(1)} \right). \end{aligned} \tag{3.9}$$

The linearized approximation neglects the terms on the third line of this expression. When this approximation is made, $\hat{I}$ is the sum of two quadratures of the independent noise operators $\hat{a}_o^{(1)}$ and $\hat{a}_o^{(2)}$, which have identical moments. Defining the pulsed quadratures of the noise

$$\hat{Q}_\theta(z) \equiv \frac{1}{\sqrt{2n_0}} \int d\tau \left\{ e^{-i\theta} \left\langle A^*(z,\tau) \right\rangle \hat{a}(z,\tau) + e^{i\theta} \left\langle A(z,\tau) \right\rangle \hat{a}^\dagger(z,\tau) \right\}, \tag{3.10}$$

and the SPM noise reduction ratio

$$R_{SPM}(z) \equiv \frac{\min_\theta \left\langle \Delta^2 \hat{Q}_\theta(z) \right\rangle}{\langle 0 | \Delta^2 \hat{Q}_\theta | 0 \rangle}, \tag{3.11}$$

we find that in the linearized limit

$$R_{Sagnac}(z) \simeq R_{SPM}(z), \tag{3.12}$$

where fibers of length $z$ were assumed. For longer fibers, the terms on the third line of (3.9) become important and the Sagnac photocurrent (3.1) no longer measures

quadratures of the noise. It is known for example that $R_{SPM}$ rises rapidly above shot noise beyond the linearized regime[73, 77]. It is however obvious that $R_{Sagnac}$ is at most equal to 1, corresponding to the choice $\theta = 0$ in (3.1) [51].

## 3.2 Linearized Theory of Self-Phase Modulation

In this section we provide equations from which the input-output relations for the envelope of each fiber can be derived. Throughout the remainder of this chapter we assume that quantum noise is much smaller than the mean field. This approximation leads to the linearized theory. The validity of this approach will be investigated in Chapter 4 and Chapter 5 for the zero-dispersion and soliton regime respectively. We will show that it provides an excellent description of the quantum noise evolution for almost all experimentally reasonable conditions. The linearized approximation treats quantum and classical noise in almost identical manners, thereby emphasizing that, for almost all practical purposes, quantum noise can be thought of in classical terms.

### 3.2.1 Linearized Equations of Motion

The quantum envelope introduced in Section 2.2 and in Appendix B can be decomposed as

$$\hat{A}(z,\tau) = \left\langle \hat{A}(z,\tau) \right\rangle + \hat{a}(z,\tau). \tag{3.13}$$

We insert this expression in the envelope evolution equation (B.33) and we treat $\hat{a}$ as a small quantity. Equations for the mean field and for $\hat{a}$ are obtained from the zeroth and first order Taylor expansion of the resulting equation. It can be seen in particular that the mean field obeys the classical envelope equation. For this reason we will denote

$$A(z,\tau) = \left\langle \hat{A}(z,\tau) \right\rangle \tag{3.14}$$

and we shall refer to $A(z,\tau)$ as the classical field, normalized to the photon flux. Note that $z$ and $\tau$ are the propagation distance and the retarded time respectively. We

therefore have [53, 54, 55]

$$\frac{\partial A(z,\tau)}{\partial z} = (D + iN(z,\tau))\, A(z,\tau), \tag{3.15}$$

where the linear dispersion operator is given by

$$D = -i\frac{\beta_2}{2}\frac{\partial^2}{\partial\tau^2} + \frac{\beta_3}{6}\frac{\partial^3}{\partial\tau^3} + \dots . \tag{3.16}$$

The constants $\beta_i$ are defined from a Taylor expansion of the dispersion relation around the carrier frequency

$$\beta(\omega) = \beta_0 + \frac{1}{v_g}(\omega - \omega_0) + \frac{\beta_2}{2}(\omega - \omega_0)^2 + \frac{\beta_3}{6}(\omega - \omega_0)^3 + \dots . \tag{3.17}$$

The bandwidth of the pulse determines the number of terms that must be retained in this expansion. If $T$ denotes the pulse duration, one can define characteristic lengths scales for each term in the dispersion operator[54]

$$L_n = \frac{T^n}{|\beta_n|} \tag{3.18}$$

These length scales provide a rough estimate of the propagation distances over which the corresponding operators affect significantly the evolution of the pulse. In standard silica fibers, $\beta_2$ takes negative values for carrier wavelengths longer than about $1.3\mu m$ and positive values at shorter wavelengths. For this reason, $1.3\mu m$ is often called the zero-dispersion wavelength. Typically, $\beta_2$ is $35ps^2/km$ at $0.8\mu m$ and $-20ps^2/km$ at $1.55\mu m$, corresponding to $L_2$'s in the tens of meters for picosecond pulses. In contrast, $\beta_3$ is typically of the order of $0.1ps^3/km$ in the same wavelength window, corresponding to $L_3 \simeq 10km$ for picosecond pulses. In general therefore, high order dispersion terms are not significant for pulses longer than $0.1ps$, unless one operates very close to the zero dispersion wavelength and at low intensities.

The nonlinear Kerr operator in (3.15) is

$$N(z,\tau) = \int_0^\infty d\tau' h(\tau') \left|A(z,\tau-\tau')\right|^2, \tag{3.19}$$

with a response function

$$h(\tau) = 0.8\kappa\delta(\tau) + h_R(\tau). \tag{3.20}$$

In Section B.6 we assumed an instantaneous response function

$$N(z,\tau) = \kappa \left|A(z,\tau)\right|^2, \tag{3.21}$$

which is appropriate for pulses longer than about $1ps$. The construction of a self-consistent quantum theory of pulse propagation in Kerr media with a finite response time is postponed until Chapter 4. Here we included an explicit response function in $N(z,\tau)$ to discuss issues connected with the numerical approach developed in Section 3.3. Both terms in (3.20) describe the intensity-dependent refractive index of fused silica. The first term is the electronic contribution with a response time much shorter that the pulse duration. The second term is due to molecular degrees of freedom with frequencies in the terahertz range. An explicit expression for $h_R(\tau)$ is available from Raman gain measurements (Section 4.1.2). The Kerr coefficient $\kappa$, which controls the magnitude of the overall nonlinearity, is given by

$$\kappa \equiv \int d\tau h(\tau) = \frac{\hbar\omega_0^2 n_2}{cA_{eff}}, \tag{3.22}$$

where $n_2 = 3.2 \times 10^{-16}\ cm^2/W$ is the nonlinear index coefficient of fused silica and $A_{eff}$ is the effective area of the propagating mode. In the units chosen here, $\kappa$ varies roughly between $2 \times 10^{-19}\ s/km$ and $9 \times 10^{-19}\ s/km$, depending on the mode field diameter. In a fiber with $A_{eff} = 65\ \mu m^2$, we find for example $\kappa \simeq 3.7 \times 10^{-19}\ s/km$ at a carrier wavelength $\lambda = 1.3\ \mu m$. A length scale can be defined beyond which the

action of the nonlinear term becomes important[54]

$$L_N = \frac{1}{\kappa |A(0,0)|^2}. \tag{3.23}$$

With the above values for $\kappa$ and $\lambda$, a pulse with a peak power of $1kW$ has a peak photon flux of $6.5 \times 10^{21} s^{-1}$, corresponding to a nonlinear length of $43cm$. In practice, single-mode peak powers in excess of $100kW$ can be achieved directly out of femtosecond modelocked lasers. Post-amplification of these pulses can lead to peak powers in the megawatt region and beyond. It is clear that when these pulses are coupled into a fiber, nonlinearities dominate their evolution, at least initially.

In (3.13), the quantum fluctuation operator obeys the commutation relations

$$[\hat{a}(z,\tau), \hat{a}(z,\tau')] = 0 \quad ; \quad \left[\hat{a}(z,\tau), \hat{a}^\dagger(z,\tau')\right] = \delta(\tau - \tau'). \tag{3.24}$$

We are interested in the moments of this operator after it has propagated a distance $z$, given that its statistics is known in the input plane. Typically, the quantum operator is in vacuum at $z = 0$

$$\hat{a}(0,\tau)|in>= 0. \tag{3.25}$$

This condition guarantees that the total envelope field operator, $\hat{A} = A + \hat{a}$, is in a coherent state with a mean field $A$. This condition is not essential however, and more general input noise conditions can be considered. Isolating terms linear in the fluctuations in (B.33), we find

$$\begin{aligned} \frac{\partial \hat{a}(\tau)}{\partial z} &= (D + iN(\tau))\,\hat{a}(\tau) \\ &+ iA(\tau)\int_{-\infty}^{\tau} d\tau' h(\tau - \tau')\left\{A^*(\tau')\hat{a}(\tau') + A(\tau')\hat{a}^\dagger(\tau')\right\} \\ &+ i\hat{m}(\tau)A(\tau). \end{aligned} \tag{3.26}$$

The $z$-dependence of the fields was omitted. On the last line of this equation, a phase noise source, $\hat{m}(z,\tau)$ was added. This term was notderived directly from (B.33). It arises from the finite response time of the Kerr nonlinearity, and its introduction will

be justified in the next chapter. For the purpose of the present discussion, we note that

$$[\hat{m}(z,\tau), \hat{a}(z',\tau')] = 0, \tag{3.27}$$

for $z' \leq z$. The phase noise vanishes when the response function is instantaneous.

Equations (3.15) and (3.26) are the field equations of the linearized noise theory. The first equation describes the evolution of the classical "pump" field unaffected by quantum noise. The second equation indicates how the pump, acting as an external driving field, couples the creation and annihilation operators of the noise. For general dispersion conditions, this set of equations must be solved numerically. The evolution of intense pulses at zero dispersion will however be dominated by the nonlinearity of the fiber and a closed-form solution can be found.

### 3.2.2 Instantaneous Zero-Dispersion Solution

Consider the above equations for $D = 0$ and $h(\tau) = \kappa\delta(\tau)$ [31]

$$\frac{\partial A}{\partial z} = i\kappa |A|^2 A, \tag{3.28}$$

$$\frac{\partial \hat{a}}{\partial z} = 2i\kappa \mid A \mid^2 \hat{a} + i\kappa A^2 \hat{a}^\dagger. \tag{3.29}$$

If $\alpha(\tau) = A(0,\tau)$ denotes the input envelope and if we define the instantaneous nonlinear phase shift by

$$\phi(z,\tau) \equiv \kappa z |\alpha(\tau)|^2 = zN(0,\tau), \tag{3.30}$$

the envelope and the noise operator at the output of the fiber can be written as

$$A(z,\tau) = e^{i\phi(z,\tau)}\alpha(\tau), \tag{3.31}$$

$$\hat{a}(z,\tau) = e^{i\phi(z,\tau)}\left\{\mu(z,\tau)\hat{a}(0,\tau) + \nu(z,\tau)\hat{a}^\dagger(0,\tau)\right\}, \tag{3.32}$$

where

$$\mu(z,\tau) = 1 + i\phi(z,\tau), \tag{3.33}$$

$$\nu(z,\tau) = i\kappa z\alpha^2(\tau). \tag{3.34}$$

Consider the quadratures $\hat{Q}_\theta(z)$ defined by (3.10). Introducing (3.31) and (3.32) in (3.10), we find

$$\hat{Q}_\theta(z) = \int d\tau \left\{ B_\theta^*(z,\tau)\hat{a}(0,\tau) + B_\theta(z,\tau)\hat{a}^\dagger(0,\tau) \right\}, \tag{3.35}$$

where

$$B_\theta(z,\tau) = \frac{1}{\sqrt{2n_0}} \left\{ \alpha(\tau)\mu^*(z,\tau)e^{i\theta} + \alpha^*(\tau)\nu(z,\tau)e^{-i\theta} \right\}. \tag{3.36}$$

When the input noise is in vacuum, the expectation value of $\hat{Q}_\theta$ vanishes. We also have in this case

$$\left\langle \Delta^2 \hat{Q}_\theta(z) \right\rangle = \int d\tau |B_\theta(z,\tau)|^2 = \frac{1 + 4p_6\Phi^2 \sin^2\theta + 2p_4\Phi \sin 2\theta}{2}, \tag{3.37}$$

where

$$\Phi(z) = \phi(z,0) = \kappa z \left|\alpha(0)\right|^2 \tag{3.38}$$

is the peak nonlinear phase shift. The pulse-shape dependent parameters $p_n$ are defined as

$$p_n = \frac{1}{n_0|\alpha(0)|^{n-2}} \int d\tau |\alpha(\tau)|^n. \tag{3.39}$$

For sech, gaussian and square pulses (see Appendix C), we find $(p_4, p_6) = (2/3, 8/15)$, $(1/\sqrt{2}, 1/\sqrt{3})$ and $(1,1)$ respectively. At the input of the fiber where $\Phi = 0$, we recover the shot-noise or vacuum level (see (2.52)). For $\Phi > 0$, the magnitude of the quadrature fluctuations depends on the relative phase $\theta$. Using (3.11) and (3.37), we find

$$R_{SPM}^{lin}(z) = 1 + 2p_6\Phi^2 - \sqrt{(2p_6\Phi^2)^2 + (2p_4\Phi)^2}. \tag{3.40}$$

This function is displayed on Fig. 3-3 for gaussian and square pulses. It is clear from

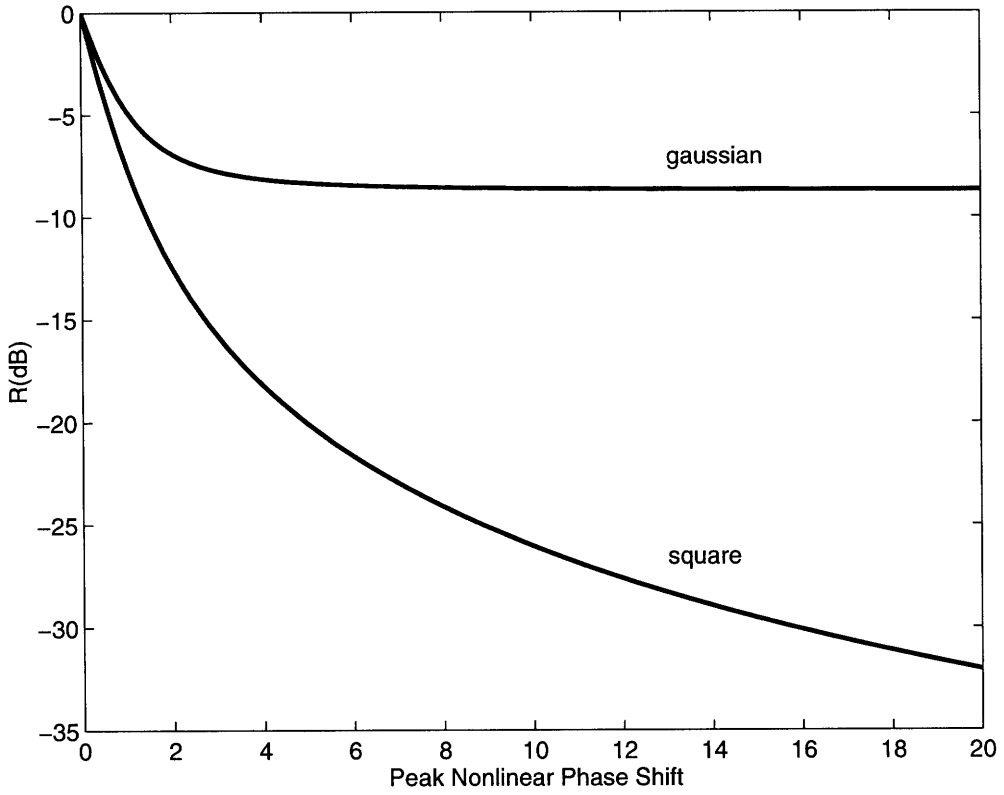


Figure 3-3: Linearized SPM squeezing at zero dispersion with instantaneous Kerr effect for gaussian and square input pulses.

this plot when $\Phi > 0$, one can find quadratures of the field with fluctuation levels below that of the vacuum. Another important property of SPM squeezing is also evident. We first note that (3.40) saturates at large nonlinear phase shifts to

$$R_{SPM} \longrightarrow 1 - \frac{p_4^2}{p_6}. \tag{3.41}$$

This limit, for sech, gaussian and square pulses, is 0.167 ($-7.78dB$), 0.134 ($-8.73dB$) and 0 respectively. Hence, the linearized theory predicts that arbitrarily large degrees of squeezing can be achieved with square pulses. Squeezing becomes less efficient as the leading and trailing edges of the pulse fall to zero less abruptly and as the intensity of the disturbance becomes less uniform. To explain the saturation in squeezing occurring when the pulse is not square, we return to (2.59). We note that in the present case, the phases of $f$ and $\nu$ are constants (remember that the overall phase in (3.31) and (3.32) cancel in $\hat{Q}_\theta$), whereas the phase of $\mu$, given by $\arctan\phi(z,\tau)$, varies across the pulse. Hence, the local oscillator used in defining the quadrature $\hat{Q}_\theta$ does not have the optimum phase profile, unless $\alpha(\tau)$ is square. As $\Phi$ increases,

the spread between the phases of $\mu$ at the peak and in the wings of the pulse widens, and the choice of $\theta$ in (3.37) will inevitably select noisy instantaneous quadratures for some values of $\tau$. This leads to the saturation of $R(z)$. It is interesting to note that this phenomenon occurs even though squeezing on any individual portion of the pulse becomes arbitrarily large. This indicates once more that it is easier to produce squeezing than to measure and use it.

It is experimentally difficult to create pulses with square profiles while maintaining appreciable peak powers. Modelocked lasers produce instead sech or gaussian pulses [56, 57]. Bergman et al. [20, 32, 33] performed a series of squeezing experiments where the conditions for $D \simeq 0$ were met. A Nd:YAG laser operating at $1.33\mu m$ was used, producing $15ps$ gaussian pulses with a peak power close to $25W$. The propagation length in the experiments was $50m$, leading to a peak nonlinear phase shift $\Phi \simeq 4$. The authors observed $5.1dB$ of quadrature noise reduction with this set-up. Consider on the other hand the limit (3.41) imposed on zero-dispersion squeezing for gaussian pulses. Taking into account the overall losses in the system independently estimated at 15%, and using (A.2), we find a saturation level of $-5.8dB$. Hence, the MIT squeezer operates very close to this limit and little room is left for improvement at zero dispersion. It was suggested to use a local oscillator with a duration much shorter than the squeezing pulse in order to take full advantage of the large degree of squeezing occurring at its peak. So far this idea has not been tested successfully.

## 3.3 Dispersive Squeezing in Fibers

In order to overcome the saturation limit associated with gaussian pulses at zero dispersion, we investigate in this section the use of pulses with carrier frequencies different from $1.3\mu m$. Since no analytic solution to (3.15) and (3.26) exists in general, we turn to numerical simulations.

### 3.3.1 Parametric Green's Functions

We first note that the linear equation (3.26) implies a relationship between the input and output noise operators of the form

$$\begin{aligned}\hat{a}(z,\tau) &= \int_{-\infty}^{\infty} d\tau' \left\{\mu(z,\tau;\tau')\hat{a}(0,\tau') + \nu(z,\tau;\tau')\hat{a}^{\dagger}(0,\tau')\right\} \\ &+ \int_{-\infty}^{\infty} d\tau' \int_{0}^{z} dz' \; \alpha(z,\tau;z',\tau')\hat{m}(z',\tau'). \end{aligned} \tag{3.42}$$

The first two terms in this expression represent vacuum fluctuations entering the fiber at $z = 0$ and transformed by their propagation through the fiber. The inhomogeneous term in (3.42) represents the contribution to the optical noise from Raman scattering. It is important to note that the slowly varying envelope approximation implicit in (3.15) neglects backward traveling Fourier components of the optical field. Moreover, Raman fluctuations at different locations of the waveguide are, by construction, totally decoupled. There is therefore no mechanism within our theory by which the optical field at $z$ can be affected by the noise operator at $z' > z$. For this reason, the spatial integral in (3.42) extends only from 0 to $z$.

The Green's functions $\mu$, $\nu$ and $\alpha$ contain the whole dynamical information on the noise evolution. It is convenient to express these functions in vector form. We first define

$$G(z,\tau;\tau') = \begin{pmatrix} \mu(z,\tau;\tau') \\ \nu^{*}(z,\tau;\tau') \end{pmatrix}, \tag{3.43}$$

with the boundary condition

$$G(0,\tau;\tau') = \begin{pmatrix} \delta(\tau-\tau') \\ 0 \end{pmatrix}. \tag{3.44}$$

Introducing (3.42) into (3.26), and isolating the coefficients of $\hat{a}(0,\tau)$ and $\hat{a}^{\dagger}(0,\tau)$, we find that $G$ obeys

$$\frac{\partial G(z,\tau;\tau')}{\partial z} = \left(\bar{D} + M\right) \cdot G(z,\tau;\tau'), \tag{3.45}$$

where we introduced the notation

$$\left(\bar{D}+M\right)\cdot G(z,\tau;\tau') \equiv \int d\tau''\left(\bar{D}(\tau-\tau'')+M(z,\tau;\tau'')\right)G(z,\tau'',\tau'), \tag{3.46}$$

and we defined

$$\begin{aligned}
\bar{D}(\tau-\tau') &= \delta(\tau-\tau')\begin{pmatrix} D & 0 \\ 0 & D^* \end{pmatrix}, && (3.47)\\
M(z,\tau;\tau') &= i\delta(\tau-\tau')N(\tau)\sigma_3 \\
&+ ih(\tau-\tau')\sigma_3\begin{pmatrix} A(\tau)A^*(\tau') & A(\tau)A(\tau') \\ A^*(\tau)A^*(\tau') & A^*(\tau)A(\tau') \end{pmatrix}, && (3.48)
\end{aligned}$$

with

$$\sigma_3 = \begin{pmatrix} 1 & 0 \\ 0 & -1 \end{pmatrix}. \tag{3.49}$$

All the fields on the right hand side of (3.48) are evaluated at $z$. Similarly, isolating the coefficient of $\hat{m}(z',\tau')$ in (3.26), we find that

$$H(z,\tau;z',\tau') = \begin{pmatrix} \alpha(z,\tau;z',\tau') \\ \alpha^*(z,\tau;z',\tau') \end{pmatrix}, \tag{3.50}$$

also obeys (3.45) for all $\tau'$ and for $z > z'$. The boundary condition for $H$ is

$$H(z,\tau;z,\tau') = i\delta(\tau-\tau')\sigma_3\begin{pmatrix} A(z,\tau) \\ A^*(z,\tau) \end{pmatrix}. \tag{3.51}$$

At this point, we have reduced the linearized quantum theory to the set of classical equations (3.15), and (3.45)[91, 92]. We show below how to solve these equations numerically.

### 3.3.2 Split-Step Formulae

We first show that the symmetrized split-step formula discussed in [54, 89, 90] can be generalized to the case where the nonlinearity has a delayed component. From (3.15) and from Taylor expansion, we have

$$A(z+\Delta z) = \left[1 + \Delta z(D+iN) + \frac{\Delta z^2}{2}(D+iN)^2\right] A(z) + \frac{i\Delta z^2}{2}\frac{\partial N}{\partial z}A(z) + O(\Delta z^3), \tag{3.52}$$

where $O(\Delta z^3)$ represents terms of order $\Delta z^3$. The terms within brackets provide an expansion of $\exp(\Delta z(D+iN))$, which would be the exact evolution operator if $N$ were $z$-independent. The spatial derivative of $N$ is obtained from (3.19) using the evolution equation

$$\frac{\partial N(z,\tau)}{\partial z} = \int_0^\infty d\tau' h(\tau-\tau')\left\{D^*A^*(z,\tau')A(z,\tau') + A^*(z,\tau')DA(z,\tau')\right\}. \tag{3.53}$$

The absence of nonlinear contribution on the right hand side of this equation allows (3.52) to be recovered from the following formula

$$A(z+\Delta z) = \exp\left(\frac{\Delta z}{2}D\right)\exp\left(i\Delta z\tilde{N}(z,\tau)\right)\tilde{A}(z) + O(\Delta z^3), \tag{3.54}$$

where operators with a "tilde" are obtained from the "untilde" operators by replacing $A$ with

$$\tilde{A}(z,\tau) \;=\; \exp\left(\frac{\Delta z}{2}D\right)A(z,\tau). \tag{3.55}$$

Explicitly, we have

$$\tilde{N}(\tau) = N(\tau) + \frac{\Delta z}{2}\int_0^\infty d\tau' h(\tau-\tau')\left\{D^*A^*(\tau')A(\tau') + A^*(\tau')DA(\tau')\right\} + O(\Delta z^3), \tag{3.56}$$

where the $z$-dependence was omitted. Expanding each factor in (3.54) up to terms of order $\Delta z^2$, we recover (3.52). Formula (3.54) presents three advantages from a numerical standpoint. First, compared to (3.52), it separates the dispersive and

nonlinear operations into a product of operators, and therefore reduces the number of times one has to alternate between the time and frequency domains. Second, the input of each factor in (3.54) is the output of the previous one. This property leads to a numerical code "marching forward", and is therefore easy to implement. Finally, one can regroup the half steps of dispersion at the end and the beginning of adjoining intervals into a single dispersive "joint leap", thus increasing by almost 50% the speed of the code. In [91], a simpler un-symmetrized split-step formula was used in the case where the nonlinearity is instantaneous

$$A(z+\Delta z) = \exp\left(\Delta z D\right) \exp\left(i\Delta z N(z,\tau)\right) A(z) + O(\Delta z^2). \tag{3.57}$$

One easily verifies that this formula is only accurate to first order.

Consider now the solution of equation (3.45) to second order in $\Delta z$. Once again, we have

$$G(z+\Delta z) = \exp\left(\Delta z(\bar{D}+M)\right) \cdot G(z) + \frac{\Delta z^2}{2}\frac{\partial M}{\partial z} \cdot G(z) + O(\Delta z^3). \tag{3.58}$$

Contrary to the previous case however, the spatial derivative of $M$ is not governed entirely by dispersion. We find instead $\partial M/\partial z = (\partial M/\partial z)_{lin} + (\partial M/\partial z)_{nlin}$, where the first term in this expression is the contribution from the dispersive terms, and

$$\begin{aligned}\left(\frac{\partial M(\tau;\tau')}{\partial z}\right)_{nlin} = & - h(\tau-\tau')\left(N(\tau)-N(\tau')\right)\begin{pmatrix} A(\tau)A^*(\tau') & 0 \\ 0 & A^*(\tau)A(\tau') \end{pmatrix} \\ & - h(\tau-\tau')\left(N(\tau)+N(\tau')\right)\begin{pmatrix} 0 & A(\tau)A(\tau') \\ A^*(\tau)A^*(\tau') & 0 \end{pmatrix}.\end{aligned}$$

All the fields are evaluated at $z$. In the absence of nonlinear contribution to $\partial M/\partial z$, one could derive a formula identical to (3.54) for $G(z+\Delta z)$. Adding a correction for the nonlinear term, we have

$$G(z+\Delta z) = \exp\left(\frac{\Delta z}{2}\bar{D}\right) \cdot \left[\exp\left(\Delta z\tilde{M}\right) + \frac{\Delta z^2}{2}\left(\frac{\partial \tilde{M}}{\partial z}\right)_{nlin}\right] \cdot \tilde{G}(z) + O(\Delta z^3), \tag{3.59}$$

where we defined

$$\tilde{G}(z,\tau;\tau') = \exp\left(\frac{\Delta z}{2}\bar{D}\right)\cdot G(z,\tau;\tau'). \tag{3.60}$$

Formula (3.59) offers the same advantages as (3.54) from a numerical point of view. It can be written in the following, more useful way

$$G(z+\Delta z) = \exp\left(\frac{\Delta z}{2}\bar{D}\right)\cdot\exp\left(\Delta z\tilde{N}(z)\sigma_3\right)\cdot\left(1+\Delta z\tilde{K}\right)\cdot\tilde{G}(z)+O(\Delta z^3), \tag{3.61}$$

where

$$K(z,\tau;\tau'') = ih(\tau-\tau'')\begin{pmatrix} A(z,\tau) \\ A^*(z,\tau)\end{pmatrix}(A^*(z,\tau''),A(z,\tau'')). \tag{3.62}$$

Once again we note that in [91], a simpler first-order formula was proposed for the instantaneous case

$$G(z+\Delta z) = \exp\left(\Delta z\bar{D}\right)\cdot\exp\left(\Delta z M\right)\cdot G(z)+O(\Delta z^2), \tag{3.63}$$

The split-step formulae (3.54) and (3.61) are the main results of this section. To test their accuracy, we define the error functions for the field

$$\Delta_A(\Delta z) = \sqrt{\int d\tau\,|A_{\Delta z}(\tau)-A(\tau)|^2}, \tag{3.64}$$

and for the Green's function

$$\Delta_G(\Delta z) = \sqrt{\int d\tau d\tau'\left\{|\mu_{\Delta z}(\tau;\tau')-\mu(\tau;\tau')|^2+|\nu_{\Delta z}(\tau;\tau')-\nu(\tau;\tau')|^2\right\}}. \tag{3.65}$$

In these expressions, the functions with a subscript are evolved with the split-step formulae using a step size $\Delta z$, and the functions without subscript represent the exact solutions to the field equations. We approximate the latter with the split-step formulae by using a very fine step size. Fig.3-4 and Fig.3-5 show $\Delta_A$ and $\Delta_G$ respectively as functions of $\Delta z$, for the first- and second-order formulae presented above. The slopes on these log-log plots indicate the power dependence on the step size of the numerical error and confirm the second order accuracy of (3.54) and (3.61). Note

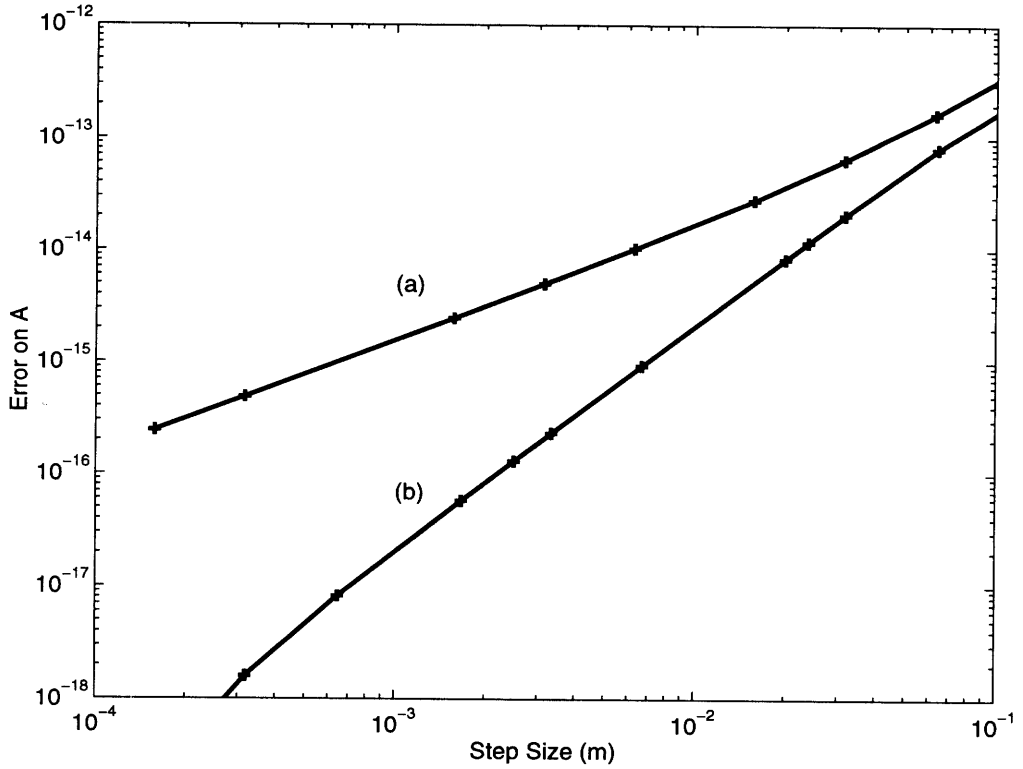


Figure 3-4: Field error $\Delta_A$ as a function of step-size. (a) first-order code based on (3.57), (b) second-order code based on (3.54).

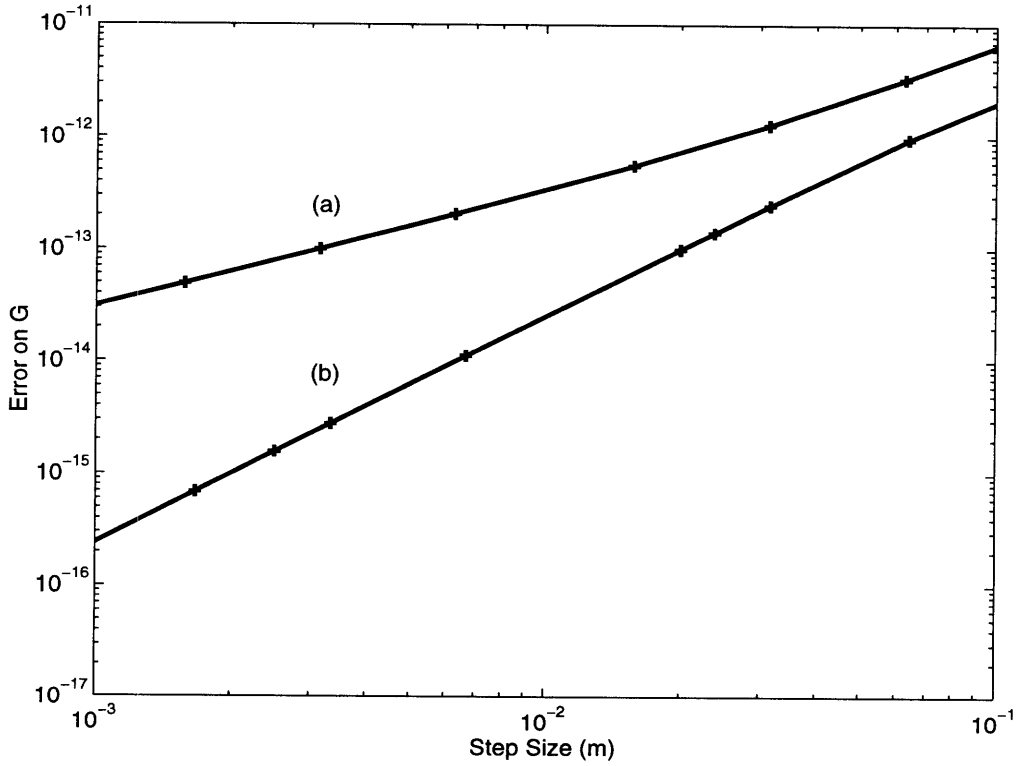


Figure 3-5: Green's function error $\Delta_G$ as a function of step-size. (a) first-order code based on (3.63), (b) second-order code based on (3.61).

that for a given distance, the number of propagation steps is inversely proportional to the step size, so that $\Delta_A$ and $\Delta_G$ from the second order code depend on $\Delta z^2$.

### 3.3.3 Dispersive Squeezing

We now use the above code to predict squeezing levels in the presence of dispersion. Using (3.10) and (3.42), we have

$$\begin{aligned}\hat{Q}_\theta(z) &= \int d\tau' \left\{B_\theta^*(z,\tau')\hat{a}(0,\tau') + B_\theta(z,\tau')\hat{a}^\dagger(0,\tau')\right\} \\ &+ \int d\tau' \int_0^z dz'\, C_\theta(z,\tau',z')\hat{m}(z',\tau'),\end{aligned} \tag{3.66}$$

where (see (3.36))

$$B_\theta(z,\tau') = \frac{1}{\sqrt{2n_0}} \int d\tau \left\{A(z,\tau)\mu^*(z,\tau;\tau')e^{i\theta} + A^*(z,\tau)\nu(z,\tau;\tau')e^{-i\theta}\right\} \tag{3.67}$$

is the local oscillator backpropagated with the adjoint system [87, 88] and

$$C_\theta(z,\tau',z') = \frac{1}{\sqrt{2n_0}} \int d\tau \left\{A(z,\tau)\alpha^*(z,\tau;z',\tau')e^{i\theta} + A^*(z,\tau)\alpha(z,\tau;z',\tau')e^{-i\theta}\right\}. \tag{3.68}$$

The two noise sources affecting the field are independent and contribute separately to the variance of the output quadrature. The noise reduction ratio is therefore

$$R_{SPM}^{lin}(z) = 2\min_\theta \left\langle \Delta^2 \hat{Q}_v(\theta,z)\right\rangle + 2\min_\theta \left\langle \Delta^2 \hat{Q}_R(\theta,z)\right\rangle, \tag{3.69}$$

where the factors 2 arise from the normalization of $R_{SPM}$ to the vacuum level (see (2.52)). The evolved vacuum variance is

$$\left\langle \Delta^2 \hat{Q}_v(\theta,z)\right\rangle = \int_{-\infty}^{\infty} d\tau \left|B_\theta(z,\tau)\right|^2, \tag{3.70}$$

and the Raman noise contribution is

$$\left\langle \Delta^2 \hat{Q}_R(\theta,z)\right\rangle = \int_{-\infty}^{\infty} \frac{d\omega}{2\pi}\, \bar{h}_R''(\omega)\coth\left(\frac{\hbar\omega}{2kT}\right) \int_0^z dz' \left|C_\theta(z,\omega,z')\right|^2. \tag{3.71}$$

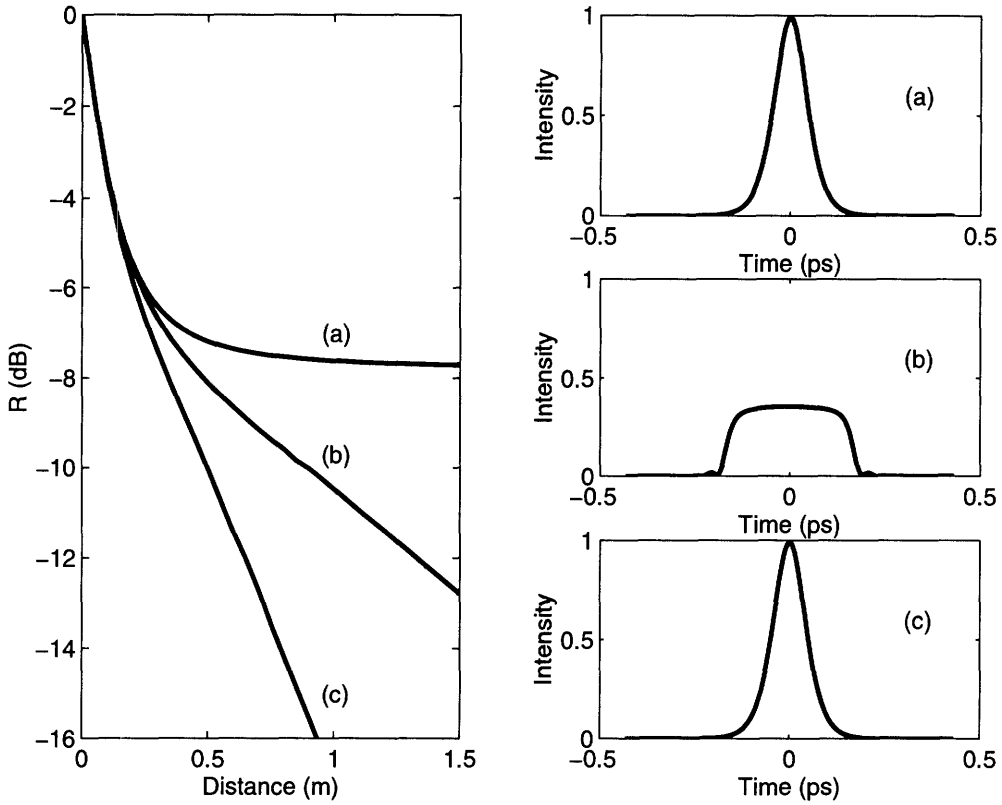


Figure 3-6: Linearized SPM squeezing with sech pulses. (a) zero-dispersion, (b) positive dispersion ($\beta_2 = 1ps^2/km$), (c) soliton ($\beta_2 = -20ps^2/km$). The $100fs$ input pulses were identical in all three cases. The inserts show the output envelopes.

In this last expression, we defined

$$C_\theta(z,\omega,z') = \int d\tau \exp(i\omega\tau) C_\theta(z,\tau,z'), \tag{3.72}$$

$$\bar{h}''_R(\omega) = \int d\tau \sin(\omega\tau) h_R(\tau). \tag{3.73}$$

Figure 3-6 displays $R^{lin}_{SPM}(z)$ for three dispersion coefficients. The input pulse in all cases was a sech with a $100fs$ duration. An instantaneous response function, $h(\tau) = \kappa\delta(\tau)$ was assumed. The curve labelled (c) in this figure corresponds to the formation of an optical soliton [58, 59, 60]. The conditions for the formation of such pulses are met when $\beta_2$ is negative ($\lambda > 1.3\mu m$) and when the pulses are long enough for the higher order dispersion terms to be negligible [61, 62]. In this case, equation (3.15) is the well-known nonlinear Schrödinger equation which admits the solution[63]

$$A(z,\tau) = \sqrt{I_0} \exp\left(i\frac{\kappa z I_0}{2}\right) \text{sech}\left(\frac{\tau}{\sigma}\right), \tag{3.74}$$

where the peak flux and the pulse duration are related by the area theorem $\sigma\sqrt{I_0} = \sqrt{|\beta_2|/\kappa}$. An analytic solution for the noise reduction ratio can be found when the local oscillator is a specific combination of the adjoint functions associated with photon number and phase fluctuations [60, 64]. No closed-form expression exists however for $R^{lin}_{SPM}(z)$. As can be seen from Fig. 3-6, no saturation of squeezing arises in this case. This can be understood from (3.74) where, contrary to the phase $\phi(z,\tau)$ of the dispersionless case, the nonlinear phase shift $\kappa z I_0/2$ is independent from $\tau$. The soliton therefore acts as a unit, with a single nonlinear phase shift attached to the whole pulse. As for a square pulse, the phase of the integrated quadrature can therefore be chosen to satisfy the optimum squeezing condition everywhere across this pulse. Two experiments were carried out to test the soliton squeezing curve[34, 35] and resulted in poor results. The failure of these attempts was attributed to the noise performance of the color-center laser systems used in these experiments. Chapter 5 further discusses soliton squeezing beyond the linearized regime.

The curve labelled (b) in Fig. 3-6 was obtained assuming a positive dispersion coefficient. It can be seen that in this case too, no saturation is apparent. This phenomenon can be understood from Fig. 3-7 which shows the envelope of the pulse as it propagates through the fiber. This plot indicates that in the positive dispersion regime, the profile of the pulse evolves initially into a square. The squeezing properties being more uniform across the pulse, a larger integrated squeezing level results for the integrated quadrature. Contrary to the soliton case however, the pulse eventually disperses out and squeezing degrades.

The results presented in this section indicate that the saturation in squeezing associated with non-square input pulses at zero-dispersion can be avoided when dispersion is present. From an experimental point of view, the positive dispersion regime is particularly attractive. In this case, no obvious constraint on the energy of the initial pulse is apparent from our simulation. Soliton squeezing on the other hand requires pulses of well-defined energy for a given pulse duration and dispersion coefficient. For $500ps$ solitons in standard fibers ($\beta_2 = -20ps^2/km$) for example, the resulting peak power must be $125W$. Working with low power pulses is demanding for two reasons.

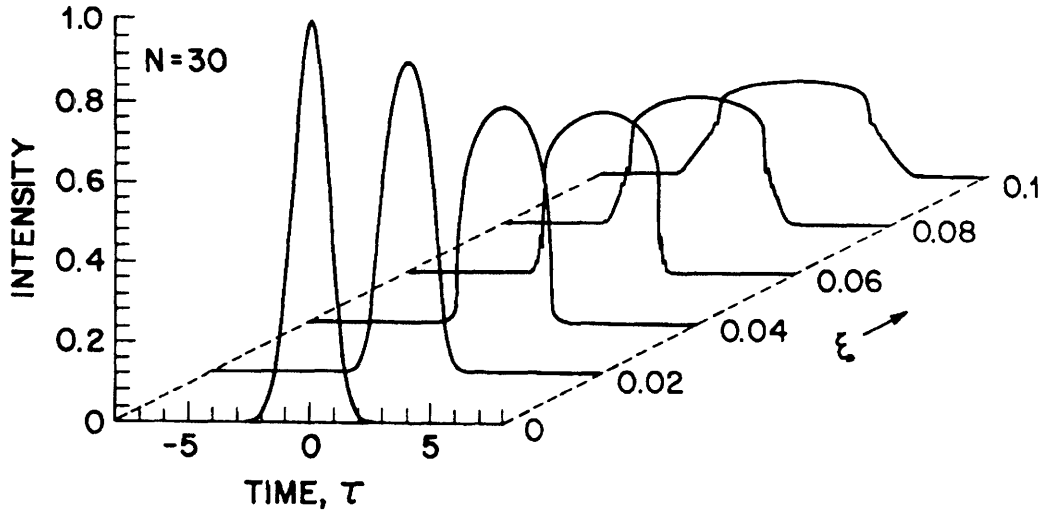


Figure 3-7: Evolution of an initially unchirped gaussian pulse in a medium with a positive dispersion coefficient. The distance is normalized to the dispersion length $L_2$ and the parameter $N = 30$ is roughly the ratio of the nonlinear length $L_N$ over the dispersion length $L_2$ After Ref.[54]

First, longer fiber loops are needed to achieve significant phase shifts. Second, the local oscillators derived from these pulses lead to lower shot noise levels unless high repetition rates are used. Eventually, the electronics noise floor of the detector becomes comparable to the shot noise level, and no squeezing can be measured. The positive dispersion regime is much more flexible in terms of peak powers. This fact, combined with the availability of powerful laser sources in the $800nm$ wavelength region make this regime very promising. Figure 3-8 shows the noise reduction ratio for a $100fs$ pulse with a peak power of $110kW$. Similar intensities and pulse durations can be achieved with KLM Ti:sapphire lasers. The dispersion coefficient was chosen to be appropriate for fused silica around $800nm$. As this plot indicates large degrees of squeezing can be achieved over a few centimeters.

All the curves presented so far were obtained from an instantaneous Kerr nonlinearity. For pulse durations of the order of $1ps$ or less, the finite response time of the nonlinearity must be taken into account. Although we indicated previously how to

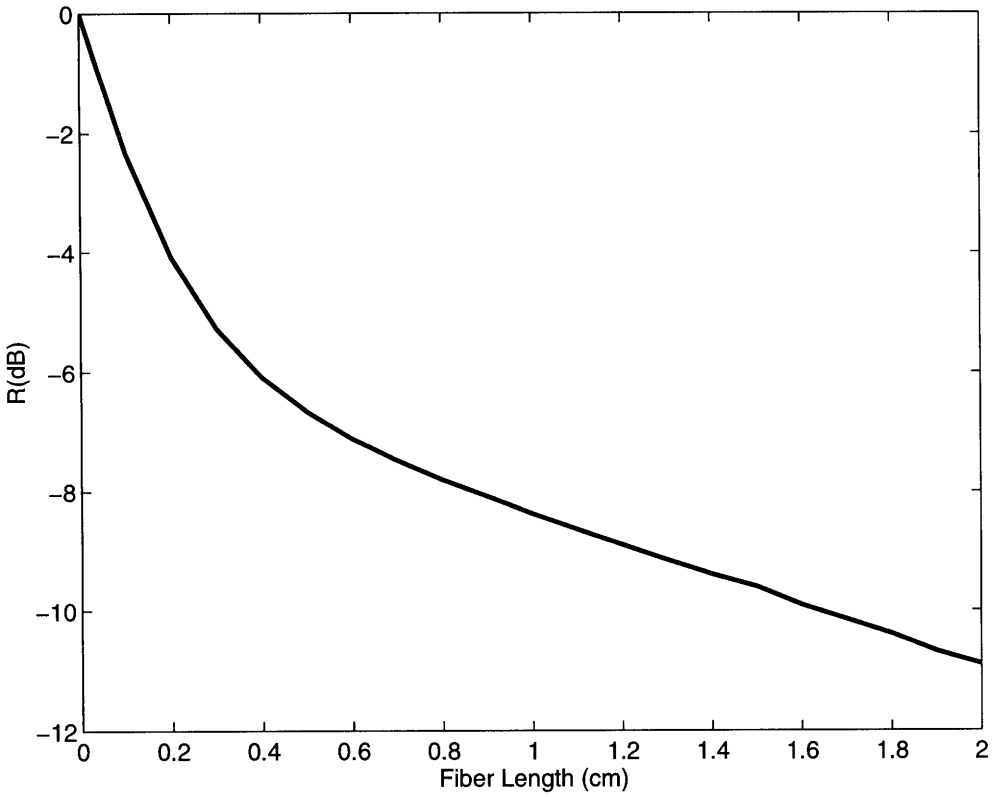


Figure 3-8: Linearized SPM squeezing with a $75fs$ sech pulse and a peak power of $150kW$. The dispersion coefficient was $\beta_2 = 34ps^2/km$.

modify our numerical code to take this effect into account, we did not yet provide expressions for $h_R$ and $\hat{m}$. This is in part the goal of the next chapter.

# Chapter 4

# Finite Response Time of the Kerr Effect

As we saw in Chapter 3, the operation of a fiber squeezer at wavelengths where the fiber is dispersive can lead to significant improvements in quadrature noise reduction for the output field. Due to the absence of squeezing saturation in this case, a clear advantage obtains when pulses with large peak powers are used. Very large pulse intensities are generally achieved with femtosecond sources. The evolution of such pulses in optical fibers is complicated by the finite response time of the Kerr nonlinearity. Section 4.1 presents a self-consistent quantum theory of short pulse propagation in optical fibers. We show that the equation of motion for the envelope contains a response function for the Kerr effect, and a Raman scattering noise source. These quantities are related to Raman gain in Section 4.1.2. In Section 4.2, a closed-form solution to the integro-differential, stochastic and nonlinear quantum envelope equation is found in the absence of dispersion. Non-perturbative expressions for various physical quantities are obtained from this solution. We compare these expressions to those obtained from the discretized-time model which will also be reviewed briefly. In Section 4.3, we consider the linearized limit of the nonlinear solution. A simple formula for $R_{SPM}^{lin}$ is obtained which applies to pulses of arbitrary duration and includes the effect of Raman noise. The domain of validity of the linearized theory is clarified and it is shown that the discretized-time model can be used to monitor departures

from this theory. The material of this chapter was published in [51, 65, 66].

## 4.1 Pulse Propagation in Raman Active Fibers

The envelopes of pulses with bandwidths larger than about 1THz, vary substantially over time intervals comparable with the response time of the Kerr nonlinearity. For these pulses, the intensity-dependent change of the refractive index cannot be assumed instantaneous as was done in Section B.6. As frequency components of the pulse beat and excite molecular resonances in the fused silica matrix, stimulated Raman scattering occurs. It is not immediately clear whether the advantage gained by using short and intense pulses in squeezing experiments still obtains when Raman scattering noise is taken into account. To clarify this point, we consider in more detail the dynamics of the nonlinear index change and we justify the equations introduced in Section 3.2.

### 4.1.1 Model for the Nonlinear Index

The Kerr effect in fibers arises from a change in the local refractive index of silica induced by the dynamics of material oscillators. This index change modifies the envelope equation of the linear dispersive medium (see (B.30)) to

$$\frac{\partial}{\partial z}\hat{A}(z,\tau) = D\hat{A}(z,\tau) + i\mu\hat{n}_{NL}(z,\tau)\hat{A}(z,\tau), \tag{4.1}$$

The Hermitean operator $\hat{n}_{NL}$ represents the electronic and molecular variables coupling to the envelope. The coupling constant $\mu$ is chosen so that $\hat{n}_{NL}$ measures the refractive index change. The dynamics of this operator is coupled to the optical field and, in general, depends on the intensity of the latter. Since optical nonlinearities are usually very weak, we can expand $\mu\hat{n}_{NL}$ to first order in $\hat{A}^\dagger\hat{A}$

$$\mu\hat{n}_{NL}(z,\tau) = \int_{-\infty}^{\infty} d\tau'\; h(\tau')\hat{I}(z,\tau-\tau') + \hat{m}(z,\tau). \tag{4.2}$$

where

$$\hat{I}(z,t) \equiv \hat{A}^{\dagger}(z,t)\hat{A}(z,t). \tag{4.3}$$

The function $h$ describes the delayed response of the index change to an applied optical field. By causality, the index at time $\tau$ can only be influenced by the field at earlier times, so that $h(\tau')$ must vanish when $\tau' < 0$. The hermitean operator $\hat{m}(z,\tau)$, on the other hand, describes the quantum and thermal fluctuations present in $\hat{n}_{NL}$ in the absence of optical field. Inserting expression (4.2) into the field equation for the envelope, (4.1), we find

$$\frac{\partial}{\partial z}\hat{A}(z,\tau) = \left\{D + i\int_{-\infty}^{\infty} d\tau'\, h(\tau')\hat{I}(z,\tau-\tau') + i\hat{m}(z,\tau)\right\}\hat{A}(z,\tau). \tag{4.4}$$

This equation describes the evolution of a pulse in a Kerr medium with a response function $h$. As can be seen, the index fluctuations represented by $\hat{m}$ translate into a source of phase noise for the optical field. The spectral properties of these fluctuations are closely tied to those of the response function. To specify this relation more precisely, we model the noise background as a collection of localized and independent harmonic oscillators

$$\hat{m}(z,\tau) = \int_0^{\infty} d\omega \frac{\sqrt{W(\omega)}}{2\pi}\left\{\hat{d}_{\omega}^{\dagger}(z)e^{i\omega\tau} + h.c.\right\}, \tag{4.5}$$

where the spectral weighting function $W(\omega)$ is, as yet, unspecified. The operators $\hat{d}_{\omega}(z)$ and $\hat{d}_{\omega}^{\dagger}(z)$ obey the commutation relation

$$\begin{aligned}\left[\hat{d}_{\omega}(z), \hat{d}_{\omega'}^{\dagger}(z')\right] &= \delta(\omega-\omega')\delta(z-z'),\\ \left[\hat{d}_{\omega}(z), \hat{d}_{\omega'}(z')\right] &= 0\end{aligned} \tag{4.6}$$

This model assumes that the material oscillators at different points do not interact. This is consistent with a picture where $\hat{n}_{NL}$ is created by localized molecular vibrations. At first sight, it seems that acoustical index fluctuations are excluded from our theory since they couple different parts of the waveguide. We note however that the

coherence length associated with acoustical modes in a fiber is very short[67] so that, in this case too, a spatial delta function correlation seems appropriate. The localized nature of the noise operator, combined with the slowly-varying envelope approximation, which neglects any coupling of the envelope to the backward propagating modes, imply that the noise operator at $z$ can only affect the field at $z > z'$. In particular, we have

$$\left[\hat{A}(z,\tau), \hat{m}(z,\tau')\right] = 0, \tag{4.7}$$

i.e, the field and the noise at a given point of the waveguide are independent degrees of freedom.

Recall from Appendix B that

$$[\hat{A}(z,\tau), \hat{A}(z,\tau')] = 0, \quad [\hat{A}(z,\tau), \hat{A}^\dagger(z,\tau')] = \delta(\tau - \tau'). \tag{4.8}$$

The spectral weight function $W(\omega)$ is determined by requiring that the commutation relations of the field be preserved by the equation of motion (4.4) [65, 68]. Consider the derivative of one of these commutators

$$\begin{aligned}\frac{\partial\left[\hat{A}(z,\tau), \hat{A}^\dagger(z,\tau')\right]}{\partial z} &\equiv \lim_{\Delta z\to 0}\frac{1}{\Delta z}\left\{\left[\hat{A}(z+\Delta z,\tau), \hat{A}^\dagger(z+\Delta z,\tau')\right]\right. \\ &\qquad \left. - \left[\hat{A}(z,\tau), \hat{A}^\dagger(z,\tau')\right]\right\}. \end{aligned}\tag{4.9}$$

Using the equation of motion, we have

$$\begin{aligned}\hat{A}(z+\Delta z) = \hat{A}(z) \;+\; &\Delta z\left(D + i\int_0^\infty d\tau' h(\tau')\hat{A}^\dagger(z,\tau-\tau')\hat{A}(z,\tau-\tau')\right)\hat{A}(z,\tau) \\ &+ i\int_z^{z+\Delta z} dz'\hat{m}(z',\tau)\hat{A}(z',\tau).\end{aligned}$$

Using this expression in (4.9), we find

$$\begin{aligned}\frac{\partial\left[\hat{A}(\tau), \hat{A}^\dagger(\tau')\right]}{\partial z} &= i\hat{A}^\dagger(\tau')\hat{A}(\tau)\left\{h(\tau-\tau') - h(\tau'-\tau)\right\} \\ &+ \frac{1}{\Delta z}\int_z^{z+\Delta z} dz'dz''\left[\hat{m}(z',\tau), \hat{m}(z'',\tau')\right]\hat{A}(z',\tau)\hat{A}^\dagger(z'',\tau').\end{aligned}$$

Since we require the derivative to vanish, we want

$$[\hat{m}(z,\tau),\hat{m}(z',\tau')] = -i\delta(z-z')\left\{h(\tau-\tau') - h(\tau'-\tau)\right\}. \tag{4.10}$$

Computing this commutator with (4.5) and (4.6), we find that the weight function must be given by

$$W(\omega) = 4\pi\bar{h}''(\omega) \geq 0, \tag{4.11}$$

where

$$\bar{h}''(\omega) = \int d\tau \sin(\omega\tau)h(\tau) \tag{4.12}$$

vanishes only if $h(\tau)$ is even. Since $h(\tau<0)=0$, the only possible symmetric response function is proportional to a delta function, which leads to a singular quantum field theory in the absence of dispersion (Section 4.2 and 4.3). With the above choice for $W(\omega)$, the commutator $\left[\hat{A},\hat{A}\right]$ is also preserved. We will show below that $\bar{h}''(\omega)$ is essentially the Raman gain for a signal propagating with a frequency $\omega_0-\omega$. The inequality $\bar{h}''(\omega>0)>0$, which is required for the hermiticity of $\hat{m}$ is then a stability condition verified experimentally by the positivity of the Raman gain on the Stokes side of the carrier frequency. Below, the material oscillators will be assumed in thermal equilibrium:

$$< \hat{d}^{\dagger}_{\omega}(z)\hat{d}_{\omega'}(z') >= \delta(\omega-\omega')\delta(z-z')n_{th}(\omega), \tag{4.13}$$

where $n_{th}(\omega) = (\exp(\hbar\omega/kT)-1)^{-1}$ is the Bose-Einstein distribution. The phase noise operator then has a gaussian statistics.

We close this paragraph by observing that the commutators (4.8) imply

$$[\hat{I}(z,\tau),\hat{I}(z,\tau')] = 0, \tag{4.14}$$

which indicates that the photon fluxes at two different times across the pulse are independent.

### 4.1.2 Kerr Response Function and Raman Gain

In the last paragraph, we showed how the spectral properties of $\hat{m}$ and $h$ were related. In this paragraph, we show how these quantities can be obtained from Raman gain measurements. Consider a field made of an intense pump at the carrier frequency and of a signal with frequency $\omega_s < \omega_0$

$$A(z,\tau) = A_p(z) + A_s(z)e^{i\Omega\tau}, \tag{4.15}$$

where

$$\Omega \equiv 2\pi\nu \equiv \omega_0 - \omega_s. \tag{4.16}$$

Experimentally, one observes that for $\nu$ between about $0.5THz$ and $75THz$, the signal is amplified by the pump. This phenomenon, called Raman amplification, occurs from the conversion of pump photons into signal photons, with the simultaneous excitation of Raman oscillators with frequencies in the terahertz range. The evolution of the signal in these conditions is described by the equation

$$\frac{\partial |A_s|^2}{\partial z} = \frac{G_0 \hbar\omega_0 |A_p|^2}{A_{eff}} g(\nu) |A_s|^2, \tag{4.17}$$

where $G_0$ is the peak Raman gain and where we neglected dispersion for simplicity. The measurements reported in [81] at a carrier wavelength of $795nm$ give $G_0 \simeq 1.2 \times 10^{-11} cm/W$. The function $g(\nu)$, which is dimensionless and equals 1 at its peak, is shown on Fig. 4-1 as a solid line. At low frequency, the curve fits $0.02\nu + 0.04\nu^3$, where $\nu$ is expressed in terahertz. Raman gain measurements were also reported in [79, 126]. The factor $\hbar\omega_0$ in the gain coefficient of (4.17) arises from the normalization of the envelope in units of photon flux.

The above gain equation can be derived directly from the envelope equation. We first introduce the decomposition (4.15) into equation (4.4), neglecting $D$ and $\hat{m}$ and interpreting all fields as classical functions. Isolating the coefficient of $e^{i\Omega\tau}$ in the

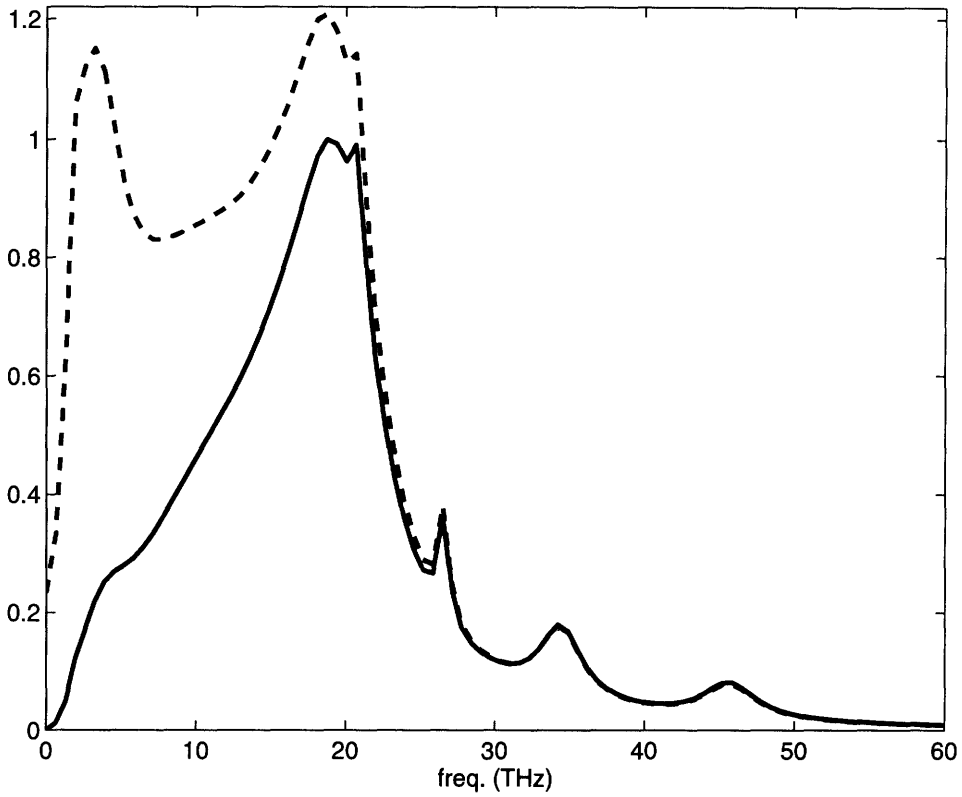


Figure 4-1: Raman power gain coefficient (solid line) and thermally enhanced Raman gain (dashed line). The latter is introduced in Section 4.2.3.

resulting equation, we find

$$\frac{\partial A_s}{\partial z} = i\left\{\kappa\left|A_s\right|^2 + \kappa_c\left|A_p\right|^2\right\}A_s + \bar{h}''(\Omega)\left|A_p\right|^2 A_s, \tag{4.18}$$

where $\kappa$ and $\kappa_c$ are the Kerr and cross Kerr coefficients respectively, and are given by

$$\kappa = \int d\tau h(\tau), \tag{4.19}$$

$$\kappa_c = \int d\tau h(\tau)\left(1+\cos(\Omega\tau)\right). \tag{4.20}$$

The function $\bar{h}''$ is defined by (4.12). From (4.18), we have

$$\frac{\partial\left|A_s\right|^2}{\partial z} = 2\bar{h}''(\Omega)\left|A_p\right|^2\left|A_s\right|^2. \tag{4.21}$$

Comparing (4.17) with (4.21), we find that $\bar{h}''$ is linearly related to the Raman gain coefficient

$$\bar{h}''(\Omega) = \hbar\omega_0\frac{G_0}{2A_{eff}}g\left(\nu\right). \tag{4.22}$$

The Kerr nonlinearity in fibers arises from two independent mechanisms. The first source of nonlinearity is of electronic origin and accounts for about 80% of the overall Kerr coefficient[125, 126]. This nonlinearity is extremely fast on the time scale of the envelope, even for femtosecond pulses. The second mechanism has its origin in the coupling of molecular vibrations to the optical field. As the separation between the nuclei of a molecule influence its susceptibility, a nonlinear dependence of the medium polarization arises. These two different mechanisms contribute separately to $h$

$$h(\tau) = h_e(\tau) + h_R(\tau), \tag{4.23}$$

where $h_e$ and $h_R$ are the electronic and molecular response functions respectively. $h_e$ should not be included in $\bar{h}''$ of (4.22). The electronic oscillators, which have frequencie higher than the carrier frequency of the pulse, cannot mediate Raman processes. Indeed, the latter would involve signal photons with negative frequencies. Instead, UV resonances are responsible for two-photon absorption. In principle, the two-photon absorption spectrum of fused silica [69]) can be used to determine $h_e$. Currently available pulses are too long however to resolve the details of this function which are therefore largely irrelevant. Instead, we used

$$h_e(\tau) = \frac{\kappa_e}{\tau_e} e^{-\tau/\tau_e}, \tag{4.24}$$

with a subfemtosecond response time $\tau_e = 0.5fs$. The constant $\kappa_e \simeq 0.8\kappa$ is the electronic contribution to the Kerr coefficient. One can verify that the imaginary part of the Fourier transform of this function essentially vanishes in the Raman gain window.

Returning to $h_R(\tau)$, we note that this function is real. We therefore have

$$h_R(\tau) = \int_{-\infty}^{\infty} \frac{d\Omega}{2\pi} \cos(\Omega\tau)\bar{h}'_R(\Omega) + \int_{-\infty}^{\infty} \frac{d\Omega}{2\pi} \sin(\Omega\tau)\bar{h}''_R(\Omega), \tag{4.25}$$

with $\bar{h}'_R(\omega) = \int d\tau \cos(\Omega\tau)h_R(\tau)$. Noting however that $h_R(\tau)$ vanishes at negative times, we find that the two integrals above are equal. The Raman response func-

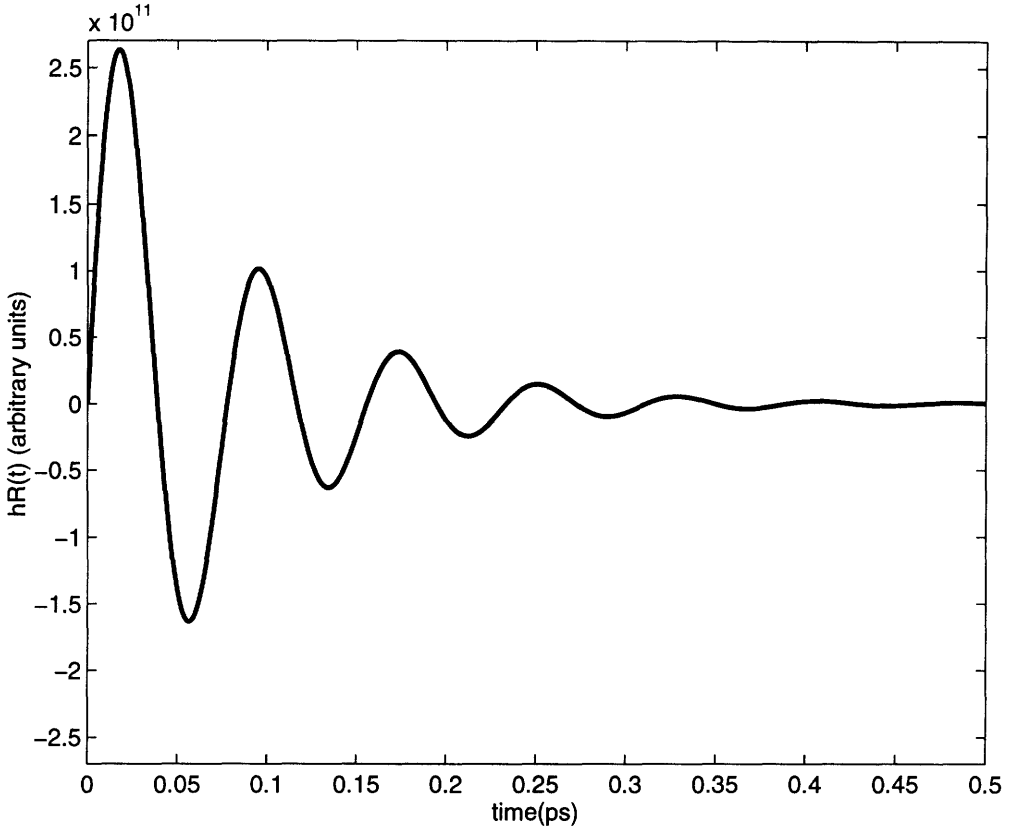


Figure 4-2: Raman response function of fused silica.

tion can therefore be expressed entirely in terms of $\bar{h}_R''$. Using the symmetry of the integrand and (4.22), we finally obtain[80]

$$h_R(\tau) = \hbar\omega_0 \frac{2G_0}{A_{eff}} \int_0^\infty d\nu \; g(\nu) \sin(2\pi\nu\tau). \tag{4.26}$$

Figure 4-2 shows the function $h_R$ corresponding to the Raman gain measurements of Fig. 4-1. Although this function shows structure extending up to $0.5ps$, its most important contribution occurs within $100fs$. Expressions (4.24) and (4.26) provide our explicit model for the response function. The function $\bar{h}_R''$ is also used in the spectral weight function $W$ given by (4.11) and therefore specifies the Raman noise operator needed to preserve the commutation relations of the field.

## 4.2 Closed-Form Solution at Zero Dispersion

In this section we consider the zero dispersion regime where a closed-form solution to the stochastic integro-differential equation (4.4) can be found[51, 65, 66]. We first note that the hermiticity of $\hat{n}_{NL}$, combined with $D = 0$, imply that $\hat{I}$ is $z$ independent.

This indicates that, even though the phase of the envelope is affected by the medium, the flux of photons travels unchanged at the group velocity. If all photons were of the same frequency, $\hat{I}$ would be proportional to the $z$-component of the Poynting vector. However, $\hat{A}(z,\tau)$ contains modes of a finite bandwidth coupled to the medium. Since photons can exchange energy with the medium and simultaneously change frequency, the conservation of the flux of photons does not imply the conservation of the energy of the pulses. Expressing the photon flux operator in terms of the input field, we have

$$\hat{I}(\tau) = \hat{A}_i^{\dagger}(\tau)\hat{A}_i(\tau). \tag{4.27}$$

Consider therefore the commutator of the index operator at different locations $z$ and $z'$, with $z \neq z'$

$$\begin{aligned}
[\hat{n}_{NL}(z,\tau), \hat{n}_{NL}(z',\tau')] &= \frac{1}{\mu^2}\int_0^{\infty} dsds' h(s)h(s') \left[I(s-\tau), I(s'-\tau')\right] \\
&+ \frac{1}{\mu^2}\left[\hat{m}(z,\tau), \hat{m}(z',\tau')\right] \\
&= 0,
\end{aligned} \tag{4.28}$$

where we used (4.7), (4.10) and (4.14). Nonlinear index operators at different locations along the waveguide are therefore independent. This allows (4.4) to be integrated without path ordering, as if $\hat{n}_{NL}$ were a $c$-number. We find the closed-form solution

$$\hat{A}(z,\tau) = \exp\left(i\mu\int_0^z dz'\ \hat{n}_{NL}(z',\tau)\right)\hat{A}_i(\tau). \tag{4.29}$$

Using again the fact that the Raman noise operator, $\hat{m}$ commutes with the photon flux operator, and assuming a fiber of length $l$, we can write the following input-output connection

$$\hat{A}_o(\tau) = \exp\left(i\hat{\theta}(\tau)\right)\exp\left(i\hat{\phi}(\tau)\right)\hat{A}_i(\tau), \tag{4.30}$$

where the self-phase modulation operator is

$$\hat{\phi}(\tau) = l\int_0^{\infty} d\tau'\ h(\tau')\hat{I}(\tau-\tau'), \tag{4.31}$$

and the Raman phase noise operator is

$$\hat{\theta}(\tau) = \int_0^l dz\, \hat{m}(z,\tau). \tag{4.32}$$

The relative order of $\exp(i\hat{\phi})$ and $\hat{A}_i$ is important in (4.30), but the noise exponential, which commutes with the field factors, can be inserted anywhere.

### 4.2.1 Resonance-Fluorescence

Consider a piece of fiber excited with a monochromatic laser field. Due to the various transitions taking place in this medium, a resonance-fluorescence spectrum for the optical field is obtained at the output of the waveguide. In this paragraph, we show that Raman noise modifies qualitatively this spectrum. Consider a coherent input state $|in\rangle$ corresponding to a monochromatic pump at the carrier frequency. One then has

$$\hat{A}_i(\tau)\,|in\rangle = \sqrt{I_p}\,|in\rangle\,, \tag{4.33}$$

where the constant $I_p$ is the photon flux. The solution (4.30) indicates that the field autocorrelation function for this input state has the form

$$\left\langle \hat{A}_o^\dagger(0)\hat{A}_o(\tau)\right\rangle = I_p \left\langle e^{-i\hat{\theta}(0)}e^{i\hat{\theta}(\tau)}\right\rangle \left\langle e^{-i\hat{\phi}(0)}e^{i\hat{\phi}(\tau)}\right\rangle. \tag{4.34}$$

The two expectation values can be evaluated for any response function. Recall from (4.14) that $e^{-i\hat{\phi}(0)}e^{i\hat{\phi}(\tau)} = e^{-i\hat{\phi}(0)+i\hat{\phi}(\tau)}$. By using the normal ordering formula (C.1) with $g(s) = il\{h(s) - h(s-\tau)\}$, we find

$$\left\langle e^{-i\hat{\phi}(0)}e^{i\hat{\phi}(\tau)}\right\rangle = \exp\left(I_p \int ds\, \{e^{g(s)} - 1\}\right). \tag{4.35}$$

On the other hand, $< e^{-i\hat{\theta}(0)}e^{i\hat{\theta}(\tau)} >= e^{i\frac{1}{2}\alpha} < e^{-i\hat{\theta}(0)+i\hat{\theta}(\tau)} >$, where this time $\alpha = h_R(\tau) - h_R(-\tau)$. The expectation value of the last exponential is computed from the thermal distribution (4.13) using the identity $< \exp(X) >= \exp(\frac{1}{2} < X^2 >)$ for $X$ with a gaussian statistics and with a vanishing average. We finally find the following

contribution to the autocorrelation function from the noise source:

$$\left\langle e^{-i\hat{\theta}(0)} e^{i\hat{\theta}(\tau)} \right\rangle = e^{-i\frac{l}{2}\alpha} e^{-lJ(\tau)}, \tag{4.36}$$

where

$$J(\tau) = \int_{-\infty}^{\infty} \frac{d\omega}{\pi} \bar{h}_R''(\omega) \sin^2(\omega\tau/2) \coth(\hbar\omega/2kT). \tag{4.37}$$

The autocorrelation function can be Fourier transformed to give the spectrum of the radiation leaving the medium[82]. Figure 4-3 displays normalized output power spectra of a medium with a single resonance $\Omega$ and with a damping coefficient $\Gamma$. We assume that all the nonlinearity is of molecular origin. The resulting response function is[78]

$$h(\tau) = \frac{\kappa\Omega^2}{\sqrt{\Omega^2 - \Gamma^2/4}} u(\tau) e^{-\frac{\Gamma}{2}\tau} \sin(\sqrt{\Omega^2 - \Gamma^2/4}\tau), \tag{4.38}$$

where $u(\tau)$ is the step function. The frequency on Fig. 4-3 is measured relative to the carrier, and is normalized to the resonance. The dashed lines were plotted after removing the Raman noise source. All plots use the same pump intensity. Defining $x = K\Omega l/v_g$ and $\gamma = \Gamma/\Omega$ to measure the propagation distance and the width of the resonance respectively, we have: (a) $x = 0.002$, $\gamma = 0.4$, $kT = 0.5\hbar\Omega$, (b) $x = 0.002$, $\gamma = 0.4$, $kT = 5\hbar\Omega$, (c) $x = 0.1$, $\gamma = 0.4$, $kT = 0.5\hbar\Omega$, (d) $x = 0.1$, $\gamma = 0.15$, $kT = 0.5\hbar\Omega$. The spectrum near the pump was removed. For short propagation distances, one can identify in these plots the contributions from individual low order Feynman diagrams (Fig.4-4). Expanding (4.35) and (4.36) to lowest order in $l$, we find that the noise expectation value grows linearly with $l$ whereas self-phase modulation contributes only to second order

$$\begin{aligned}
\left\langle e^{-i\hat{\phi}(0)} e^{i\hat{\phi}(\tau)} \right\rangle &= 1 + il \int ds \{h(s) - h(s-\tau)\} + O(l^2) = 1 + O(l^2), \\
\left\langle e^{-i\hat{\theta}(0)} e^{i\hat{\theta}(\tau)} \right\rangle &= 1 - l\left(J(\tau) + i\frac{\alpha(\tau)}{2}\right) + O(l^2).
\end{aligned}$$

The short distance output spectrum is then dominated by Raman noise. The corre-

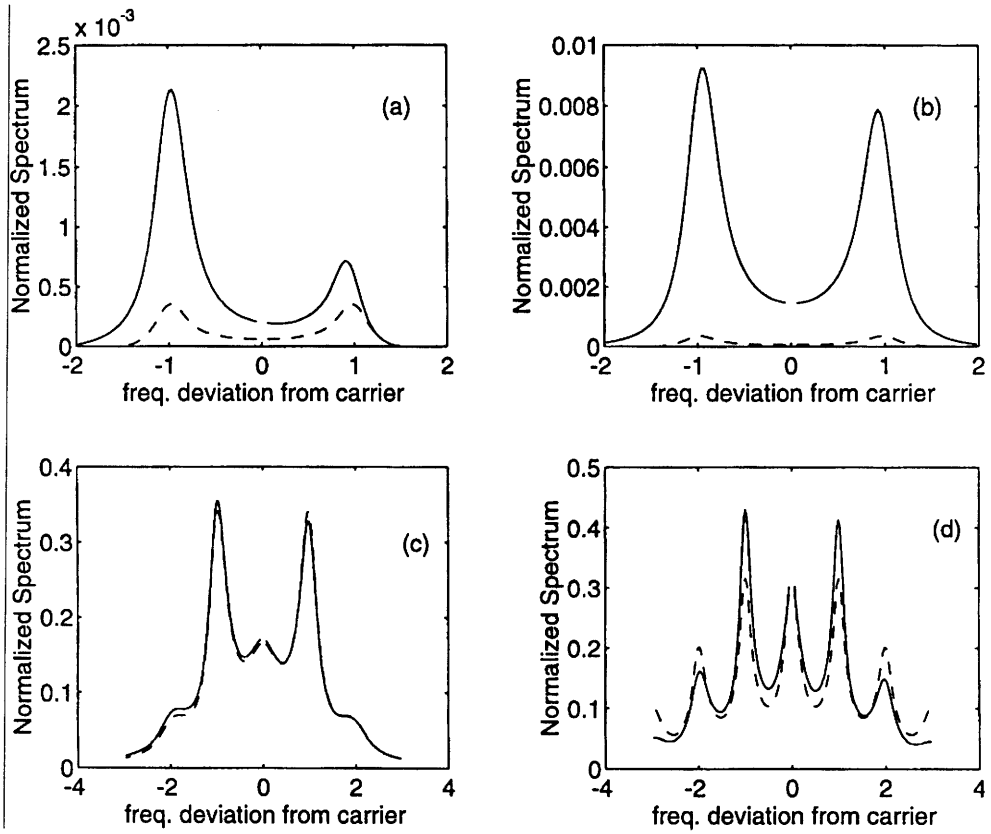


Figure 4-3: Resonance-fluorescence spectra of a single resonance fiber.

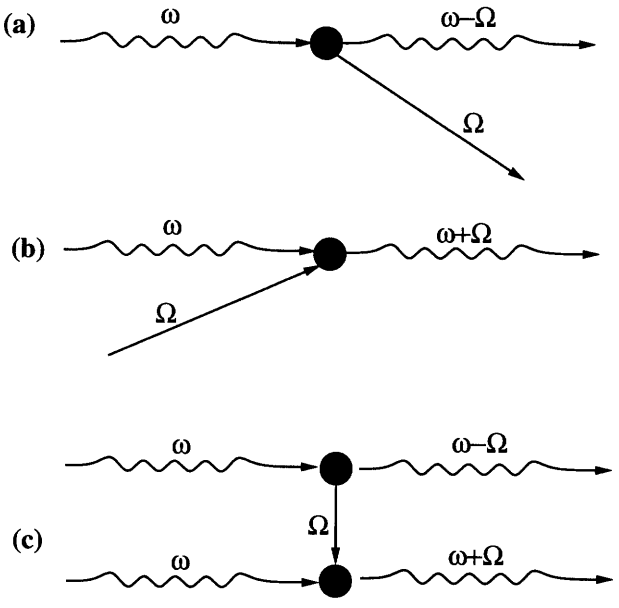


Figure 4-4: Low order Feynman diagrams.

sponding processes are shown on Fig.4-4(a)(Stokes) and Fig.4-4(b)(anti-Stokes). At low temperatures, such that $kT < \hbar\Omega$, the process of Fig.4-4(b), in which a photon gains a quantum of energy from the waveguide, is discouraged due to the absence of thermal medium excitations. In this case, most photons scattered from the pump end up with a lower frequency. As Fig.4-3(b) shows, partial symmetry of the spectrum is restored at higher temperatures. Note that the spectra computed without the Raman noise factor (dashed lines) are symmetric. This is readily understood for short propagation distances since in this case the lowest order Feynman diagram contributing to spectral broadening is shown on Fig. 4-4(c). Clearly this process, in which the medium participates only as the mediator of the nonlinear wave mixing, produces as many photons on the Stokes and anti-Stokes sides. The short distance output spectrum is then qualitatively different when the noise of the medium is neglected. This provides a clear experimental test for our model. The plots of Fig.4-3(c) and Fig.4-3(d) show spectra at longer propagation distances, where the contribution of individual Feynman diagrams can no longer be distinguished. The growth of secondary Stokes and anti-Stokes waves is obvious and is enhanced by a sharper medium resonance. The medium noise is less important in that regime.

### 4.2.2 Mean Field and Discretized-Time Model

As we shall see in Section 4.3, the above solution becomes singular when the response function $h(\tau)$ is taken as instantaneous. The problem resides in the absence of a high frequency cut-off when $D$ is set to zero. In this case, the fluctuations of the electromagnetic modes with arbitrarily high frequencies couple back into the frequency window of the pulse due to the Kerr nonlinearity. These white fluctuations lead to diverging expressions for physical quantities[70]. This situation is, of course, unphysical and reflects the fact that we idealized the nonlinear processes in the fiber as being instantaneous. As we discussed however, the nonlinearity cannot respond infinitely rapidly to the fluctuations of the field. As a result, it is insensitive to its high frequency zero-point noise. Hence, the response-time of the nonlinearity provides a new frequency cut-off which regularizes the theory. Before the development of our model,

an alternate theory based on the discretization of the time axis was introduced in [71, 72, 73]. In this model, the duration of the time intervals introduces a frequency cut-off which removes the divergences of the instantaneous theory. This theory is also self-consistent in the sense that the commutators of the field are preserved. This approach has the advantage of leading to simpler expressions for physical quantities. It is however an approximate model, and its domain of validity must be clarified. This is in part the purpose on the next two paragraphs and of Section 4.3.

In this paragraph, we evaluate the expectation value of the field at zero dispersion. We assume that the fiber is excited by a coherent pulse

$$\hat{A}_i(\tau)\,|in\rangle = \alpha(\tau)\,|in\rangle\,. \tag{4.39}$$

Using the thermal correlators (4.13), the solution (4.30) and the above property, we find

$$\left\langle \hat{A}_o(\tau)\right\rangle = e^{-\frac{\kappa l}{4}M(0)} \exp\left(\int_0^\infty d\tau' \left\{e^{ilh(\tau')} - 1\right\} |\alpha(\tau-\tau')|^2\right) \alpha(\tau). \tag{4.40}$$

In this expression, we defined:

$$\begin{aligned} \kappa l M(\tau-\tau') &= \left\langle \hat{\theta}(\tau)\hat{\theta}(\tau')\right\rangle + \left\langle \hat{\theta}(\tau')\hat{\theta}(\tau)\right\rangle \\ &= l\int_{-\infty}^{\infty} \frac{d\omega}{\pi} \cos(\omega(\tau-\tau')) \coth\left(\frac{\hbar\omega}{2kT}\right) \bar{h}_R''(\omega), \end{aligned} \tag{4.41}$$

so that we have

$$\left\langle \exp(i\hat{\theta}(\tau))\right\rangle = \exp\left(-\frac{1}{2}\left\langle \hat{\theta}^2(\tau)\right\rangle\right) = \exp(-\frac{\kappa l}{4}M(0)). \tag{4.42}$$

Hence we see that the only effect of the Raman phase noise on the mean field is an overall damping. The function $M(\tau)$ for fused silica at room temperature is displayed on Fig. 4-5. From this plot, we find a characteristic Raman damping length

$$l_d \equiv \frac{1}{\kappa M(0)} \simeq 10^5 km, \tag{4.43}$$

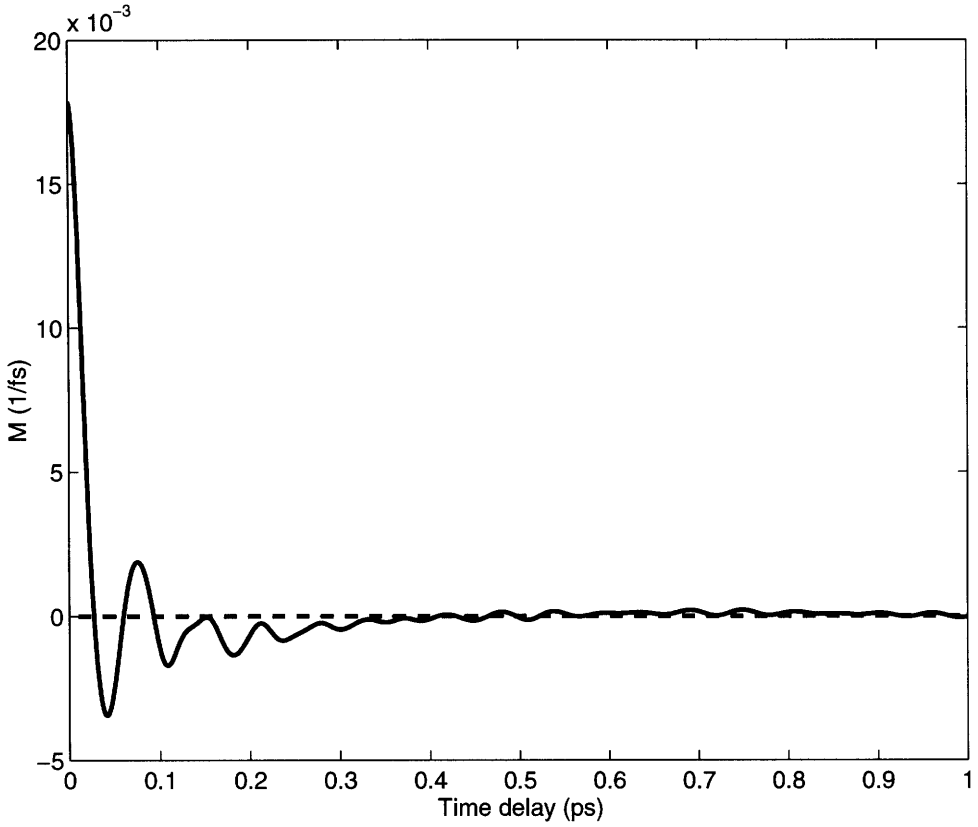


Figure 4-5: Noise function $M(\tau)$ for fused silica at room temperature.

which is very large. For all practical purpose therefore, Raman damping of the mean field is negligible. The other factor in (4.40) was computed using the normal ordering formula (C.1), with $g(s) = ilh(s)$.

As for the above continuous-time model, the discretized-time theory allows to evaluate the output mean field in closed-form. We replace the envelope by a sum of variables defined on each time interval[71, 72, 73]

$$\hat{A}(z,\tau) = \frac{1}{\sqrt{\Delta\tau}}\hat{a}_n(z) \quad \text{for } \tau \text{ between } n\Delta\tau \text{ and } (n+1)\Delta\tau, \tag{4.44}$$

where $[\hat{a}_n, \hat{a}_m] = 0$ and $[\hat{a}_n, \hat{a}_m^\dagger] = \delta_{n,m}$. Introducing this expression in (4.4), with $h(\tau) = \kappa\delta(\tau)$ and $\hat{m} = 0$, one finds, for each time slot, operator

$$\frac{d\hat{a}_n}{dz} = i\frac{\kappa}{\Delta\tau}\hat{a}_n^\dagger\hat{a}_n^2. \tag{4.45}$$

Each of these $n$ decoupled nonlinear equations can again be solved:

$$\hat{a}_n(l) = \exp\left(i\frac{\kappa l}{\Delta\tau}\hat{a}_n^\dagger(0)\hat{a}_n(0)\right)\hat{a}_n(0). \tag{4.46}$$

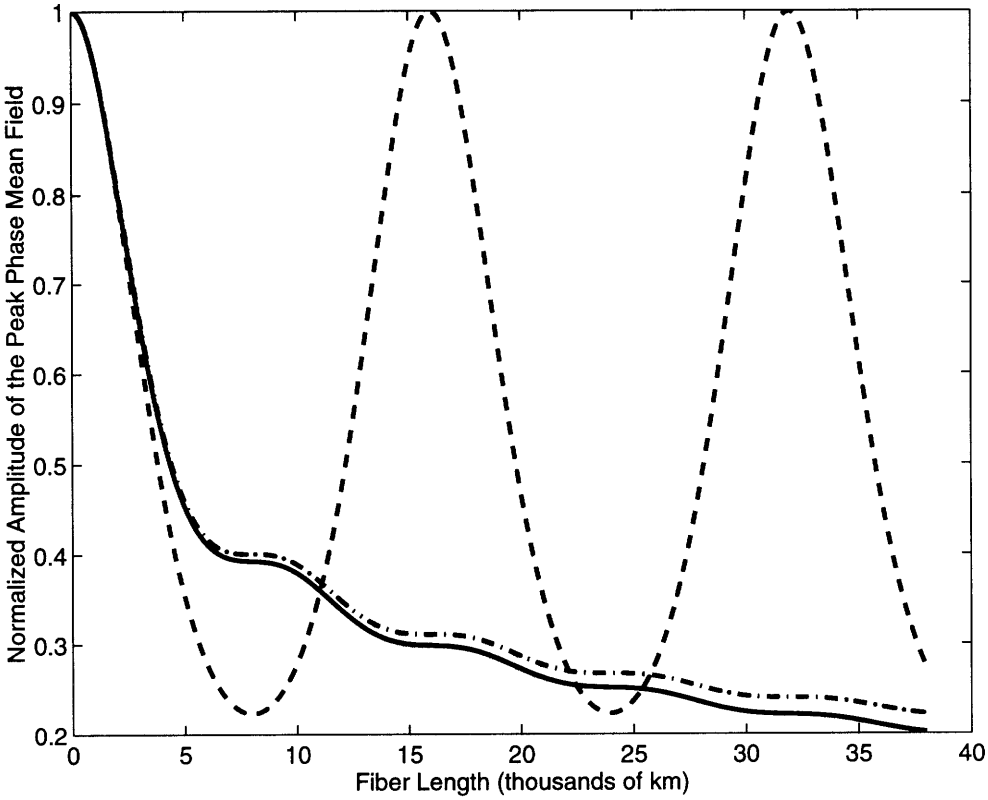


Figure 4-6: Mean field. Solid line=continuous-time model, dashed line=discretized time model, dash-dotted line=continuous-time model without Raman noise.

The coherent state expectation value of the field in the discretized theory is evaluated using (C.2)

$$< \hat{A}_o(\tau) >= \exp\left(\left\{\exp(i\frac{\kappa l}{\Delta\tau}) - 1\right\}\Delta\tau|\alpha(\tau)|^2\right)\alpha(\tau), \tag{4.47}$$

where $\alpha(\tau) = \alpha_n/\sqrt{\Delta\tau}$ for $\tau$ between $n\Delta\tau$ and $(n+1)\Delta\tau$, and $\alpha_n$ is the amplitude of the coherent state of $\hat{a}_n$.

Differences between (4.40) and (4.47) are immediately apparent. First, the discretized-time formula neglects any Raman damping. Second the discretized expression exhibits a spatial periodicity with a period $l = 2\pi\Delta\tau/\kappa$. No such periodic behavior occurs in the continuous-time model. Figure 4-6 compares the magnitude of the mean field at the center of the pulse, normalized to its input value for both formulae. The solid and dashed curves were obtained from the continuous- and discretized-time formulae respectively. A gaussian pulse with a peak power of $75\mu W$ was assumed, and the Raman noise damping was computed at room temperature. For modest fiber lengths, both expressions predict the same departure from the constant classical value.

This was achieved by a proper choice of $\Delta\tau$ in (4.47) which we shall discuss further in Section 4.3. As the fiber length increases, the predictions of the two theories differ, with the discretized-time formula displaying revivals and the continuous-time formula leading to an irreversible decay. The irreversibility in the latter case is not due to Raman noise, but to the infinite number of field modes. This is made apparent on Fig. 4-6 where the dash-dotted line, which was obtained from the continuous-time theory without the Raman noise factor, displays the same irreversibility.

### 4.2.3 Sagnac Photocurrent Fluctuations

The predictions of the continuous- and discretized-time theories for the quantum noise reduction achievable with a Sagnac squeezer at zero dispersion can also be compared. We return to expressions (3.5) and (3.6), which provide the key to the squeezing formula (3.7) for the Sagnac squeezer. The expectation values $F_1$ and $F_2$ are first evaluated using (4.30), which gives the output field of arms 1 or 2 in the continuous-time theory. The input field for both fibers is assumed to obey (4.39). The calculations are straightforward but lengthy and are outlined in Appendix D. Here we simply give the final result

$$\begin{aligned} F_1 &= 2e^{-\kappa l M(0)} \int d\tau_1 d\tau_2 |\alpha(\tau_1)\alpha(\tau_2)|^2 e^{-2n_0 + K_{cc}(\tau_1,\tau_2)} \\ &\times \sinh\left(\kappa l M(\tau_1 - \tau_2) + K_{ss}(\tau_1,\tau_2)\right), \\ F_2 &= 2e^{-\frac{\kappa l}{2} M(0)} \int d\tau |\alpha(\tau)|^2 e^{-2n_0 + K_c(\tau)} K_s(\tau). \end{aligned} \tag{4.48}$$

The function $M(\tau)$ was defined by (4.41), and the $K$-integrals are

$$K_{s\ldots s}(\tau_1, \ldots, \tau_n) = 2 \int d\tau' |\alpha(\tau')|^2 \sin\left(lh(\tau_1 - \tau')\right) \ldots \sin\left(lh(\tau_n - \tau')\right), \tag{4.49}$$

and a similar definition for $K_{c\ldots c}$ with cosine functions. The integral $M(\tau)$ gives again the contribution from the noise exponential in (4.30). This function does not vanish, even when $T = 0$, due to the zero point fluctuations of the heat bath. By setting $M = 0$, one can evaluate the effect of the Raman noise on the squeezing performance

of the setup. Note from (4.41) that the Fourier transform of $M(\tau)$ is proportional to $\coth(\hbar\omega/2kT)\bar{h}_R''(\omega)$ and not to $\bar{h}_R''(\omega)$ itself. The hyperbolic prefactor, which is one and therefore irrelevant at high frequencies, enhances the contribution to $M$ from the thermally excited low frequency Raman oscillators. The dashed curve on Figure 4-1 shows the effect of the hyperbolic prefactor on the Raman gain coefficient.

Before using the above expressions for $F_1$ and $F_2$ in $R_{Sagnac}$ for specific input pulses, we turn to the discretized-time theory. Using (4.46) instead of (4.30), we find

$$\begin{aligned} F_1 &= \Delta\tau \int d\tau |\alpha(\tau)|^4 \left[1 - \exp\left(-4\Delta\tau|\alpha(\tau)|^2 \sin^2(\frac{\kappa}{\Delta\tau}l)\right)\right], \\ F_2 &= 4\sin(\frac{\kappa}{\Delta\tau}l)\Delta\tau \int d\tau |\alpha(\tau)|^4 \exp\left(-4\Delta\tau|\alpha(\tau)|^2 \sin^2(\frac{\kappa}{2\Delta\tau}l)\right). \end{aligned} \quad (4.50)$$

One can show that (4.48) reduces to (4.50) when (*i*) $M$ is set to zero, (*ii*) the integral over $\tau_2$ in $F_1$ is approximated by $\Delta\tau$ times the integrand at $\tau_2 = \tau_1$, (*iii*) the response function is taken as:

$$h(\tau) = \begin{cases} \frac{\kappa}{\Delta\tau} & \text{if } 0 < \tau < \Delta\tau \\ 0 & \text{otherwise} \end{cases} \quad (4.51)$$

and (*iv*) the intensity of the pulse is assumed constant over a period $\Delta\tau$.

Consider a gaussian input pulse (Appendix C)

$$\alpha(\tau) = \sqrt{\frac{n_0}{\tau_p}} \exp\left(-\frac{\pi\tau^2}{2\tau_p^2}\right) \quad (4.52)$$

with $\tau_p = 20ps$ and $n_0 = 2.8\times10^9$. The parameter $\tau_p$ is the pulse time scale introduced in the next section (see (4.57)). In the case of a gaussian pulse, it is related to the FWHM pulse duration by

$$T_{FWMH} = 2\sqrt{\frac{2}{\pi}}\tau_p \simeq 0.9394\tau_p. \quad (4.53)$$

The values introduced above for $n_0$ and $\tau_p$ are typical of the recent experiments at MIT [32]. Since the pulses vary little over the characteristic time of $h$, the detailed form of this function is not critical in the evaluation of the $K$-integrals in the continuous-

time theory. The most important feature of these integrals is the saturation of the integrands due to the circular functions. This effect leads to a degradation of squeezing when $lh$ becomes large over a substantial region of the domain of integration. As discussed in Section 4.3, the electronic response time determines the fiber length where this effect occurs. To simplify the numerical analysis, we therefore evaluate the $K$-integrals with the response function:

$$h(\tau) = \frac{\kappa}{\tau_e} e^{-\tau/\tau_e}, \tag{4.54}$$

where $\tau_e = 0.5fs$.

Figure 4-7 and 4-8 show $R_{Sagnac}$ as a function of fiber length in the arms of the interferometer measured in units of the peak nonlinear phase shift, $\Phi = \kappa l \left|\alpha(0)\right|^2 = \phi(l,0)$ (see (3.30)). The curves obtained from the continuous- (solid lines) and discretized-time (dashed lines) theories are compared at room temperature. The time constant of the discretized model was chosen so that the onset of the quantum regime occurs for the same length of fiber as for in the continuous-time model. Also displayed are the curves from the continuous-time theory without noise source (dash-dotted lines), and the linearized curves with and without noise. A $0.1dB$ departure from these curves occurs roughly at a phase shift of 85, where $l \simeq 1.0km$, in accordance with the results of the next section. When the phase shift increases well beyond the linearized regime, $R_{Sagnac}$ deteriorates and eventually reaches the limiting value of 1. No revival occurs in our continuous theory, even when the Raman noise is neglected. This effect cannot be seen when the response function is idealized by the step function (4.51) and when noise is neglected as in [77]. In this case the continuous-time theory predicts revivals. On the other hand the model with a discretized-time axis clearly produces expressions for $F_1$ and $F_2$ which return to their input value when $l = 2\pi\Delta\tau/\kappa$, as for the mean field. Once again, we see that this periodicity is an artifact of the discretization. Figure 4-7 compares the continuous- and discretized-time curves in the same conditions as in Fig. 4-7 and 4-8, but with $n_0 = 2.8 \times 10^4$. In this case, the discretized theory predicts revivals for small phase

shifts. From figure 4-8, we see that the dashed line and the dash-dotted line overlap beyond the linearized regime. This indicates that the discretized model predicts correctly the low order departure from the linearized approximation. As for the mean field, Raman noise is completely neglected by this theory however. The next Section considers in more details the breakdown of the linearized approximation.

## 4.3 Linearized Regime and Onset of the Quantum Regime

We close this chapter with a discussion of the linearized limit. In paragraph 4.3.2, we obtain a linearized squeezing formula including both the effect of Raman noise and of the finite response time of the Kerr nonlinearity. We will also take advantage of the availability of an exact solution at zero dispersion to find expressions for the first order corrections to the linearized expressions for the cases considered in Section 4.2. The purpose of this calculation is to determine the value of $\Delta\tau$ required for the discretized model to produce quantum corrections identical to those obtained from the continuous-time model.

We first observe that the linearized theory is obtained from the exact field equations by taking the limit of large photon numbers, keeping nonlinear phase shifts of order unity. For simplicity, consider one time interval of the discretized-time model. Separating the field as $A + \hat{a}/\sqrt{\Delta\tau}$, with $A(z,\tau) = \exp(i\phi(z,\tau))\alpha(\tau)$, we have

$$\frac{\partial \hat{a}}{\partial z} = 2i\kappa |A|^2 \hat{a} + i\kappa A^2 \hat{a}^\dagger + 2i\frac{\kappa A}{\sqrt{\Delta\tau}}\hat{a}^\dagger\hat{a} + i\frac{\kappa A^*}{\sqrt{\Delta\tau}}\hat{a}^2 + i\frac{\kappa}{\Delta\tau}\hat{a}^\dagger\hat{a} \tag{4.55}$$

Dividing both sides by $\kappa |\alpha(0)|^2$, we find the equation

$$\frac{\partial \hat{a}}{\partial \Phi} = 2i\hat{a} + ie^{2i\phi}\hat{a}^\dagger + 2ie^{i\phi}\sqrt{\frac{\tau_p}{n_0\Delta\tau}}\hat{a}^\dagger\hat{a} + ie^{-i\phi}\sqrt{\frac{\tau_p}{n_0\Delta\tau}}\hat{a}^2 + i\frac{\tau_p}{n_0\Delta\tau}\hat{a}^\dagger\hat{a}, \tag{4.56}$$

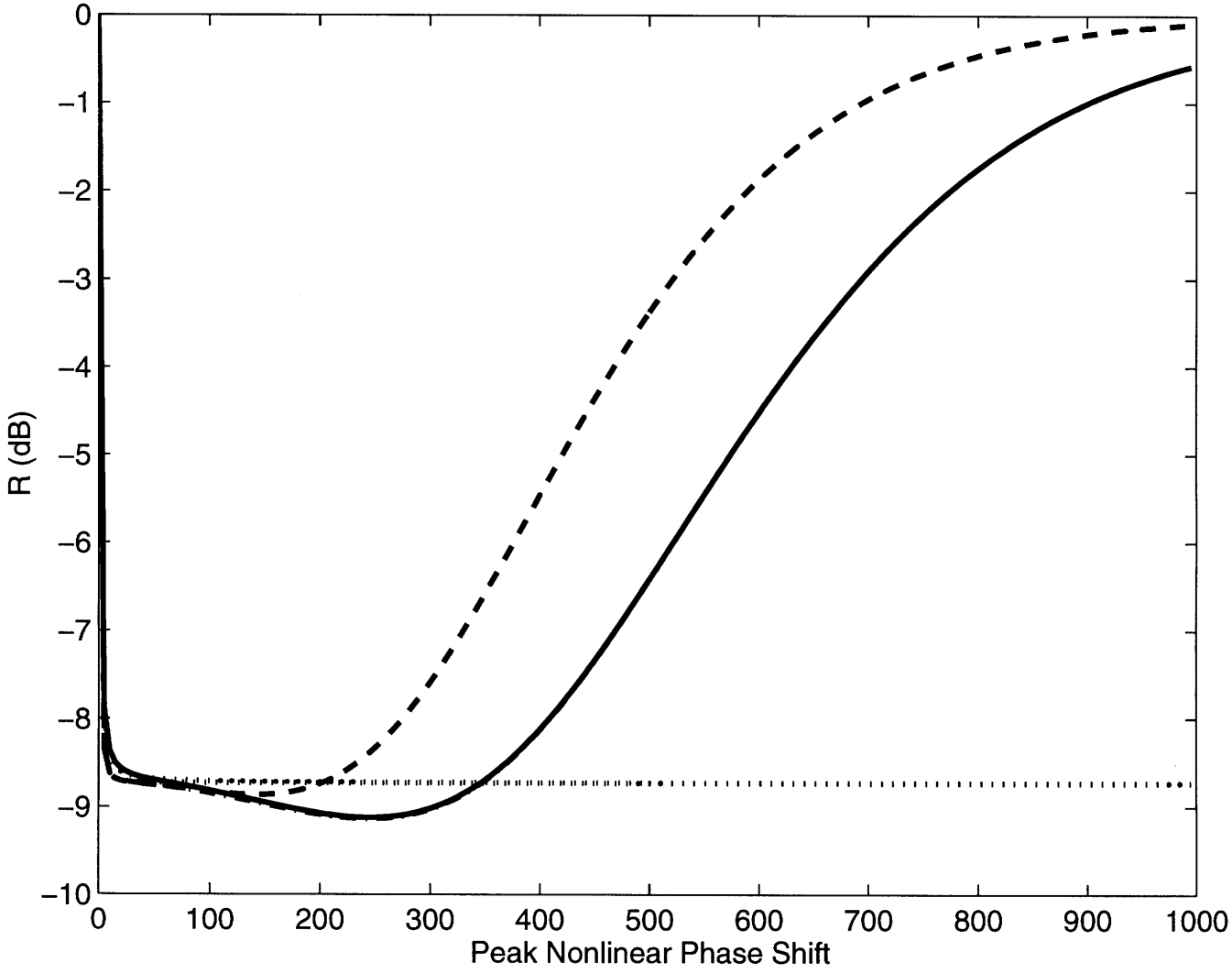


Figure 4-7: Minimum variance of the balanced homodyne photocurrent in a Sagnac squeezer at zero dispersion. The variance is normalized to the vacuum level (see $R_{Sagnac}$ defined in Section 3.1). Continuous-time (solid). Discretized-time (dashed). Continuous-time without Raman noise (dash-dotted). Linearized with and without Raman noise (dotted).

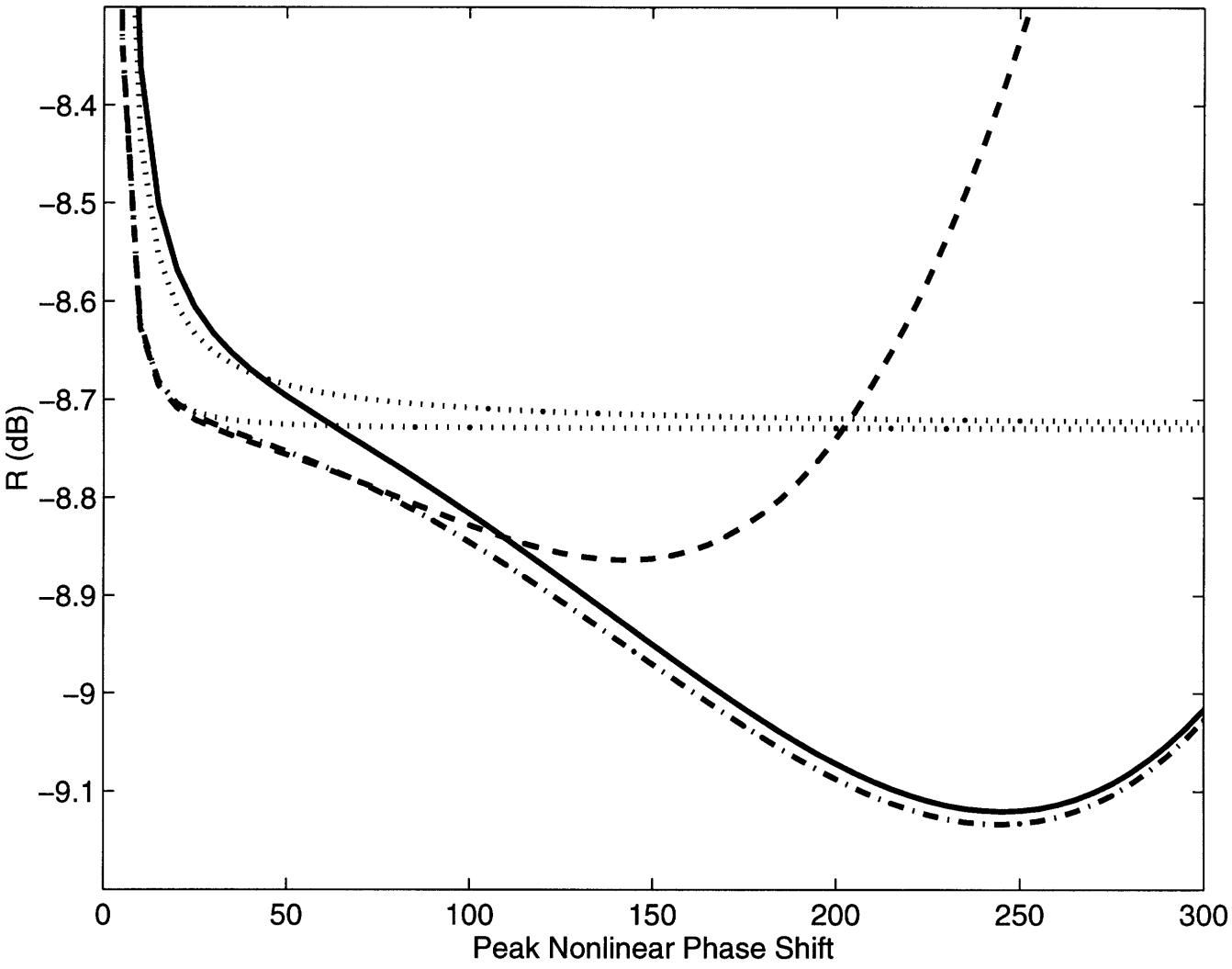


Figure 4-8: Enhancement of the small phase shift region for the previous figure.

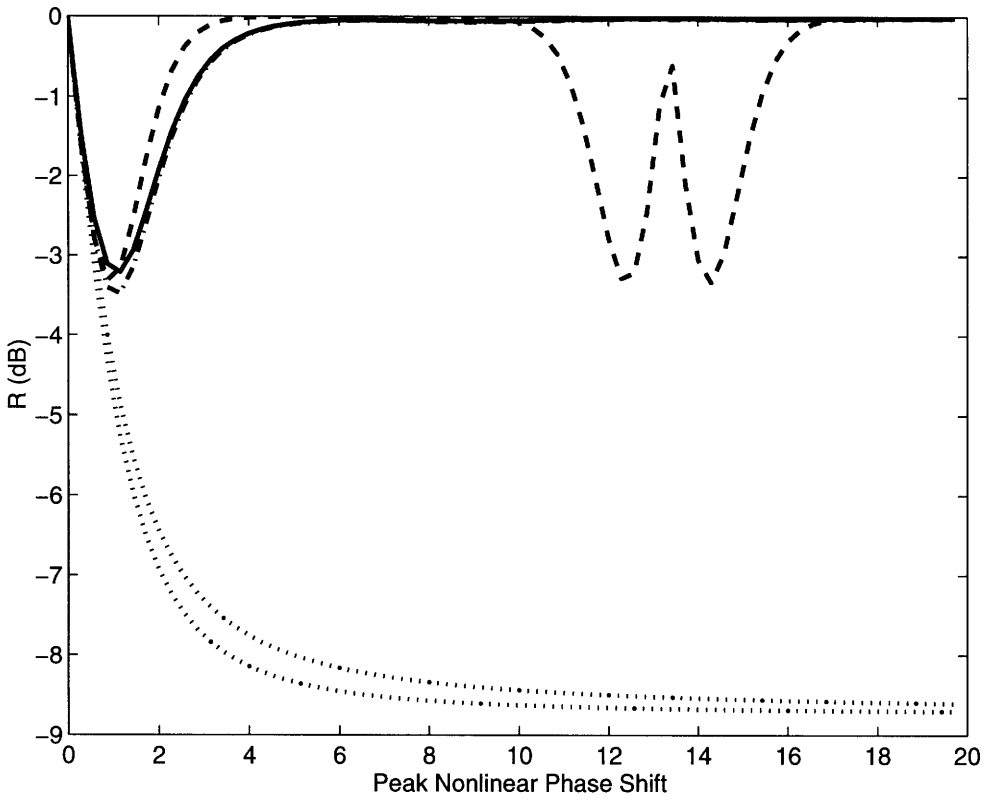


Figure 4-9: $R_{Sagnac}$ for long and weak gaussian pulses at zero-dispersion. The lines have the same meaning as in the previous two figures.

where the pulse time scale, $\tau_p$, is defined by (Appendix C):

$$\tau_p = \frac{n_0}{|\alpha(0)|^2}. \tag{4.57}$$

When $n_0 \Delta\tau/\tau_p$ becomes large, while $\Phi$ stays of order unity, the contribution of the last three terms in (4.56) to the evolution of $\hat{a}$ becomes negligible. Dropping these terms, we recover the linearized equation of Section 3.2.2. The above conditions for the photon number and the phase shift are met in most fiber squeezing experiment. For example, in the MIT fiber squeezer [32], one has $n_0 \simeq 10^9$ and $\Phi \simeq 4$. Our discussion also indicates that quantum corrections to the linearized expressions will appear as a series of terms with increasing inverse power of the photon number.

### 4.3.1 Mean Field

Consider again the self-phase modulation factor in expression (4.40). We replace $l$ by $\Phi$ as the evolution parameter in this expression and we expand the resulting formula

in inverse powers of the photon number. For pulses varying little over the time scale of $h(\tau')$, we have

$$\exp\left(\int d\tau' \left\{e^{ilh(\tau')} - 1\right\} |\alpha(\tau - \tau')|^2\right) = \exp\left(i\kappa l|\alpha(\tau)|^2\right)\left\{1 - \frac{\Phi^2}{2n_0}\frac{|\alpha(\tau)|^2}{|\alpha(0)|^2}\frac{\tau_p}{\tau_q} + O\left(\frac{1}{n_0^2}\right)\right\}, \tag{4.58}$$

where $\tau_p$ is defined by (4.57), and the material quantum time scale, $\tau_q$, is defined by:

$$\frac{1}{\tau_q} \equiv \frac{1}{\kappa^2}\int_0^\infty d\tau'\, h^2(\tau'). \tag{4.59}$$

The overall exponential in (4.58) is the classical nonlinear phase picked up by a pulse in a Kerr medium[54]. Recalling that in the linearized theory, the mean field is given by $A(z,\tau)$, the first term in (4.58) can therefore be identified as the contribution from the linearized theory. The following term of order $1/n_0$ arises from the non-commutativity of the field and is the lowest order correction to the linearized theory. Expression (4.58) indicates that $\tau_q$ determines the length of fiber beyond which substantial quantum effects occur for a given pulse intensity. Indeed, defining the length

$$l_q = \frac{1}{\kappa}\sqrt{\frac{0.2\tau_q\tau_p}{n_0}}, \tag{4.60}$$

the magnitude of the vacuum term at the center of the pulse becomes larger than 0.1 when the fiber is longer than $l_q$. Contrary to the Raman damping length $l_d$, which was power independent, $l_q$ is shorter for intense pulses. The solid curve on Fig.4-10 shows $l_q$ as a function of the peak power for pulses in fused silica fibers. In this figure we assumed $\tau_q = 1.5fs$, corresponding to a material time scale typical of the electronic Kerr effect. This value is more appropriate than the time scale of the much slower Raman oscillators. Indeed, consider a medium where the Kerr effect arises from the dynamics of fast and slow material degrees of freedom, as in fused silica. Assume also

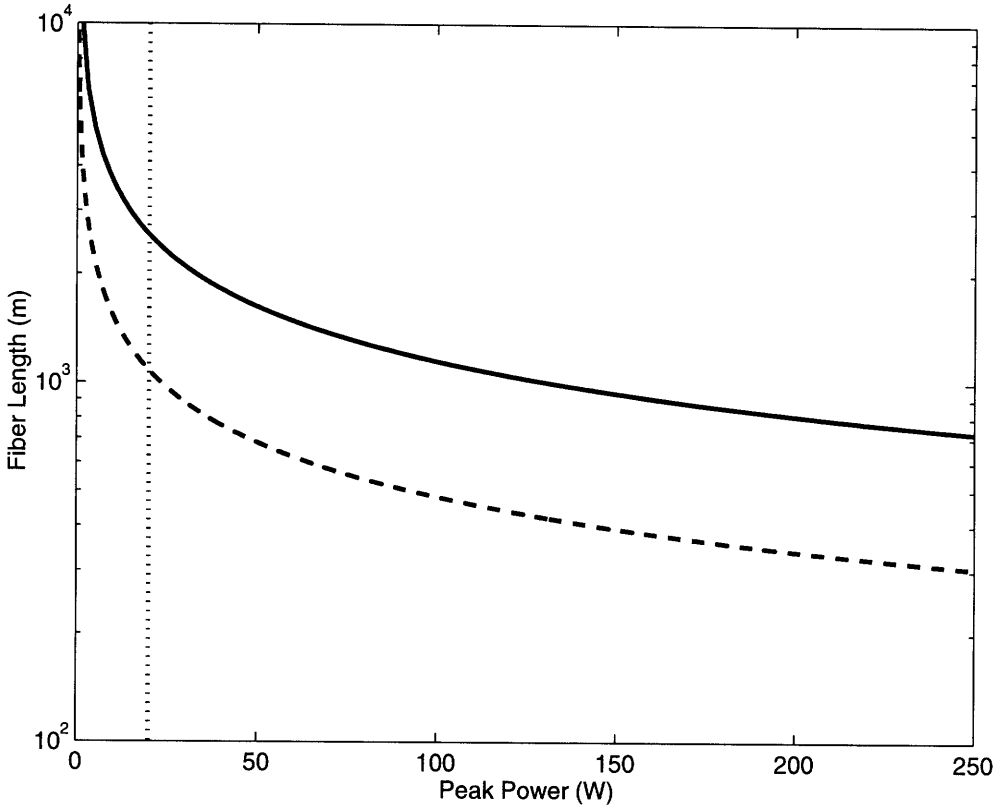


Figure 4-10: Length scales for the breakdown of the linearized approximation at zero dispersion. The solid and dashed lines show the length scales beyond which corrections to the linearized mean field and noise reduction ratio become important respectively.

that the response function takes the simplified form:

$$h(\tau) = u(\tau)\left\{\frac{\kappa_e}{\tau_e}\exp(-\tau/\tau_e) + \frac{\kappa_R}{\tau_R}\exp(-\tau/\tau_R)\right\}, \tag{4.61}$$

where $u(\tau)$ is the step function and where $\kappa_e$ and $\kappa_R$ are the contributions to the Kerr coefficient from the fast and slow oscillators ($\kappa_e + \kappa_R = \kappa$). Typically [125] $\kappa_e = 0.8\kappa$, $\kappa_R = 0.2\kappa$, $\tau_e = 0.5fs$ and $\tau_R = 100fs$ for fused silica fibers. Using the above model, one can estimate the material time scale

$$\frac{1}{\tau_q} = \frac{1}{\kappa^2}\left\{\frac{\kappa_e^2}{2\tau_e} + \frac{\kappa_R^2}{2\tau_R} + \frac{\kappa_e\kappa_R}{\tau_e+\tau_R}\right\} \simeq \left(\frac{\kappa_e}{\kappa}\right)^2 \frac{1}{2\tau_e} \simeq \frac{1}{3\tau_e}. \tag{4.62}$$

The above expression suggests the importance of the faster electronic nonlinearity in fixing the length scale for the onset of the quantum effects.

Consider now the discretized expression for the mean field, i.e. equation (4.47). Trading once again the propagation distance with the peak nonlinear phase shift and

expanding this expression in inverse powers of the photon number, we find

$$\left\langle \hat{A}_o(\tau) \right\rangle = e^{i\kappa l|\alpha(\tau)|^2} \left\{ 1 - \frac{\Phi^2}{2n_0} \frac{\tau_p}{\Delta\tau} \frac{|\alpha(\tau)|^2}{|\alpha(0)|^2} + O\left(\frac{1}{n_0^2}\right) \right\} \alpha(\tau), \tag{4.63}$$

Comparing (4.63) with (4.58), we see that $\Delta\tau$ in the discretized theory plays the role of $\tau_q$ in the continuous theory, at least to lowest order in the quantum corrections. One should therefore use[66]

$$\Delta\tau = \kappa^2 \frac{1}{\int_0^\infty d\tau'\, h_e^2(\tau')}. \tag{4.64}$$

### 4.3.2 Photocurrent Fluctuations

Consider now the continuous-time expression for $F_1$ and $F_2$ derived in Section 4.2.4. The linearized expressions for these functions are obtained by expressing $l$ in terms of $\Phi$ and by keeping only terms of order 1 in $F_1/2n_0$ and $F_2/2n_0$

$$\frac{F_1^{lin}}{2n_0} = N\Phi + 2p_6\Phi^2, \tag{4.65}$$

$$\frac{F_2^{lin}}{2n_0} = 2p_4\Phi, \tag{4.66}$$

where the pulse dependent coefficients $N$, $p_4$ and $p_6$ are

$$N = \frac{1}{n_0|\alpha(0)|^2} \int d\tau\, |\alpha(\tau)|^2 \int d\tau' |\alpha(\tau-\tau')|^2 M(\tau'), \tag{4.67}$$

$$p_n = \frac{1}{n_0|\alpha(0)|^{n-2}} \int d\tau |\alpha(\tau)|^2 \left[ \int d\tau' |\alpha(\tau-\tau')|^2 \frac{h(\tau')}{\kappa} \right]^{n/2-1}. \tag{4.68}$$

From formula (3.7), we therefore have the quantum noise reduction formula in the linearized regime [51, 66]

$$R_{Sagnac}^{lin} = 1 + (N\Phi + 2p_6\Phi^2) - \sqrt{(N\Phi + 2p_6\Phi^2)^2 + (2p_4\Phi)^2}. \tag{4.69}$$

As we indicated in Section 3.1, $R_{Sagnac}$ and $R_{SPM}$ have the same linearized limit. The above expression should therefore be compared with (3.40) which was derived for an

instantaneous Kerr nonlinearity. In fact, assuming that the pulse varies little over the characteristic time of $M$ and $h$, the convolution integrals in the expressions for $p_n$ and $N$ can be simplified by letting $|\alpha(\tau - \tau')|^2 \simeq |\alpha(\tau)|^2$. In this case, $p_n$ reduces to expression (3.39) derived previously, and $N = p_4\eta$ with

$$\eta = \int d\tau M(\tau). \tag{4.70}$$

We therefore see that even in the limit of long pulses, the theory presented in this chapter leads to a slightly different squeezing formula than (3.40). Using (4.41), we find an explicit expression for $\eta$

$$\eta = \frac{4k_B T}{\hbar}\left(\frac{\kappa_R}{\kappa}\right) T_R, \tag{4.71}$$

where we defined the Raman response time by[78]:

$$T_R = \frac{1}{\kappa_R} \lim_{\omega \to 0} \frac{\tilde{h}_R''(\omega)}{\omega}, \tag{4.72}$$

with $\kappa_R \simeq 0.189\kappa$ being the contribution to the Kerr coefficient from the Raman oscillators. The low frequency fit of $g(\nu)$ in [81] gives $T_R = 4fs$, so that $\eta = 0.12$ at room temperature. Following a similar approximation procedure for the discretized-time theory, we recover the above formula for the function $R^{lin}_{Sagnac}$, but with $\eta = 0$. This function is displayed on Fig. 4-11 for gaussian and square pulses. It is clear from this plot that the Raman noise in silica does not affect significantly the squeezing level. This conclusion is consistent with previous work on Raman noise in the soliton regime [78, 85, 86]. As can be seen from (4.71), this is due to the small value of $T_R$ and to the small fraction of the Kerr nonlinearity arising from these degrees of freedom. We note here that the Raman response time defined by (4.72) is much shorter than the characteristic time of the Raman response function which, from Fig.4-2 is rather on the order of 100 fs. This difference, which is due to the very small slope of the Raman gain at $\nu = 0$, indicates that $T_R$ is not a good measure of the time scale involved in the dynamics of the Raman oscillators. Due to our lack of information on the electronic

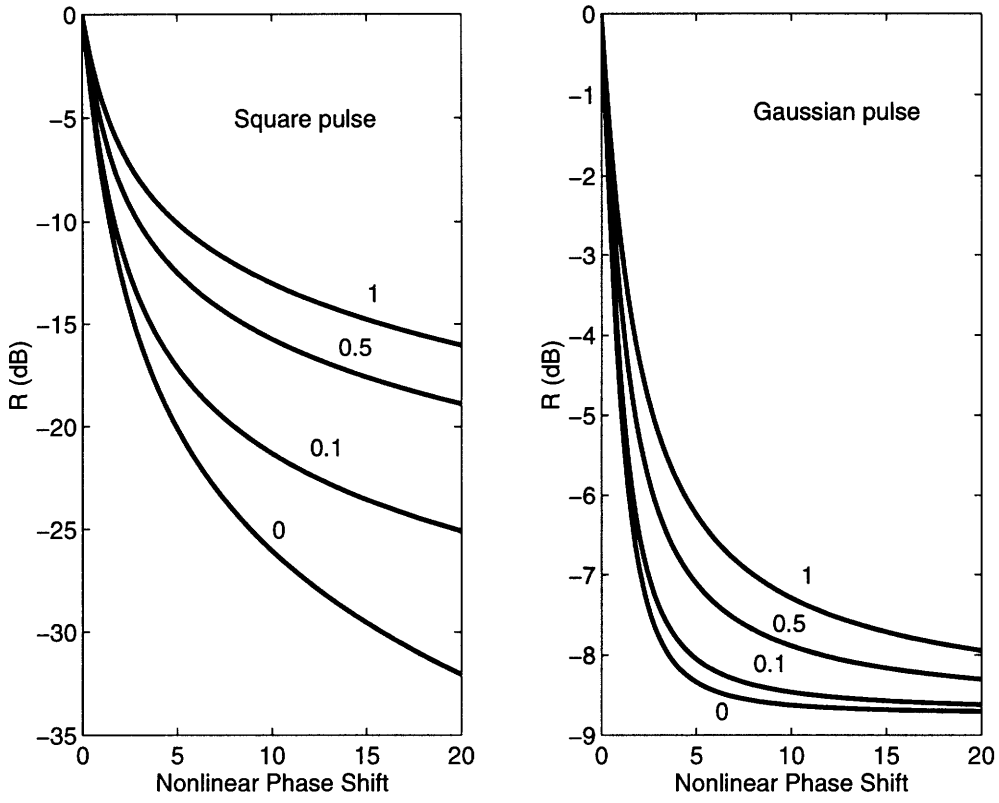


Figure 4-11: Linearized SPM squeezing in the presence of Raman noise for square and gaussian noise.

response function, we did not include the contribution from two-photon absorption noise in $\eta$. It is however expected to be small as well. Indeed, for the exponential response function (4.24), the response time

$$T_e \equiv \frac{1}{\kappa_e} \lim_{\omega \to 0} \frac{\tilde{h}_e''(\omega)}{\omega}, \tag{4.73}$$

equals $\tau_e \simeq 0.5fs$. The electronic contribution to $\eta$ would therefore be

$$\eta_e = \frac{4k_B T}{\hbar} \left( \frac{\kappa_e}{\kappa} \right) T_e, \tag{4.74}$$

which is about half the Raman contribution.

It is interesting to note that the Raman noise does not modify the asymptotic squeezing limit found in Section 3.1.1. This result indicates that the Raman phase noise builds up at a slower rate than the noise reduction by squeezing. The linearized theory therefore indicates that one can overcome the loss of squeezing due to Raman noise by using a longer fiber. Eventually, the linearized formula is no longer a good

approximation and a slightly higher noise floor due to the Raman source is found, as can be seen on Fig. 4-7 and Fig. 4-9.

Consider now the linearized formula for pulses shorter than $1ps$. The discretized model is inadequate to describe such pulses. We therefore use the continuous-time theory where the convolutions in $N$ and $p_n$ require a reasonable model for the response function of silica. As long as the pulses are much longer than the electronic response time, one can approximate the corresponding nonlinearity as instantaneous[84]. We will therefore use in the linearized theory:

$$\frac{h(\tau)}{\kappa} = 0.8\delta(\tau) + \frac{2u(\tau)}{\pi\kappa}\int_0^\infty d\omega \bar{h}_R''(\omega)\sin(\omega\tau), \tag{4.75}$$

where $u(\tau)$ is again the step function. Inserting $h$ in the expressions for $N$, we obtain the plot of Fig 4-12. This curve shows the noise parameter $\eta = N/p_4$ for gaussian pulses, as a function of the pulse duration. As can be seen, $\eta$ doubles for pulses with a duration of the order of $20fs$ and quickly decreases for shorter pulses. Referring to Fig.4-11, one can therefore see that the effect of the Raman noise on squeezing is never very important in silica. Figure 4-13 is a plot of the limiting value, $1 - p_4^2/p_6$, for gaussian pulses as a function of the pulse width. This figure indicates that when the noise is neglected, the dynamics of the Raman oscillators enhances squeezing for pulses with a duration of the order of $20fs$. For even shorter pulses, the Raman nonlinearity becomes ineffective in (4.2) because $h_R$, which vanishes at $\tau = 0$ cannot rise fast enough. A more thorough analysis of squeezing with short pulses should however include the effect of third order dispersion and self-steepening which were neglected in our discussion, and becomes important for pulses shorter than $100fs$[54].

The pulses used in [32] had a peak power of roughly $20W$, corresponding to $l_q \simeq 2.6km$. This small value indicates that squeezing experiments with more intense pulses could well be affected by vacuum terms. Let us evaluate the correction to $R^{lin}_{Sagnac}$ from these terms. As for the mean field, the overall Raman damping does not affect $R_{Sagnac}$ for fibers shorter then a few thousand kilometers. We therefore neglect

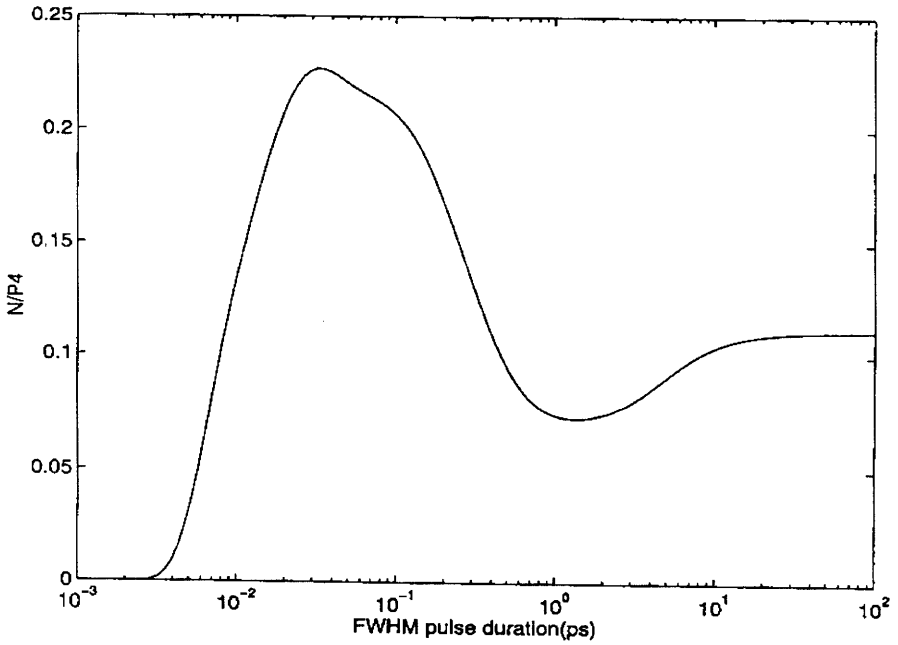


Figure 4-12: Raman noise parameter of the linearized theory for subpicosecond gaussian pulses in fused silica.

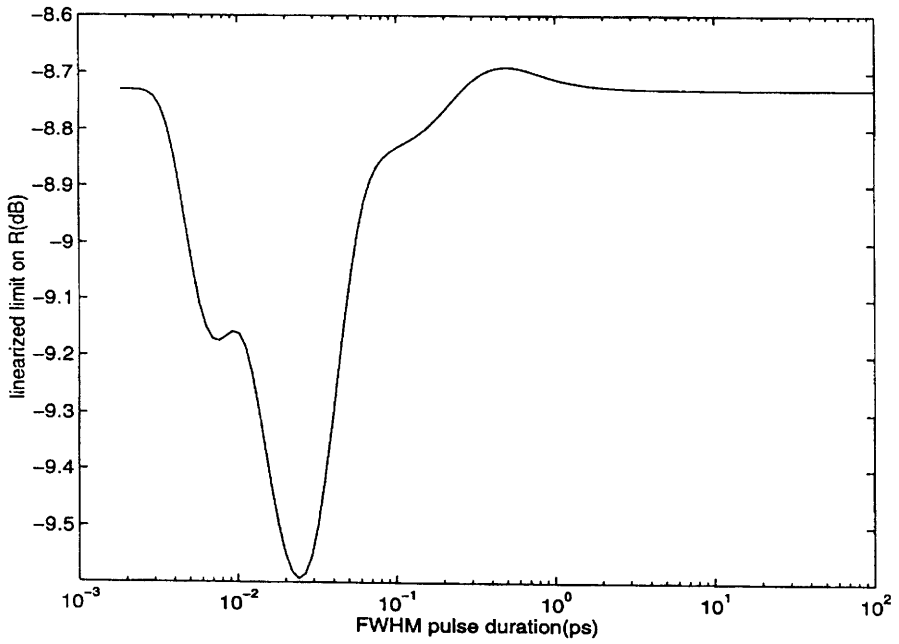


Figure 4-13: Lower bound on squeezing given by the linearized theory for subpicosecond gaussian pulses in fused silica.

this effect. The small value of $\eta$ for fused silica also makes this parameter irrelevant to the determination of the fiber length where the linearized theory breaks down. Our derivation of $R^{lin}_{Sagnac}$ is the first step of a systematic expansion of $R_{Sagnac}$ in inverse powers of the photon number. Keeping the first two terms in such an expansion for $F_1$ and $F_2$, we have:

$$\frac{F_1}{2n_0} \simeq \frac{F_1^{lin}}{2n_0}\left(1 - \frac{2p_8\Phi^2}{p_6\left|\alpha(0)\right|^2\tau_q}\right), \tag{4.76}$$

$$\frac{F_2}{2n_0} \simeq \frac{F_2^{lin}}{2n_0}\left(1 - \frac{p_6\Phi^2}{p_4\left|\alpha(0)\right|^2\tau_q}\right). \tag{4.77}$$

Note that $p_8 = 0.5$, $16/35$ and $1$ for gaussian, sech and square pulses respectively. Let $\Delta R$ denote the change, in $dB$, from $R^{lin}_{Sagnac}$ due to the vacuum terms. Hence, if $R_{Sagnac} = R^{lin}_{Sagnac}(1+\delta)$ where $\delta$ is a small number, we have $\Delta R = 10\,\delta/\ln 10$. Inserting the corrected expressions for $F_1$ and $F_2$ into the definition of $R_{Sagnac}$, we find $\Delta R = G(\Phi)/\tau_q|\alpha(0)|^2$, where the monotonously increasing function $G(\Phi)$ is:

$$G(\Phi) = -\frac{10}{\ln 10 R_{lin}}\left[\frac{2p_8}{p_6}\frac{F_1^{lin}}{2n_0} - \frac{\frac{2p_8}{p_6}\left(\frac{F_1^{lin}}{2n_0}\right)^2 + \frac{p_6}{p_4}\left(\frac{F_2^{lin}}{2n_0}\right)^2}{\sqrt{\left(\frac{F_1^{lin}}{2n_0}\right)^2 + \left(\frac{F_2^{lin}}{2n_0}\right)^2}}\right]\Phi^2. \tag{4.78}$$

For a fixed nonlinear phase shift, the correction to $R^{lin}_{Sagnac}$ increases with decreasing $|\alpha(0)|^2$. Given $\tau_q$ and a tolerance level for $\Delta R$, the above relation establishes , for a given $\Phi$, the peak photon flux below which the correction to $R^{lin}_{Sagnac}$ exceeds $\Delta R$. The length of fiber corresponding to these values of $\Phi$ and $|\alpha(0)|^2$ can then be found from $\Phi = \kappa l\,|\alpha(0)|^2$. Each point on the dashed curve of Fig.4-10 gives a fiber length and a peak power obtained from the above procedure for gaussian pulses using different nonlinear phase shifts and a $0.1dB$ tolerance level for $\Delta R$. At fixed power, fibers with length above this curve correspond to larger phase shift, to larger values of $|G(\Phi)|$ and, therefore, to larger corrections $\Delta R$.

# Chapter 5

# Quantum Noise of the Fundamental Soliton

Soliton squeezing was briefly discussed in Section 3.3 using the linearized approximation. In the present chapter, we investigate in more detail the domain of validity of this approximation in the soliton regime. To do so, we take advantage of the availability of an exact solution to the quantized nonlinear Schrödinger equation (QNSE) in $1+1$ dimensions. The bound states of this equation were found in the 1960's using Bethe's ansatz [95, 96, 97, 98, 99, 100]. We assume that at the input of the fiber, the field is in a Poisson-Gaussian superposition of Bethe eigenstates. Using the known time dependence for the latter, we follow the quantum noise evolution. Another approach to the study of dispersive squeezing beyond the linearized approximation uses the positive $P$-distribution [58, 59]. Contrary to the analytical treatment presented here, this method is numerical in nature, even for optical solitons. Our discussion extends the work of Lai and Haus [104] who evaluated the mean field in a Poisson-Gaussian superposition of Bethe states but did not consider their noise properties. We show that the phase shift beyond which the linearized approximation does not describe quantum noise properly scales as $n_0^{1/4}$, where $n_0$ is the average photon number of each pulse. The fluctuations of the four soliton operators in Poisson-Gaussian solitons are also considered. We show that these states minimize the uncertainty on these collective operators. It was shown in [60, 64] that this cannot be done with

coherent states.

This chapter is organized as follow. In Section 5.1 we briefly review the quantum theory of soliton propagation in the Schrödinger picture. In Section 5.2, the mean field and the noise correlation functions for Poisson-Gaussian solitons are evaluated. These correlators are key ingredients in the analysis of the following two sections. The calculations are however tedious and their bulk is transfered in appendix. Section 5.3 is devoted to non-linearized squeezing. Finally, Section 5.4 introduces the four soliton noise operators as pairs of conjugate variables. The noise properties of these operators in coherent and in Poisson-Gaussian soliton states are compared. The material presented in this chapter appeared in [93].

## 5.1 Quantum Soliton Propagation

We briefly review in this section the quantum theory based on the nonlinear Schrödinger equation. More details and references can be found in [104]. We assume that $\beta_2 < 0$ throughout this chapter. We first introduce the notations

$$\begin{aligned} c &= -\frac{\kappa}{|\beta_2|\, v_g}, && (5.1)\\ x &= v_g \tau, && (5.2)\\ t &= \frac{v_g^2\, |\beta_2|\, z}{2,} && (5.3)\\ \hat{\phi}(t,x) &= \frac{1}{\sqrt{v_g}} \hat{A}(z,\tau), && (5.4) \end{aligned}$$

so that $x$ is a distance, $t$ is the square of a length, and $c$ has units of inverse length. For $\kappa = 4 \times 10^{-19} s/km$, $v_g = 2 \times 10^8 m/s$ and $\beta_2 = -20 ps^2/km$, we have $c^{-1} = 10 km$. The normalization of the field was chosen such that

$$\begin{aligned} [\hat{\phi}(t,x), \hat{\phi}^\dagger(t,x')] &= \delta(x-x'), \\ [\hat{\phi}(t,x), \hat{\phi}(t,x')] &= [\hat{\phi}^\dagger(t,x), \hat{\phi}^\dagger(t,x')] = 0. \end{aligned} \quad (5.5)$$

Introducing the above variables in (B.33), we find

$$i\frac{\partial}{\partial t}\hat{\phi}(t,x) = -\frac{\partial^2}{\partial x^2}\hat{\phi}(t,x) + 2c\,\hat{\phi}^\dagger(t,x)\hat{\phi}(t,x)\hat{\phi}(t,x), \tag{5.6}$$

which is the QNSE. Below we shall refer to $t$ as time and to $x$ as position to conform with standard terminology for this equation.

Many-particle states take the standard form

$$|\psi>=\sum_{n=0}^{\infty} a_n \frac{1}{\sqrt{n!}}\int d\{x_i\} f_n(x_1,\cdots,x_n,t)\hat{\phi}^+(x_1),\cdots,\hat{\phi}^+(x_n)|0>, \tag{5.7}$$

where the $n$-particle wave functions $f_n(x_1,\cdots,x_n,t)$ are normalized so that the coefficients $a_n$ determine the photostatistics. The evolution of the $n$-particle wavefunctions is governed by the Schrödinger equation

$$i\hbar\frac{d}{dt}|\psi>=\hat{H}|\psi>, \tag{5.8}$$

where the operator $\hat{H}$ is

$$\hat{H} = \hbar\int \frac{\partial}{\partial x}\hat{\phi}^+(x)\frac{\partial}{\partial x}\hat{\phi}(x)dx + c\int \hat{\phi}^+(x)\hat{\phi}^+(x)\hat{\phi}(x)\hat{\phi}(x)dx. \tag{5.9}$$

Note that $\hat{H}$ preserves both the particle number

$$\hat{N} = \int \hat{\phi}^\dagger(x)\hat{\phi}(x)dx \tag{5.10}$$

and the total momentum

$$\hat{P} = i\frac{\hbar}{2}\int\left(\frac{\partial}{\partial x}\hat{\phi}^\dagger(x)\hat{\phi}(x) - \hat{\phi}^\dagger(x)\frac{\partial}{\partial x}\hat{\phi}(x)\right)dx. \tag{5.11}$$

One also verifies that the photon number and momentum operators commute so that common eigenstates of $\hat{H}$, $\hat{P}$ and $\hat{N}$ can be found. Because $c$ is negative, the Schrödinger equation (5.8) has bound states. A subset of these bound states is characterized solely by the eigenvalues of $\hat{N}$ and $\hat{P}$. The wave functions of these states

are

$$f_{n,p} = N_n \exp\left[ip\sum_{j=1}^{n} x_j + \frac{c}{2}\sum_{1\le i,j<n}|x_i - x_j|\right], \tag{5.12}$$

where $N_n$ is a normalization constant,

$$N_n = \sqrt{\frac{(n-1)!|c|^{n-1}}{2\pi}}. \tag{5.13}$$

Using $f_{n,p}$ in (5.7) one obtains the $|n,p>$ Bethe states

$$|n,p> \equiv \frac{1}{\sqrt{n!}}\int d\{x_i\} f_{n,p}(x_1,\cdots,x_n,t)\hat{\phi}^+(x_1),\cdots,\hat{\phi}^+(x_n)|0> . \tag{5.14}$$

The wavefunction $f_{n,p}$ decays exponentially with the separation between any boson pair. It describes an n-particle bound state with momentum $P = n\hbar p$. The state $|n,p>$ is an eigenstate of $\hat{H}$ with eigenvalue

$$E(n,p) = np^2 - \frac{|c|^2}{12}n(n^2-1). \tag{5.15}$$

Fundamental soliton states are defined as arbitrary superpositions of $|n,p>$ states

$$|\psi> = \sum_{n=0}^{\infty} a_n \int dp\, g_n(p)|n,p> . \tag{5.16}$$

The normalized function $|g_n(p)|^2$ is the momentum distribution in the $n$-particle subspace.

## 5.2 Poisson-Gaussian Fundamental Solitons

In this section, we consider fundamental solitons with a poissonian photostatistics

$$a_n \equiv \sqrt{p_n} = e^{-\frac{n_0}{2}}\frac{n_0^{n/2}}{\sqrt{n!}}. \tag{5.17}$$

$c_n$ is the probability to have exactly $n$ photons in the bound state. The average photon number and the photovariance in the corresponding states are

$$\left\langle \hat{N} \right\rangle = n_0, \tag{5.18}$$

$$\left\langle \hat{N}^2 \right\rangle - \left\langle \hat{N} \right\rangle^2 = n_0. \tag{5.19}$$

The momentum distribution is assumed gaussian

$$g_n(p) = \sqrt{g(p)} e^{-inpx_0} \quad \text{with} \quad g(p) = \frac{1}{\sqrt{2\pi}\Delta p} \exp\left[ -\frac{1}{2} \frac{(p-p_0)^2}{(\Delta p)^2} \right]. \tag{5.20}$$

The gaussian $g(p)$ describes the momentum distribution in every $n$-particle space. The parameter $x_0$ is real, and will subsequently be identified as the average position of the soliton at $t = 0$. Similarly, $\hbar p_0$ is the average momentum per photon. The above expressions for $a_n$ and $g_n(p)$ were proposed by Lai and Haus in [104] who studied the expectation value of $\hat{\phi}(t,x)$ in the corresponding fundamental soliton state (note however the different definitions of $g(p)$ and $\Delta p$ used by these authors). They pointed out that the width of the momentum distribution must satisfy

$$|c| \ll \Delta p \ll n_0. \tag{5.21}$$

The lower bound is needed initially to localize the bound state in a region smaller than the classical width of the soliton. The upper bound arises from the requirement that quantum dispersion be negligible over a classical soliton period. The above two conditions therefore give to the quantum bound state properties that are close to those of a classical soliton. We will show in Section 5.4 that when one uses

$$\Delta p = \sqrt{\frac{n_0}{\mu}} \frac{|c|}{2}, \tag{5.22}$$

with $\mu$ of order unity compared to $n_0$, the fluctuations in position and momentum at $t = 0$ reach the lower bound set by the uncertainty relations. Note that the above expression is compatible with the constraints (5.21). To evaluate the noise of

[illegible]soliton operators and the noise reduction ratio associated with the above Poisson-Gaussian fundamental solitons, we first consider the expectation value and the second order moments of the [illegible]eld.

### 5.[illegible].1 [illegible]he Field Expectation Value

Following [104], we use the matrix elements between n-particle soliton states (derived in Appendix E) to evaluate the expectation value of the field in the above state. The following expression is obtained in Appendix G

$$< \psi(t)|\hat{\phi}(x)|\psi(t) >= \sum_{n=0}^{\infty} p_n \frac{\sqrt{n_0|c|}}{2}\sqrt{n}\exp\left[i\frac{|c|^2}{4}n(n+1)t\right]\int dv g(v) e^{i(x-x_0)v - iv^2 t}$$
$$\times \left\{1 + \frac{1}{4n} + \frac{x_n(v)}{2n}\frac{\partial}{\partial x_n}\left(\frac{\mu + 2i\Phi_{nl}/n_0}{8n_0} - \frac{1}{4n}\right)\frac{\partial^2}{\partial x_{n+1/2}^2} + O\left(\frac{1}{n^2}\right)\right\}\mathrm{sech}\left(x_n(v)\right), \tag{5.23}$$

with the abbreviations

$$\Phi_{nl} = \frac{n_0 |c|^2}{4}t, \tag{5.24}$$
$$x_n(v) = \frac{|c|n}{2}(x - x_0 - 2v\,t). \tag{5.25}$$

To obtain (5.23), we assumed

$$n_0 \gg 1, \tag{5.26}$$
$$\mu \simeq 1, \tag{5.27}$$
$$\Phi_{nl} < n_0. \tag{5.28}$$

This expression generalizes the result obtained by Lai and Haus where the terms following 1 in brackets were neglected. Note that these authors had $n$ replaced by $n + 1/2$ in $x_n$. The additional $1/2$ is included as the third term within brackets in our expression.

We seek an expression for the mean field including terms of order $n_0$, which domi-

nate in the classical limit, and noise terms of order 1. As pointed out by Lai and Haus, the term of order $n_0$ reproduces the classical soliton. Corrections to this profile arise both initially and over the time evolution. At $\Phi_{nl} = 0$, the mean field deviates from a classical soliton due, in part, to the imperfect localization of the bound state position resulting from the finite width of the momentum distribution. Similarly, phase noise is present at $\Phi_{nl} = 0$ due to the finite width of the Poisson photodistribution. Other corrections to the initial classical profile cannot be attributed to the widths of the distributions in $n$ and $p$ and should be considered as intrinsic properties of Bethe eigenstates used to construct fundamental solitons. The second type of corrections to the classical soliton profile takes place during propagation. As the phase of the Bethe states with different values of $n$ and $p$ walk out of step, the mean field slowly collapses. As the nonlinear phase shift becomes larger, it becomes increasingly difficult to sum and integrate the terms associated with different photon numbers and momenta in (5.23). In Appendix G, we perform the sum over $n$ and obtain an expression for the mean field valid for $\Phi_{nl} < n_0$. Restricting ourselves further to $\Phi_{nl} \ll \sqrt{n_0}$, we are also able to carry out the momentum integral (i.e. the integral over $v$). This complicated-looking expression is used in Section 5.3 to obtain squeezing curves for large phase shifts. Here we provide the much simpler expression obtained when $\Phi_{nl}$ is of order 1. Defining the classical soliton profile as

$$\phi_0(t,x) = \frac{n_0\,|c|^{1/2}}{2} \exp(i\Phi_{nl} - ip_0^2 t + ip_0(x - x_0))\mathrm{sech}\left(x_{n_0}(p_0)\right), \tag{5.29}$$

we find for $p_0 = 0$,

$$< \psi(t)|\hat{\phi}(x)|\psi(t) >= \phi_0(t,x)\left(1 + \frac{\Delta(t,x)}{n_0}\right), \tag{5.30}$$

where

$$\Delta(t,x) = i\Phi_{nl}\left(1 - \frac{1}{\mu}\right) - 2\Phi_{nl}^2 + \frac{\mu}{4}\tanh^2 x_{n_0} - \frac{x_{n_0}^2}{2} + \frac{2-\mu}{8}, \tag{5.31}$$

with $x_{n_0} = n|c|/2$. The first term in $\Delta$ indicates that the phase of the mean field walks off from the classical soliton phase as $t$ increases. The following term signals

the uncertainty on the phase of the field increases during propagation, resulting in a damping of its expectation value. The last three terms of (5.31) give the initial corrections to the classical soliton profile and are independent of $t$ when $p_0 = 0$. For large values of $\mu$, the momentum of the bound state is increasingly well-defined, but substantial deviations from the classical profile occur in the initial mean field. When $\mu$ is chosen small on the other hand, the phase walk-off of the field increases more rapidly.

### 5.2.2 Noise Correlators

The second order correlation functions of the field, $< \psi(t)|\hat{\phi}(x)\hat{\phi}(x+\tau)|\psi(t) >$ and $< \psi(t)|\hat{\phi}^\dagger(x)\hat{\phi}(x+\tau)|\psi(t) >$, are evaluated in Appendix H using the same technique as for the mean field (Appendix E through G). We define the quantum noise operator $\hat{v}(t,x)$ such that

$$\hat{\phi}(t,x) = \left\langle \hat{\phi}(t,x) \right\rangle + \hat{v}(t,x). \tag{5.32}$$

Subtracting the mean field from the two-point correlators, we find the noise covariances $< \hat{v}^\dagger(x)\,\hat{v}(y$ $) >$ and $< \hat{v}(x)\,\hat{v}(y) >$. Instead of providing thes for large nonlinear phase shifts here, we restrict ourselves once again to the case $\Phi_{nl} = O(1)$. Defining the classical soliton width as

$$\tau_{n_0} = \frac{2}{n_0\,|c|}, \tag{5.33}$$

we find

$$\begin{aligned}
< \hat{v}^\dagger(x)\hat{v}(x+\tau) >= \frac{n_0|c|}{4}\Bigg\{ & \left(4\Phi_{nl}^2 + \frac{3}{4} + \frac{1}{2\mu}x_{n_0}(x_{n_0}+\tau_{n_0})\right)\mathrm{sech}(x_{n_0})\mathrm{sech}(x_{n_0}+\tau_{n_0}) \\
& + \left(\frac{\mu-2}{4} + x_{n_0}(x_{n_0}+\tau_{n_0}) + \frac{2\Phi_{nl}^2}{\mu}\right)\mathrm{sech}'(x_{n_0})\mathrm{sech}'(x_{n_0}+\tau_{n_0}) \\
& + \frac{1}{2}\left(|\tau_{n_0}|\cosh(\tau_{n_0}) - \sinh(|\tau_{n_0}|)\right)\mathrm{sech}^2(x_{n_0})\mathrm{sech}^2(x_{n_0}+\tau_{n_0}) \\
& + (x_{n_0}+\tau_{n_0})\mathrm{sech}'(x_{n_0}+\tau_{n_0})\mathrm{sech}(x_{n_0}) + x_{n_0}\mathrm{sech}'(x_{n_0})\mathrm{sech}(x_{n_0}+\tau_{n_0}) \\
& - i\Phi_{nl}\left(2(x_{n_0}\mathrm{sech}'(x_{n_0})\mathrm{sech}(x_{n_0}+\tau_{n_0}) - (x_{n_0}+\tau_{n_0})\mathrm{sech}'(x_{n_0}+\tau_{n_0})\mathrm{sech}(x_{n_0})\right)
\end{aligned} \tag{5.34}$$

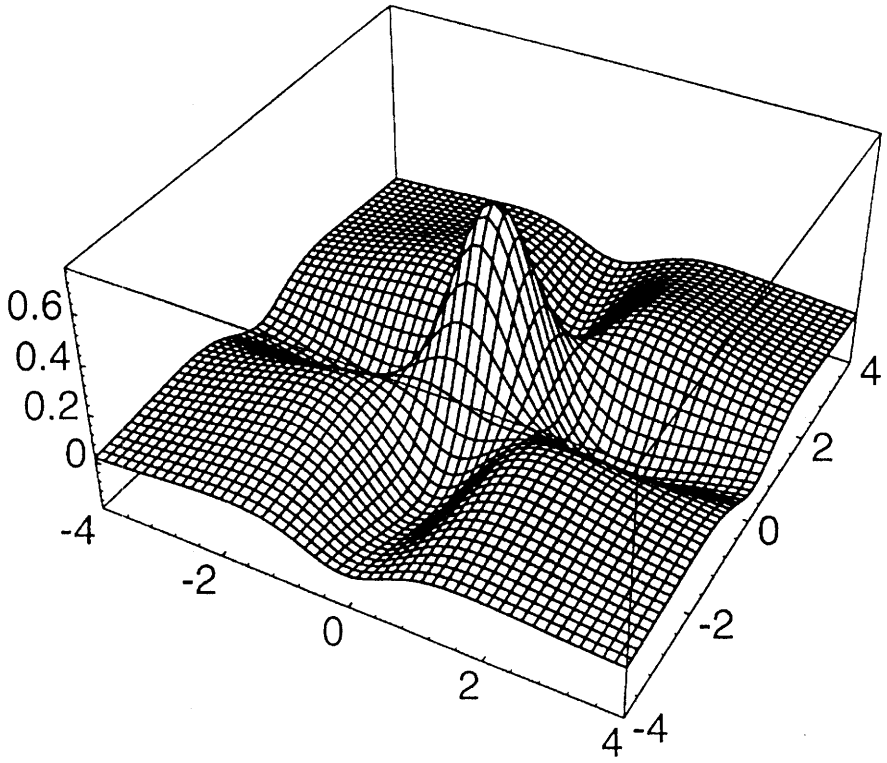


Figure 5-1: Correlation function $< \hat{v}^{\dagger}(x)\hat{v}(y) >$ for a minimum uncertainty fundamental soliton.

$$+\frac{2}{\mu}((x_{n_0}+\tau_{n_0})\mathrm{sech}'(x_{n_0})\mathrm{sech}(x_{n_0}+\tau_{n_0})-x_{n_0}\mathrm{sech}'(x_{n_0}+\tau_{n_0})\mathrm{sech}(x_{n_0}))\Bigg)\Bigg\}$$

and

$$\begin{aligned}
<\hat{v}(x)\,\hat{v}(x+\tau)>=\frac{n_0|c|}{4}\Bigg\{&\left(-4\Phi_{nl}^2+\frac{5}{4}-|\tau_{n_0}|-\frac{1}{\mu}x_{n_0}(x_{n_0}+\tau_{n_0})\right)\mathrm{sech}(x_{n_0})\mathrm{sech}(x_{n_0}+\tau_{n_0})\\
&+\left(\frac{\mu-2}{4}+x_{n_0}(x_{n_0}+\tau_{n_0})+\frac{2\Phi_{nl}^2}{\mu}\right)\mathrm{sech}'(x_{n_0})\mathrm{sech}'(x_{n_0}+\tau_{n_0})\\
&+\frac{1}{2}\left(|\tau_{n_0}|\cosh(\tau_{n_0})-\sinh(|\tau_{n_0}|)\right)\mathrm{sech}^2(x_{n_0})\mathrm{sech}^2(x_{n_0}+\tau_{n_0})\\
&+(x_{n_0}+\tau_{n_0})\mathrm{sech}'(x_{n_0}+\tau_{n_0})\mathrm{sech}(x_{n_0})+x_{n_0}\mathrm{sech}'(x_{n_0})\mathrm{sech}(x_{n_0}+\tau_{n_0})\\
&+i\Phi_{nl}\,(4\mathrm{sech}(x_{n_0})\mathrm{sech}(x_{n_0}+\tau_{n_0})\\
&+2(x_{n_0}\mathrm{sech}'(x_{n_0})\mathrm{sech}(x_{n_0}+\tau_{n_0})+(x_{n_0}+\tau_{n_0})\mathrm{sech}'(x_{n_0}+\tau_{n_0})\mathrm{sech}x_{n_0}))\\
&-\frac{2}{\mu}((x_{n_0}+\tau_{n_0})\mathrm{sech}'(x_{n_0})\mathrm{sech}(x_{n_0}+\tau_{n_0})+x_{n_0}\mathrm{sech}'(x_{n_0}+\tau_{n_0})\mathrm{sech}(x_{n_0}))\Bigg)\Bigg\}
\end{aligned}\tag{5.35}$$

where the primes denote derivatives with respect to the corresponding argument. Initially, when $\Phi_{nl}=0$, these two correlation functions are real and are shown in Fig.

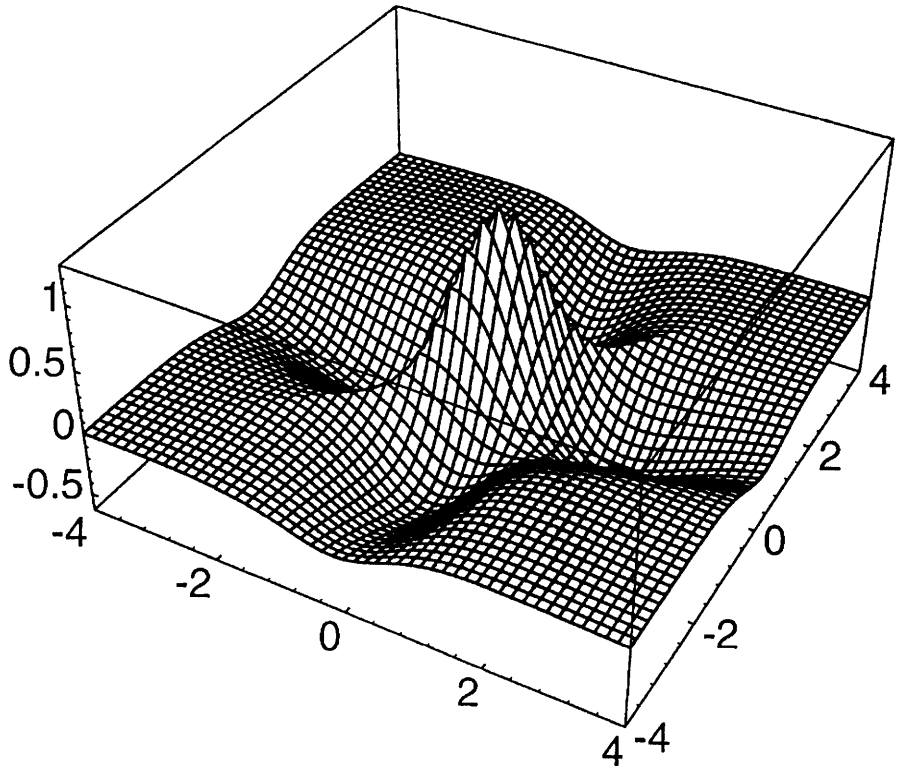


Figure 5-2: Correlation function $< \hat{v}(x)\hat{v}(y) >$ for a minimum uncertainty fundamental soliton.

5-1 and Fig. 5-2. In contrast to coherent states, the quantum noise of the fundamental soliton is not white. This indicates that correlations among the particles are created by the Kerr effect.

## 5.3 Squeezing

In this section, we use expressions (G.5), (H.3) and (H.6) to derive a scale for the phase shift beyond which the linearized theory fails to describe quantum noise correctly. To evaluate the covariance functions with $\Phi_{nl} = O(1)$ in Section 5.2.2, we neglected terms of the form

$$n_0 \left( \frac{\Phi_{nl}^2}{n_0} \right)^2 \tag{5.36}$$

This led to the linearized expressions for these correlators. When the nonlinear phase becomes of order $n_0^{1/4}$, the neglected terms become important and the linearization fails. To show this, we evaluate the variance of the field quadratures associated with

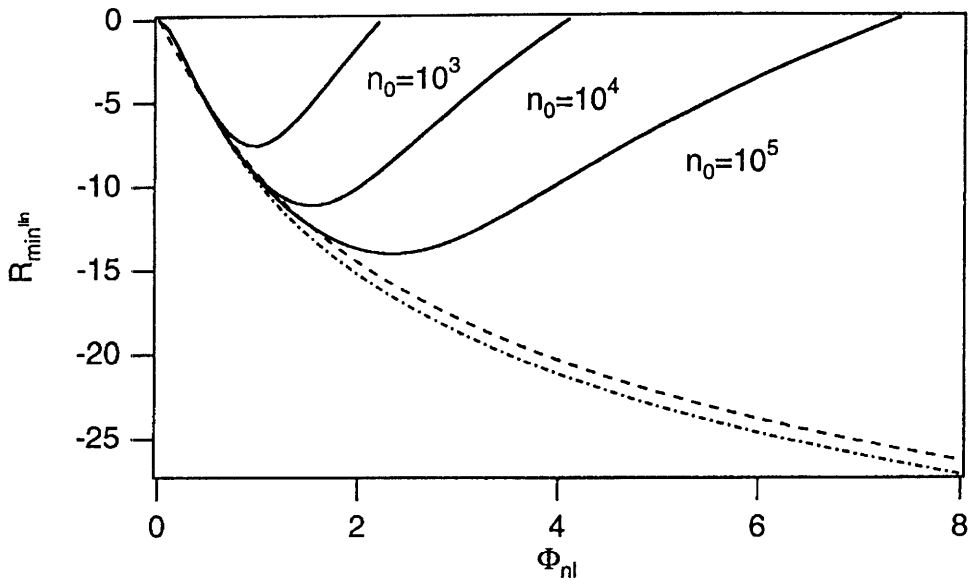


Figure 5-3: Reduction of quadrature fluctuations in a homodyne experiment with a sech - shape local oscillator normalized to the standard quantum limit for photon numbers $10^3 - 10^5$, (-.-.-) linearized result, (- - -) linearized noise reduction for a coherent initial state and optimum local oscillator according to Ref.[HausLai]

the mode

$$\hat{a} = \frac{1}{\sqrt{n_0}} \int \phi^*_{0,n_0}(x,t)\ \hat{\phi}^\dagger(x,t)dx. \tag{5.37}$$

The quadrature noise reduction ratio for this mode is (see (2.5) and (2.1))

$$R^{lin} = 2 \min_\theta < \Delta^2 \hat{Q}_\theta >= 1 + 2\left( < \hat{a}^\dagger \hat{a} > - < \hat{a}^\dagger >< \hat{a} > - | < a^2 > - < a >^2 | \right). \tag{5.38}$$

The expectation values can be expressed in terms of the correlation functions (G.5), (H.3) and (H.6). The result is shown in Fig. 5-3 as a series of solid lines corresponding to increasing photon numbers. The dashed - dotted line is the linearized result obtained by neglecting terms of order $n_0 \left(\frac{\Phi^2_{nl}}{n_0}\right)^2$ in the correlation functions. When the photon number is increased by a factor of 10 the range of phase shifts where the noise reduction follows the linearized result increases as predicted by $10^{1/4} \approx 1.8$. Squeezing experiments use pulses with $n_0 \simeq 10^9$. The linearized approximation should therefore describe properly the evolution of quantum noise for phase shifts up to 100. The dis-

crepancy between the soliton squeezing predictions and the poor results obtained in laboratory [34, 35] can therefore not be attributed to a failure of the linearized theory. It is interesting to note that the slope of the noise reduction ratio vanishes at $\phi = 0$ for the Poisson-Gaussian soliton states. This behavior contrasts with that of initial coherent states[60]. The corresponding linearized squeezing curve is represented by a dashed line in Fig. 5-3 where an optimum local oscillator was used.

## 5.4 Collective Coordinate Fluctuation Operators

The question of the relationship between the QNSE bound states and the classical solitons has been the focus of considerable attention in the last 20 years [101, 102, 103, 104, 105]. We contribute to this analysis in this section by evaluating the variance of the four soliton collective coordinates in a Poisson-Gaussian soliton state at $t = 0$.

### 5.4.1 Soliton Operators

Introducing the decomposition (5.32) in the definition of the total momentum and photon number operators, we find

$$\hat{N} = n_0 + \Delta\hat{n} \tag{5.39}$$

$$n_0 = \int dx < \hat{\phi}^\dagger(x) >< \hat{\phi}(x) > \tag{5.40}$$

$$\Delta\hat{n} = \int dx < \hat{\phi}^\dagger(x) > \hat{v}(x) \; + h.c., \tag{5.41}$$

$$\hat{P} = \hbar n_0 p_0 + \hbar n_0 \Delta\hat{p} \tag{5.42}$$

$$p_0 = \frac{i}{n_0}\int dx < \hat{\phi}_x^\dagger(x) >< \hat{\phi}(x) > \tag{5.43}$$

$$\Delta\hat{p} = \frac{i}{n_0}\int dx < \hat{\phi}_x^\dagger(x) > \hat{v}(x) \; + h.c. \tag{5.44}$$

By construction, the quantum number $p$ in $|n,p>$ is related to the momentum of the center coordinate of the $n$ interacting bosons which is defined as

$$\hat{X} = \lim_{\epsilon \to 0} \int x \, \hat{\phi}^\dagger(x) \hat{\phi}(x) dx (\epsilon + \hat{N})^{-1}. \tag{5.45}$$

The limit over $\epsilon$ is introduced to regularize the position operator for the vacuum state. Introducing the decomposition (5.32) in the expression for $\hat{X}$ we have

$$\hat{X} = x_0 \left(1 - \frac{\Delta\hat{n}}{n_0}\right) + \Delta\hat{x} \tag{5.46}$$

$$x_0 = \frac{1}{n_0} \int dx \, x < \hat{\phi}^\dagger(x) >< \hat{\phi}(x) > \tag{5.47}$$

$$\Delta\hat{x} = \frac{1}{n_0} \int dx \, x < \hat{\phi}^\dagger(x) > \hat{v}(x) \; + h.c.. \tag{5.48}$$

Note that $n_0 \Delta\hat{p}$ and $\Delta\hat{x}$ form a conjugated pair

$$[n_0 \Delta\hat{p}, \Delta\hat{x}] = i. \tag{5.49}$$

To complete this set of collective coordinate fluctuation operators, we introduce the operator conjugated to $\Delta\hat{n}$

$$\Delta\hat{\theta} = \frac{1}{n_0} \int dx \left( i \left( < \hat{\phi}^\dagger(x) > + x < \hat{\phi}^\dagger_x(x) > \right) - p_0 x < \hat{\phi}^\dagger(x) > \right) \hat{v}(x) + h.c., \tag{5.50}$$

from which

$$[\Delta\hat{n}, \Delta\hat{\theta}] = i. \tag{5.51}$$

The four fluctuation operators $\Delta\hat{n}$, $\Delta\hat{\theta}$, $\Delta\hat{p}$ and$\Delta\hat{x}$ are *unnormalized* quadratures of the noise operator. Since condition (2.45) is not satisfied, the variance of these operators in a coherent state is not given by (2.52). Instead, we find [60]

$$< \Delta\hat{n}_0^2 > = n_0 \tag{5.52}$$

$$< \Delta\hat{\theta}_0^2 > = \frac{0.6075}{n_0} \tag{5.53}$$

$$< \Delta\hat{p}_0^2 > \;=\; \frac{1}{3n_0\tau_{n_0}^2} \tag{5.54}$$

$$< \Delta\hat{x}_0^2 > \;=\; \frac{1.645\,\tau_{n_0}^2}{2\,n_0} \tag{5.55}$$

where $\tau_{n_0}$ was defined by (5.33). The following uncertainty products,

$$< \Delta\hat{n}_0^2 >< \Delta\hat{\theta}_0^2 > \;=\; 0.6075 \geq 0.25, \tag{5.56}$$

$$n_0^2 < \Delta\hat{p}_0^2 >< \Delta\hat{x}_0^2 > \;=\; 0.27 \geq 0.25. \tag{5.57}$$

indicate that coherent states do not minimize the fluctuations of the collective variables.

### 5.4.2 Poisson-Gaussian Soliton Fluctuations

Consider now the variance of the collective variables in Poisson-Gaussian soliton states for small phase shifts. Using expression (5.30) for the mean field with $x_0 = p_0 = 0$, we obtain

$$\begin{aligned} < \Delta\hat{x}_i\, \Delta\hat{x}_j > &= \int\int dxdy \underline{f}_i^*(x)\underline{f}_j(y) \\ &+ \; 2Re\left\{ \int\int dxdy \underline{f}_i^*(x)\underline{f}_j^*(y) < \hat{v}(x)\, \hat{v}(y) > + \underline{f}_i(x)\underline{f}_j^*(y) < \hat{v}^\dagger(x)\, \hat{v}(y) > \right\} \end{aligned} \tag{5.58}$$

where $\Delta\hat{x}_i$ or $\Delta\hat{x}_j$ can be any of the four soliton operators, and where the adjoint functions [60] are

$$\underline{f}_n(x) \;=\; \frac{n_0|c|^{1/2}}{2}\text{sech}\,(x_{n_0}) \tag{5.59}$$

$$\underline{f}_\theta(x) \;=\; \frac{i|c|^{1/2}}{2}\left(\text{sech}\,(x_{n_0}) + x_{n_0}\frac{d}{dx_{n_0}}\text{sech}\,(x_{n_0})\right) \tag{5.60}$$

$$\underline{f}_p(x) \;=\; \frac{-in_0|c|^{3/2}}{4}\frac{d}{dx_{n_0}}\text{sech}\,(x_{n_0}) \tag{5.61}$$

$$\underline{f}_x(x) \;=\; \frac{1}{n_0|c|^{1/2}}x_{n_0}\text{sech}\,(x_{n_0}) \tag{5.62}$$

with $x_{n_0} = \frac{n_0|c|}{2}x$. The evaluation of the integrals in (5.58) using (5.34) and (5.35) is straightforward but lengthy. The photon number and momentum variances obtained this way are, of course, identical to those used in $a_n$ and $g(p)$

$$< \Delta\hat{n}^2 >= n_0, \qquad < \Delta\hat{p}^2 >= \frac{1}{\mu n_0 \tau_{n_0}^2}. \tag{5.63}$$

These values are time independent because $N$ and $P$ are constants of motion. The phase variance for Poisson-Gaussian soliton is found to be

$$< \Delta\hat{\theta}^2 >=< \Delta\hat{\theta}_0^2 > +4\frac{\Phi_{nl}^2}{n_0} \tag{5.64}$$

with the initial phase fluctuations

$$< \Delta\hat{\theta}_0^2 >= \frac{0.25}{< \Delta\hat{n}^2 >}. \tag{5.65}$$

Similarly, the uncertainty on the bound state position is given by

$$< \Delta\hat{x}^2 >=< \Delta\hat{x}_0^2 > +2\frac{\Phi_{nl}^2}{n_0}\frac{\tau_{n_0}^2}{\mu} \tag{5.66}$$

with the initial position fluctuations

$$< \Delta\hat{x}_0^2 >= \frac{0.25\mu\tau_{n_0}^2}{n_0} = \frac{0.25}{< n_0^2\Delta\hat{p}^2 >}. \tag{5.67}$$

As we anticipated in Section 5.2, Poisson-Gaussian solitons are minimum uncertainty states for the four collective soliton operators. The parameter $\mu$ determines the relative magnitudes of the position and momentum uncertainties.

# Chapter 6

# Quantum Polarization Cross-Phase Modulation

In previous chapters, we considered the evolution of quantum noise in truly single-mode silica waveguides. We assumed in particular that the degeneracy between modes of orthogonal polarizations was lifted by breaking the circular symmetry of the effective index, as in polarization maintaining fibers. This chapter considers the evolution of quantum noise in fibers where this symmetry is not broken. In Section 6.1, we consider the effect of an intense linearly polarized pulse on the vacuum fluctuations of the cross-polarized modes in these low birefringence fibers. We show that as a result of the nonlinear interaction between the pulse and the noise, the latter is squeezed during propagation. In Section 6.2, we show that the cross-polarized quantum noise, in turn, depolarizes the pulse. The squeezer presented in Section 6.1 was proposed in [114]. The results of Section 6.2 were not yet published.

## 6.1 Squeezed Vacuum from Polarization XPM

In Section 3.1, we showed that in order to produce a squeezed vacuum using self-phase modulation (SPM) in a fiber, the latter must be inserted into a Sagnac interferometer. In this section, we propose a different method to generate a squeezed vacuum with an optical fiber. This approach uses cross-phase modulation (XPM) between

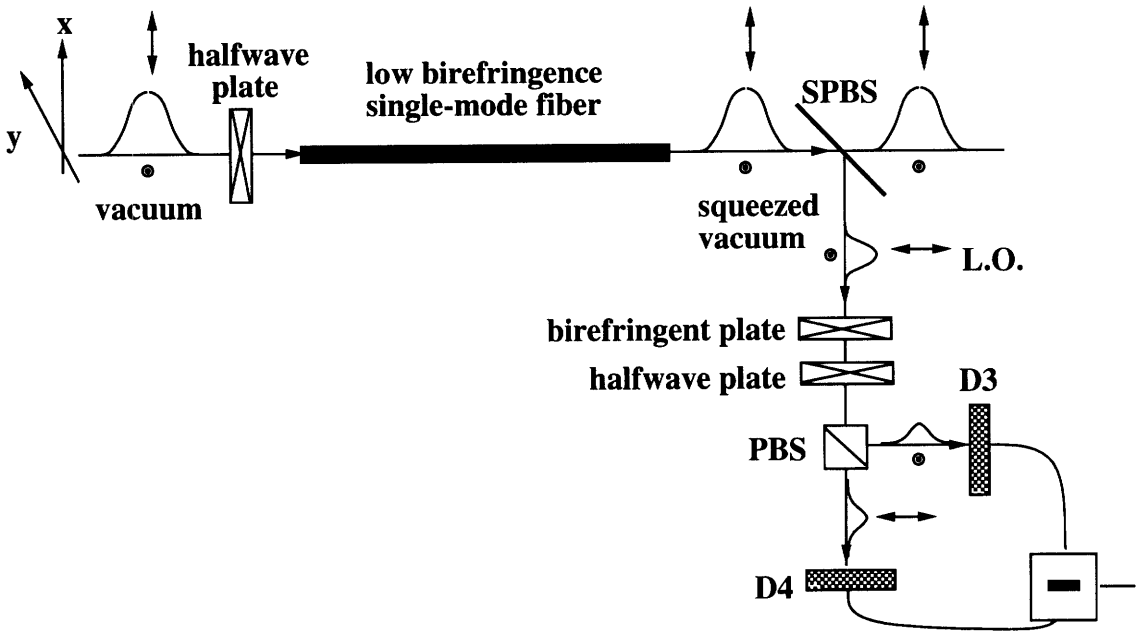


Figure 6-1: XPM squeezer

optical modes of identical carrier frequencies, but with perpendicular polarizations. Polarization XPM makes it possible to generate a squeezed vacuum directly out of a low birefringence fiber and therefore eliminates the need for a Sagnac interferometer.

### 6.1.1 Physical Picture

Our squeezer is shown on Figure 6-1 [114]. An incoming pulse, linearly polarized along the $x$-axis, is coupled into a low birefringence fiber. This pulse creates a parametric interaction coupling the creation and annihilation operators of the $y$-polarized modes. This phenomenon arises because the carrier frequency and the carrier wavelength of the pulse match those of a band of $y$-polarized modes. As a result, the quantum state of these modes, initially in vacuum, is that of a squeezed vacuum at the output of the waveguide. At this point, a special polarization sensitive beamsplitter (SPBS) is used to deflect part of the $x$-polarized pump and all of the $y$-polarized squeezed light. The attenuated pump is used as the local oscillator in a balanced homodyne detection scheme. The relative phase between squeezed light and the local oscillator is adjusted using a birefringent plate. For a proper choice of this phase, the output

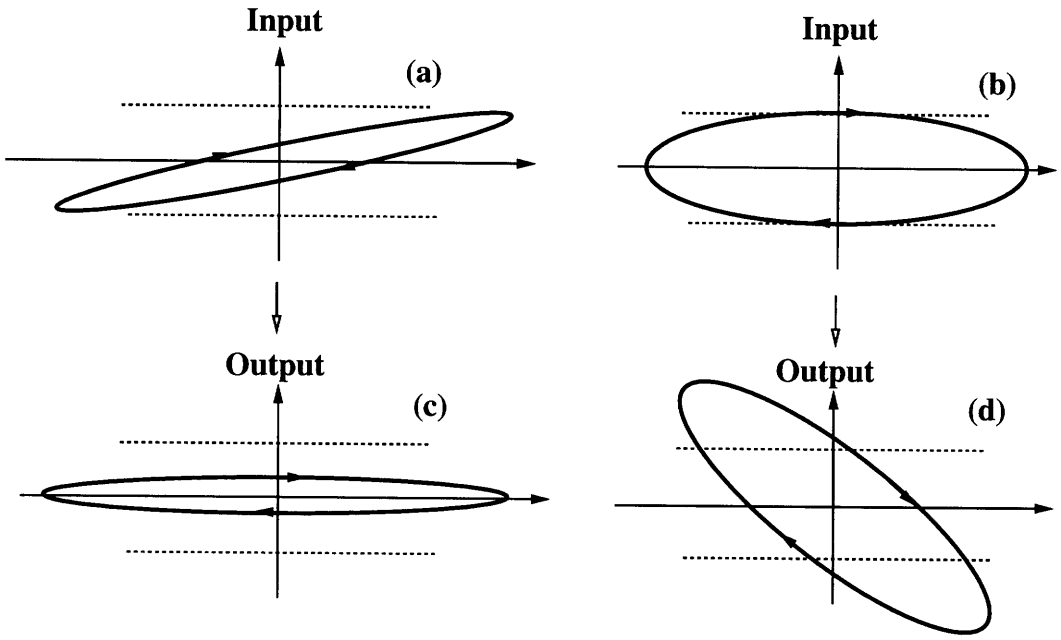


Figure 6-2: Polarization ellipses

photocurrent fluctuations of the balanced detector are below the shot noise level.

The noise reduction process described above can be understood physically in terms of nonlinear polarization rotation. Suppose a small (one photon) $y$-polarized signal is coupled in the fiber and leads the pump by a phase $\theta$. The ellipticity and the helicity of the field are controlled by $\theta$, as shown on Fig. 6-2(a) and Fig.6-2(b). All possible ellipses have the same projection on the $y$ axis, but the width of their minor axis depends on $\theta$. The Kerr effect in the fiber core results in the precession of the polarization ellipse of the field [127]. The direction of nonlinear rotation is clockwise for $0 < \theta < \pi$ and counterclockwise for $-\pi < \theta < 0$. The rotation rate is maximum for $\theta = \pm\pi/2$ and decreases to zero for $\theta = 0, \pm\pi$. Due to this nonlinear effect, the projection of the polarization ellipse on the $y$ axis at the output of the fiber depends on the initial phase $\theta$, as can be seen on Fig.6-2(c) and Fig.6-2(d). Signals with the proper phase relative to the pump are initially deamplified by the nonlinear propagation, up to a minimum level given by the minor axis width of their polarization ellipse. Signals with narrower minor ellipses are more deamplified but require longer propagation distances to reach maximum deamplification due to their reduced nonlinear rotation

rate. The periodicity of nonlinear polarization rotation indicates that, over very long propagation distances, any signal is successively amplified and deamplified. When the signal arises from noise with a random phase relative to the pump, as is the case for vacuum fluctuations, one observes its deamplification for quadratures with the proper phase.

### 6.1.2 Equations of Motion

To assess quantitatively the performance of our squeezer, we analyze the linearized equations of motion for the quantum noise of the $y$-polarized modes. Consider first the classical equations for $A_x$ and $A_y$, which are the $x$ and $y$ polarized envelopes respectively. In fused silica fibers, most of the third order nonlinearity is of electronic origin [125, 126], and the nonlinear coefficients $\chi^{(3)}_{xxyy}$, $\chi^{(3)}_{xyxy}$ and $\chi^{(3)}_{xyyx}$ are all nearly equal. Taking these coefficients as being equal, one can derive simple evolution equations for the envelopes[54, 127]. Neglecting any residual birefringence effect in the fiber, we find

$$\frac{\partial A_x}{\partial z} = (D + iN_x)\, A_x + i\frac{\kappa}{3} A_y^2 A_x^*, \tag{6.1}$$

$$\frac{\partial A_y}{\partial z} = (D + iN_y)\, A_y + i\frac{\kappa}{3} A_x^2 A_y^*, \tag{6.2}$$

where the nonlinear Kerr operators are given by

$$N_x(z,\tau) = \kappa \left|A_x(z,\tau)\right|^2 + \frac{2\kappa}{3} \left|A_y(z,\tau)\right|^2, \tag{6.3}$$

$$N_y(z,\tau) = \kappa \left|A_y(z,\tau)\right|^2 + \frac{2\kappa}{3} \left|A_x(z,\tau)\right|^2. \tag{6.4}$$

As can be seen from these expressions, a field with a given polarization modifies its own refractive index and the cross-polarized index by different amounts. The last nonlinear terms on the left hand side of (6.1) and (6.2) are so-called coherence terms. They arise when the carrier frequencies and the wavenumbers of the perpendicularly polarized waves are degenerate. The generation of squeezed light through polarization XPM depends critically on the presence of the coherence term in the $y$ equation.

Linear birefringence of the fiber tends to randomize the relative phase between the two polarizations, canceling the effect of this term. For this reason our squeezer requires the use of a low birefringence fiber. External factors resulting in strain or stress of the fiber core should be avoided by a careful layout. Even in the best conditions however, residual birefringence resulting from the manufacturing process will remain. We consider only fibers much shorter than the corresponding residual beat length. For currently available low birefringence fibers, this implies propagation distances of less than about $1m$.

We are interested in the situation where the $y$ polarized modes are in vacuum in the $z = 0$ plane, corresponding to a $x$-polarized input pulse. Replacing $A_y$ by $\hat{a}_y$ in the above field equations and neglecting terms which are quadratic or cubic in this field. We find

$$\frac{\partial A_x}{\partial z} = DA_x + i\kappa \mid A_x \mid^2 A_x, \tag{6.5}$$

$$\frac{\partial \hat{a}_y}{\partial z} = D\hat{a}_y + i\frac{\kappa}{3}\left[2 \mid A_x \mid^2 \hat{a}_y + A_x^2 \hat{a}_y^\dagger\right]. \tag{6.6}$$

Note that the field operator satisfies the commutators

$$[\hat{a}_y(0,\tau), \hat{a}_y(0,\tau')] = 0, \;\; ; \;\; \left[\hat{a}_y(0,\tau), \hat{a}_y^\dagger(0,\tau')\right] = \delta(\tau - \tau'). \tag{6.7}$$

and that the state of the input fluctuations obeys

$$\hat{a}_y(0,\tau) \mid in\rangle = 0. \tag{6.8}$$

We do not need to quantize the $x$-polarized modes since their quantum fluctuations have little effect on squeezing of the transversely polarized modes.

The linearized set of equations can be integrated in closed-form in the absence of dispersion. Using the notation introduced in Section 3.2.2, we have

$$A_x(z,\tau) = e^{i\phi(z,\tau)}\alpha(\tau), \tag{6.9}$$

$$\hat{a}_y(z,\tau) = e^{i\phi(z,\tau)}\left\{\mu_y(z,\tau)\hat{a}_y(0,\tau) + \nu_y(z,\tau)\hat{a}_y^\dagger(0,\tau)\right\}, \tag{6.10}$$

where

$$\phi(z,\tau) = \kappa z \left|A_x(z,\tau)\right|^2 \tag{6.11}$$

$$\mu_y(z,\tau) = \left(1 - i\frac{\phi(z,\tau)}{3}\right), \tag{6.12}$$

$$\nu_y(z,\tau) = \left(i\frac{\kappa z}{3}\alpha^2(\tau)\right). \tag{6.13}$$

These expressions can be compared with the analogous formulae obtained for SPM-squeezing at zero dispersion (see (3.31) to (3.34)). Apart from the identical overall phase factor, expressions (6.10) and (3.32) differ by a factor 1/3 for the Kerr coefficient and by a sign. The $y$-polarized noise therefore experiences squeezing. Indeed, consider the integrated quadrature operators for the $y$-polarized modes

$$\hat{Q}_{y,\theta}(z) = \frac{1}{\sqrt{2n_0}}\int_{-\infty}^{\infty} d\tau \left\{e^{i\theta}A_x(z,\tau)\hat{a}_y^\dagger(z,\tau) + e^{-i\theta}A_x^*(z,\tau)\hat{a}_y(z,\tau)\right\}. \tag{6.14}$$

This operator is proportional to the balanced photocurrent measured on Fig. 6-1. From (6.10) and for the input vacuum state considered here, we have $\left\langle \hat{Q}_{y,\theta}(z)\right\rangle = 0$. Defining

$$R_{XPM}(z) \equiv \frac{\min_\theta \left\langle \Delta^2 \hat{Q}_{y,\theta}(z)\right\rangle}{\langle 0|\, \Delta^2 \hat{Q}_{y,\theta}\, |0\rangle}, \tag{6.15}$$

we have at zero dispersion

$$\begin{aligned} R_{XPM}^{lin}(z) &= 1 + \frac{2}{9}p_6\Phi^2 - \sqrt{\left(\frac{2}{9}p_6\Phi^2\right)^2 + \left(\frac{2}{3}p_4\Phi\right)^2} \\ &= R_{SPM}^{lin}\left(\frac{z}{3}\right), \end{aligned} \tag{6.16}$$

where $R_{SPM}^{lin}$ is given by (3.40). As can be seen, the smaller effective Kerr coefficient in $\mu_y$ and $\nu_y$ makes XPM-squeezing less efficient than the SPM-squeezing process. Note however that the interferometric scheme used to extract squeezed vacuum from the SPM-squeezed fluctuations requires a 50/50 splitting of the pump power at the fiber coupler. For this reason, only half of the optical power is actually used to generate squeezed light in each counterpropagating pulses. The scheme proposed here does

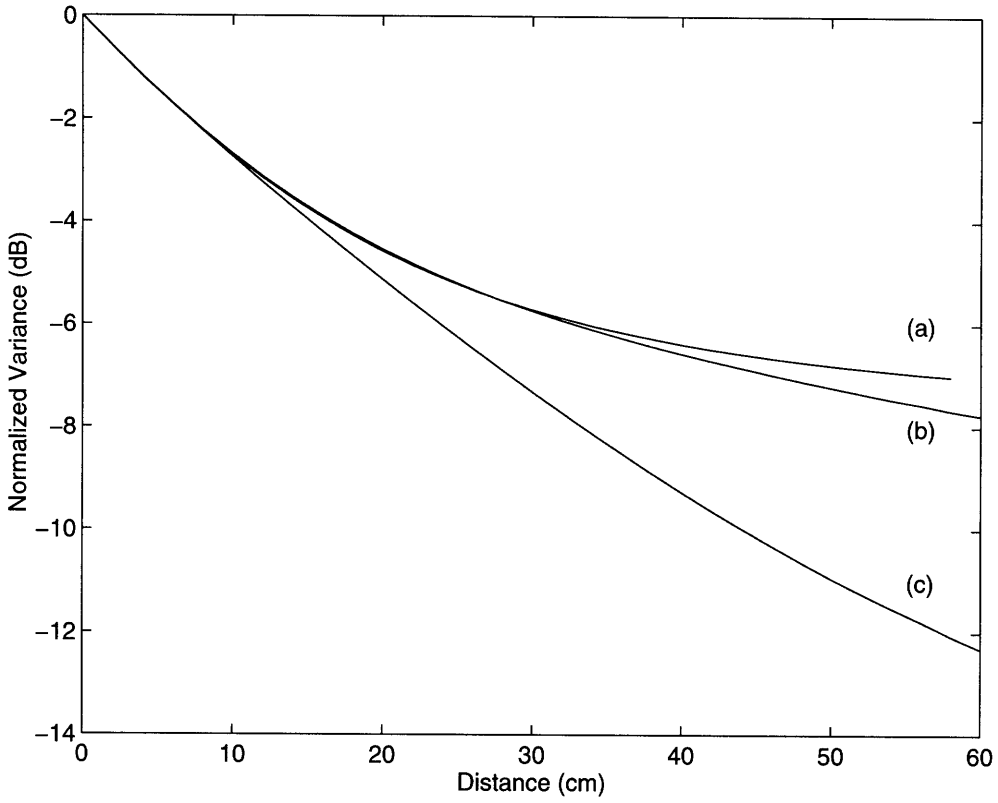


Figure 6-3: Linearized XPM squeezing with input sech pulses. (a)$\beta_2 = 0$, (b)$\beta_2 = 1ps^2/km$ and (c)$\beta_2 = -50ps^2/km$ (soliton).

not require such a splitting. For a given optical power, this method is therefore less efficient by a factor of 2/3 at zero dispersion. Figure 6-3 shows $R_{XPM}$ for unchirped sech input pulses, $\alpha(\tau) = \sqrt{n_0/2\sigma}\mathrm{sech}(\tau/\sigma)$, with $n_0 = 2.8\times10^9$ and $\sigma = 100fs/1.763$, corresponding to a peak power of about $5kW$ at $1\mu m$. Three dispersion regimes are illustrated: (a)$\beta_2 = 0$, (b)$\beta_2 = 1ps^2/km$ and (c)$\beta_2 = -50ps^2/km$ (soliton). The numerical approach developed in Section 3.3 was adapted to generate the curves with $\beta_2 \neq 0$. We used $\kappa = 6.2 \times 10^{-7} ps/km$ for all these curves.

When no dispersion is present, the output phase profile of the noise operator is identical to that of the pump, as can be seen from (6.9) and (6.10). This property is favorable to the measurement of squeezing by homodyne detection with the pump pulse used as the local oscillator. The presence of dispersion tends to spoil the matching of the phase profiles. This is illustrated on Fig. 6-4 which compares XPM- and SPM-squeezing for $\beta_2 > 0$. In this case, a dispersion penalty is incurred resulting in $R^{lin}_{XPM}(z) > R^{lin}_{SPM}(z/3)$.

In actual fibers, the orientation of the principal axis of polarization of the fiber

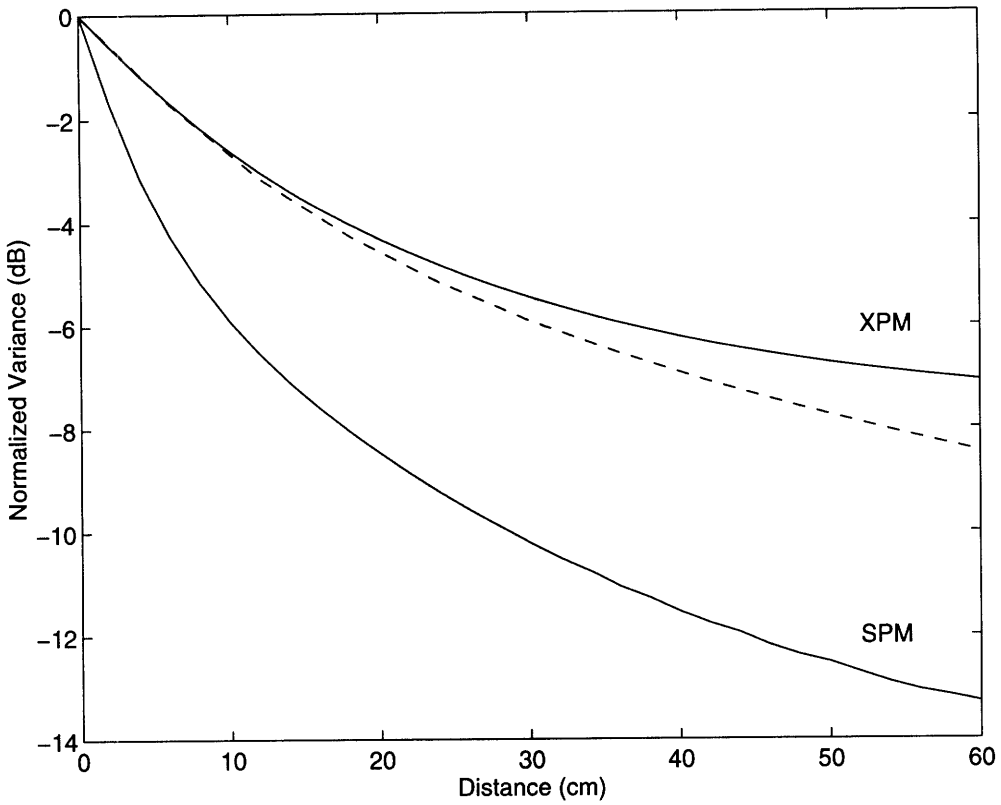


Figure 6-4: Comparison of XPM and SPM squeezing for $\beta_2 = 10ps^2/km$. All other parameters were chosen as in Fig. 3-8. The dashed curve is $R_{SPM}(z/3)$. The difference between this curve and the XPM curve is the dispersion penalty discussed in the text.

varies randomly as a function of $z$. When the polarization of the pump does not correspond with one of these principal axis of birefringence, (6.5) and (6.6) do not hold exactly, and part of the power of the pump is transferred to the $y$-polarized modes. An upper bound on the optical power $P_y$ scattered into the squeezed port can be obtained by assuming that the birefringence axis maintains a $45^0$ angle with respect to the input polarization of the pump for the whole propagation distance. This angle maximizes the power transferred and provides the worst scenario possible. In this case, we find $P_y = P_0 \sin^2(\pi z/L_B)$, where $P_0$ is the input pump power, and $L_B$ is the residual beat length of the fiber. Typically, low birefringence fibers have beat lengths between $30m$ and $50m$[128], so that $z/L_B \simeq 0.01 - 0.02$ on Fig.6-3 and Fig.6-4. One therefore expects at most 0.1% to 0.4% of the input pump power to be transferred to the squeezed port in these cases. These numbers are similar to those found for Sagnac squeezers when the imperfections of the fiber coupler are taken into account. As for these devices, light scattered in the squeezed port will not prevent the

observation of shot noise reduction in Fig.6-1, provided high enough RF frequencies are considered, for which quantum noise dominates over the excess classical noise of the background laser light.

### 6.1.3 Guided Acoustic Wave Brillouin Scattering

We close this section by mentioning a very important source of noise for fiber squeezers. Fibers have a family of acoustical modes corresponding to radial vibrations of the waveguide. The lowest frequency of these modes depends predominantly on the fiber radius, and is typically around $20MHz$. Due to their low frequencies, these modes are thermally excited and produce noisy "refractive index ripples" on the fiber core. The guided optical field couples to these modes until their frequencies are so high and the ripples on the core so closely spaced that their net effect cancels. The scattering of the pulse by this process is called guided acoustic wave Brillouin scattering (GAWBS) [115, 116, 117]. The exact frequency at which the coupling cuts off depends on the core size, and is typically $1GHZ$. For most fiber experiments, light scattered forward by this mechanism is too small to be of concern. In fiber squeezing however, this scattered light raises the noise floor of the balanced photocurrent and can prevent any measurement of squeezing. Historically, GAWBS has been the most important obstacle to fiber squeezing. A number of techniques were however developed successfully to circumvent this effect and to produce significant and usable degrees of squeezing. Whereas SPM squeezers are affected by polarized GAWBS (scattering $x$-polarized light back into the $x$-polarized modes), the polarization XPM scheme proposed above will be affected by depolarized GAWBS (scattering $x$-polarized light into the $y$-polarized modes). This is unfortunate since the frequency spacing of these modes is somewhat irregular and leads to GAWBS sidebands occurring at much lower frequencies in the balanced homodyne photocurrent. Suppose for example that the input pulse train has an envelope

$$A_i(\tau) = \sum_n A_n e^{-i\Omega_0 n\tau} \tag{6.17}$$

where $\Omega_0/2\pi$ is the repetition rate of the pulse stream. Neglecting damping of the acoustic modes for simplicity, the output field has the form

$$A_o(\tau) = \sum_n A_n e^{-i\Omega_0 n\tau} \times \sum_m a_m e^{-i\nu_m \tau}, \tag{6.18}$$

where $a_m$ are scattering coefficients and $\nu_m$ are the acoustic mode frequencies. This expression shows that each frequency component of the field picks up sidebands at the acoustical frequencies. As discussed, the lowest frequency is about $20MHz$ and the coefficients $a_m$ vanish for frequencies superior to about $1GHz$. The output intensity is obtained by squaring the field

$$|A_o(\tau)|^2 = \sum_q |B_q|^2 e^{-i\Omega_0 q\tau} \times \left( \sum_{m,m'} a_m a_{m'}^* e^{-i(\nu_m - \nu_{m'})\tau} \right). \tag{6.19}$$

In this expression $q = n - n'$ and $|B_q|^2$ are numerical coefficients related to the $A_n$. Hence the power spectrum of the output pulse is also made of a series of harmonics of the repetition rate. The noise sidebands for the harmonics of this quantity occurs however at the *difference frequencies* of the acoustical modes. Polarized GAWBS modes are evenly spaced so that these sidebands extend from $20MHz$ to $1GHz$ away from each harmonic. For depolarized GAWBS however difference frequencies as low as $1.5MHz$ and $2.5MHz$ occur [115]. This smaller frequency spread can make the high repetition rate method of GAWBS "suppression" difficult to implement for XPM squeezing[33]. Note that in practice, each mode is damped, resulting in noise linewidths of a few hundred $kHz$. These linewidths are typically below $200kHz$ when the protective plastic coating of the fiber is stripped. This is to be expected since this jacket dampens vibrations at the circumference of the fiber.

## 6.2 Depolarization from Quantum Noise

We have shown in Section 6.1 that a linearly polarized pump propagating in a low birefringence fiber modifies the vacuum fluctuations of the modes polarized perpen-

dicularly. In the present section, we show that these fluctuations affect, in turn, the evolution of the pump and lead to a depolarization of the latter. We predict a power dependent depolarization of the pump, increasing quadratically with the square of the fiber length.

### 6.2.1 Physical Origin of the Nonlinear Depolarization

The physical origin of depolarization in isotropic fibers can again be understood in terms of nonlinear polarization rotation. As figure 6-2 indicates, the projection on the $x$ axis of the polarization ellipses varies as the latter precesses due to the nonlinearity. Hence, energy is transfered from the $x$ to the $y$ polarization, When the $y$ modes are driven by a source of noise with an arbitrary phase relative to the pump, this transfer is irreversible. A steady state is eventually reached where both polarizations carry half of the input energy.

The above picture indicates that almost any source of noise driving the modes polarized perpendicularly to the pump in the input plane will lead to a depolarization of the latter. These fluctuations can be of classical or quantum origin. In practice, the cross-polarized modes are always excited by some residual light that cannot be totally eliminated with a polarizer. Extinction ratios of $10^{-4} - 10^{-5}$ are typical of very good polarizers. This background light is affected by classical noise expressed as a fraction of the average power. Depending on the laser used, this fraction can be between 0.1% and 5%. The origin of $y$-polarized residual light is twofold. First, some cross-polarized light is generated in the laser itself by amplified spontaneous emission (ASE). This portion of the background is not pulsed because the nonlinear modelocking mechanism does not affect small power levels. For this reason, nonlinear depolarization by ASE noise is very weak and can be neglected. The second source of $y$-polarized light is polarization cross-talk in optical elements of the laser and of the fiber coupler. A perfectly polarized pulse propagating in these elements will be slightly depolarized due to the small birefringence created by stress, strain or manufacturing imperfections. This mechanism provides a pulsed $y$-polarized background which can act very efficiently to depolarize the pulse in the fiber. The discussion below focusses

however exclusively on the depolarization induced by quantum noise, which is the main theme of this thesis. Contrary to the noise sources discussed above, quantum noise cannot be eliminated, even in principle. For this reason, it provides an ultimate limit for the distance over which a linearly polarized pulse of large intensity can be propagated in a low birefringence fiber. It is interesting to note that no such limit arises for circularly polarized pulses. The latter constitute true propagation eigenmodes of the fiber. Although depolarization from quantum noise is small in most situations, it can lead to measurable effects for pulses with peak powers of the order of $10MW$. The coupling of such pulses in an optical fiber was recently reported in [118] and stimulated my interest in their quantum propagation. Chen *et al.*[119] recently reported the power-dependent depolarization of a linearly polarized wave in non birefringent fibers. These authors attributed this phenomenon to imperfections in the manufacturing process of their fiber. This type of depolarization, which is strongly dependent on the fiber itself, has a *linear* dependence on the propagation distance. It can therefore be distinguished from the quadratic dependence of the depolarization predicted here. The effect discussed below affects all fibers in the same way and cannot be avoided by careful manufacturing. It is closely related to the depolarization effect discussed by Matera, Mecozzi and Settembre[124] for pulses propagating in long-haul communication links. In this case however, the pump depolarization is caused by ASE noise produced by amplifiers inserted along the fiber link. In the present work, depolarization arises from the quantization of the electromagnetic field itself.

### 6.2.2 Field Equations

In Fig. 6-2, the change in the projection of the polarization ellipses on the $y$ axis is a first order effect in the rotation angle. This is why polarization XPM squeezing can be described by the linearized theory. The change in the projection of the field on the $x$ axis is however a second order effect and cannot be obtained within this theory. This is obvious from equation (6.5) which implies that the pump is unaffected by noise. We therefore return to the non-linearized equations (6.1) and (6.2), where we replace the classical envelopes by the field operators $\hat{A}_x$, $\hat{A}_y$, $\hat{A}_x^\dagger$ and $\hat{A}_y^\dagger$. These equations are

best analyzed using circularly polarized fields

$$\hat{C}_{\pm}(z,\tau) = \frac{\hat{A}_x(z,\tau) \pm i\hat{A}_y(z,\tau)}{\sqrt{2}}. \tag{6.20}$$

These fields obey the commutation relations

$$\left[\hat{C}_{\pm}(z,\tau), \hat{C}^{\dagger}_{\pm}(z,\tau')\right] = \delta(\tau - \tau'). \tag{6.21}$$

All other commutators between these variables vanish. Expressing equations (6.1) and (6.2) in terms of the circular fields, we find

$$\frac{\partial \hat{C}_{\pm}(z,\tau)}{\partial z} = \left(D + i\hat{N}_{\pm}(z,\tau)\right)\hat{C}_{\pm}(z,\tau), \tag{6.22}$$

where the nonlinear operators in the circular basis are

$$\hat{N}_{\pm}(z,\tau) = \frac{2\kappa}{3}\left(\hat{C}^{\dagger}_{\pm}\hat{C}_{\pm} + 2\hat{C}^{\dagger}_{\mp}\hat{C}_{\mp}\right). \tag{6.23}$$

Note that no coherence term appears in the circular polarization basis.

We restrict the following analysis to the zero dispersion case, $D = 0$, where the nonlinear field equations can, once more, be integrated in closed-form. We shall use the discretized-time model (Section 4.2.2) which allows to evaluate the first order correction to the linearized theory (see Section 4.3). We discretize the time coordinate in intervals of duration $\Delta\tau \simeq 1fs$, and we replace the quantum fields by a sum of independent variables defined on these intervals. For example, we have

$$\hat{C}_{\pm}(z,\tau) = \frac{1}{\sqrt{\Delta\tau}}\hat{c}_{\pm,n}(z), \tag{6.24}$$

for $\tau$ between $n\Delta\tau$ and $(n+1)\Delta\tau$. The time-slot operators obey the commutation relations

$$\left[\hat{c}_{i,n}, \hat{c}^{\dagger}_{j,m}\right] = \delta_{i,j}\delta_{n,m}, \tag{6.25}$$

with $i,j = +,-$. All other commutators involving the $\hat{c}$ and $\hat{c}^\dagger$ variables vanish. Expressing the field equations in terms on the discretized variables, we find ($D = 0$)

$$\frac{\partial \hat{c}_{\pm,n}(z)}{\partial z} = i\hat{N}_{\pm,n}(z)\hat{c}_{\pm,n}(z),. \tag{6.26}$$

where $\hat{N}_{\pm,n}(z)$, which equals $\hat{N}_{\pm}(z,\tau)$ for $\tau$ between $n\Delta\tau$ and $(n+1)\Delta\tau$, is given by

$$\hat{N}_{\pm,n}(z) = \hat{N}_{\pm}(z,\tau) = \frac{2\kappa}{3\Delta\tau}\left\{\hat{c}^\dagger_{\pm,n}\hat{c}_{\pm,n} + 2\hat{c}^\dagger_{\mp,n}\hat{c}_{\mp,n}\right\}. \tag{6.27}$$

One verifies from these equations that the operators $\hat{c}^\dagger_{\pm,n}\hat{c}_{\pm,n}$ are constants of motion. The number of photons with a given helicity in each time interval is therefore unaffected by the propagation. Replacing $\hat{N}_{\pm,n}(z)$ by $\hat{N}_{\pm,n}(0)$ in (6.26), this equation is readily integrated

$$\hat{c}_{\pm,n}(z) = \exp\left(i\hat{N}_{\pm,n}(0)z\right)\hat{c}_{\pm,n}(0) \tag{6.28}$$

Reverting to the linearly polarized envelopes, we find

$$\begin{pmatrix} \hat{A}_x(z,\tau) \\ \hat{A}_y(z,\tau) \end{pmatrix} = \frac{1}{2}\left\{ e^{i\hat{N}_{+,n}(0)z}\begin{pmatrix} 1 & i \\ -i & 1 \end{pmatrix} + e^{i\hat{N}_{-,n}(0)z}\begin{pmatrix} 1 & -i \\ i & 1 \end{pmatrix}\right\}\begin{pmatrix} \hat{A}_x(0,\tau) \\ \hat{A}_y(0,\tau) \end{pmatrix}, \tag{6.29}$$

where $n = \tau/\Delta\tau$. Contrary to the excitation number of the circular fields which are constants, the photon number operators for the linear polarizations, $\hat{A}^\dagger_x\hat{A}_x$ and $\hat{A}^\dagger_y\hat{A}_y$, are not preserved individually during the evolution of the fields. This reflects the fact that the phase between the circular fields varies, leading to a rotation of the polarization ellipse. Classically, the nonlinear rotation rate of a linearly polarized wave vanishes. Hence, the classical equations predict that a linearly polarized pulse preserves its polarization state as it propagates in a non-birefringent fiber. Equation (6.29) tells a different story however.

We will assume that $\hat{A}_x(0,\tau)$ is in a coherent state with input profile $\alpha(\tau)$, and that $\hat{A}_y(0,\tau)$ is in vacuum. We therefore have

$$\hat{A}_x(0,\tau)\,|in\rangle \;=\; \alpha(\tau)\,|in\rangle \tag{6.30}$$

$$\hat{A}_y(0,\tau)\,|in\rangle = 0 \tag{6.31}$$

$$\hat{c}_{\pm,n}(0)\,|in\rangle = \sqrt{\frac{\Delta\tau}{2}}\alpha(\tau)\,|in\rangle\,. \tag{6.32}$$

Clearly, in the input plane, the $y$-polarized photon flux vanishes. This photon flux in the output plane is given by

$$\begin{aligned}
\left\langle \hat{A}_y^\dagger(z,\tau)\hat{A}_y(z,\tau)\right\rangle &= \frac{|\alpha(\tau)|^2}{4}\left\langle \left(e^{-i\hat{N}_+(0)z} - e^{-i\hat{N}_-(0)z}\right)\left(e^{i\hat{N}_+(0)z} - e^{i\hat{N}_-(0)z}\right)\right\rangle \\
&= \frac{|\alpha(\tau)|^2}{2}\left\{1 - \mathrm{Re}\left\langle e^{-i\hat{N}_+(0)z}e^{i\hat{N}_-(0)z}\right\rangle\right\} \\
&= \frac{|\alpha(\tau)|^2}{2}\left\{1 - \mathrm{Re}\left\langle e^{\frac{2i\kappa z}{3\Delta\tau}}\hat{c}_+^\dagger(0)\hat{c}_+(0)\right\rangle\left\langle e^{-\frac{2i\kappa z}{3\Delta\tau}}\hat{c}_-^\dagger(0)\hat{c}_-(0)\right\rangle\right\} \\
&= \frac{|\alpha(\tau)|^2}{2}\left\{1 - \exp\left[-2\Delta\tau\,|\alpha(\tau)|^2\sin^2\left(\frac{\kappa z}{3\Delta\tau}\right)\right]\right\},
\end{aligned} \tag{6.33}$$

where in the last step we used formula (C.2)

$$\langle in|\exp\left(i\epsilon\hat{c}_{\pm,n}^\dagger\hat{c}_{\pm,n}\right)|in\rangle = \exp\left(\frac{\Delta\tau\,|\alpha(\tau)|^2}{2}(e^{i\epsilon}-1)\right). \tag{6.34}$$

The same calculation for the $x$-polarized photon flux gives

$$\left\langle \hat{A}_x^\dagger(z,\tau)\hat{A}_x(z,\tau)\right\rangle = \frac{|\alpha(\tau)|^2}{2}\left\{1 + \exp\left[-2\Delta\tau\,|\alpha(\tau)|^2\sin^2\left(\frac{\kappa z}{3\Delta\tau}\right)\right]\right\}, \tag{6.35}$$

so that the overall photon flux is a constant at any point across the pulse.

Expressions (6.34) and (6.35) display a spatial periodicity of period $z_{revival} = 3\pi\Delta\tau/\kappa$ characteristic of the discretized-time model. As pointed out in Section 4.2, these revivals are an artifact of the discretization procedure and disappear in the continuous-time model. In fact, only the first term of the expansion of the $\sin^2$ function is meaningful. The $x$ and $y$ average optical powers are therefore

$$P_{x,y}(z,\tau) = \frac{P_x(0,\tau)}{2}\left\{1 \pm \exp\left(-\frac{2P_x(0,\tau)(\kappa z)^2}{9\Delta\tau\hbar\omega_0}\right)\right\}. \tag{6.36}$$

As announced, the depolarization for any given time slot increases linearly with the power of the pump and quadratically with the propagation distance.

It is important to emphasize that the transfer of photons from the $x$ to the $y$ polarization is incoherent. This can be seen by computing the degree of polarization for any time slot[120]

$$d(z,\tau) \equiv \frac{1}{\langle \hat{s}_0(z,\tau)\rangle}\sqrt{\sum_{k=1}^{3}\langle \hat{s}_k(z,\tau)\rangle^2}. \tag{6.37}$$

In this expression, we introduced the Hermitean Stokes operators defined by

$$\hat{s}_0(z,\tau) = \hat{c}^\dagger_{+,n}\hat{c}_{+,n} + \hat{c}^\dagger_{-,n}\hat{c}_{-,n}, \tag{6.38}$$

$$\hat{s}_1(z,\tau) = \hat{c}^\dagger_{+,n}\hat{c}_{-,n} + \hat{c}^\dagger_{-,n}\hat{c}_{+,n}, \tag{6.39}$$

$$\hat{s}_2(z,\tau) = i\left(\hat{c}^\dagger_{+,n}\hat{c}_{-,n} - \hat{c}^\dagger_{-}\hat{c}_{+,n}\right), \tag{6.40}$$

$$\hat{s}_3(z,\tau) = \hat{c}^\dagger_{+,n}\hat{c}_{+,n} - \hat{c}^\dagger_{-,n}\hat{c}_{-,n}. \tag{6.41}$$

where $n = \tau/\Delta\tau$. The function $d$ takes values between 0 and 1. When the phase between the $x$ and $y$ components is perfectly defined, the field is elliptically polarized and $d = 1$. For any other situation, $d$ is less than unity. In the limit where the relative phase between the linear polarization states is perfectly randomized, $d = 0$. The function $d(z)$ is easily computed for our field by using the fact that $\hat{s}_0$ and $\hat{s}_3$ are constants of motion. For an initial linearly polarized wave, both circularly polarized modes are equally excited and we find $\langle \hat{s}_3(z)\rangle = 0$. One also verifies, using (6.28) and (6.32) that the expectation value of $\hat{s}_2(z,\tau)$ vanishes. Putting everything together, we find

$$d(z,\tau) = \frac{\langle \hat{s}_1(z,\tau)\rangle}{\langle \hat{s}_0(0,\tau)\rangle} = \exp\left(-\frac{2P_x(0,\tau)(\kappa z)^2}{9\Delta\tau\hbar\omega_0}\right). \tag{6.42}$$

This expression indicates that the center of the pulse depolarizes faster than its wings. This makes nonlinear depolarization hard to compensate since the polarization of the field varies on the time scale of the pulse. The length scale over which nonlinear depolarization from quantum noise becomes important is determined by the peak power of the pulse

$$z_D = \frac{3}{\kappa}\sqrt{\frac{\Delta\hbar\omega_0\tau}{2P_x(0,0)}}, \tag{6.43}$$

We compute $z_D$ in two cases. The first one corresponds to the experimental conditions reported by Chen *et al.* in their analysis of depolarization from manufacturing imperfections [119]. These authors used pulses with a peak power of about $6kW$, corresponding to $z_D \simeq 680m$. It is clear from this number that quantum depolarization was not the effect measured in [119] since in this experiment, the fiber was only $1m$ long. On the other hand consider the experiment recently reported by Lenz *et al.*[118]. In this experiment, pulses from a stretched-pulse fiber laser were post amplified with a KCl:$TI^+$ color center crystal amplifier. At the output of the amplifier, 200fs pulses with a peak intensity of about $10MW$ were measured. This very high peak power yields a depolarization length of 16 $m$. Since the residual beat length of low birefringence fibers is of the order of $30m$ to 50 $m$, the depolarization process discussed in this section could be detected in this case.

# Chapter 7

# Experimental Work

As part of this thesis, a Sagnac fiber squeezer, a modelocked titanium-sapphire laser and a balanced homodyne detector were built. The squeezer based on a self-stabilized design, operates at $830nm$ in the positive dispersion regime, and with very short pulses. Although we were not yet successful in measuring squeezing with this system, progress in this project is summarized here.

## 7.1 Balanced Homodyne Detector

A schematic of the electronic circuit of the detector is given on Fig 7-1 [121]. The leads of two backbiased silicon p-i-n photodiodes are connected so that their photocurrents subtract. The resulting difference photocurrent is converted into an output voltage $V_o$ using a transimpedance preamplifier stage. The choice of the photodiodes and of the op-amp was based on their noise properties. Consider for example the noise circuit of Fig. 7-2 which provides a simple model for the noise properties of each photodiode. The shunt resistance $R_D$ in backbiased junctions is typically very large ($> 1MHz$) and can therefore be neglected in the circuit. The capacitance $C_D$ depends on the backbias voltage $V_{BB}$ and on the area of the photodiodes. In our case, $V_{BB} = 45V$ for which $C_D \simeq 6pF$. The shot noise source arises from the quantization of the

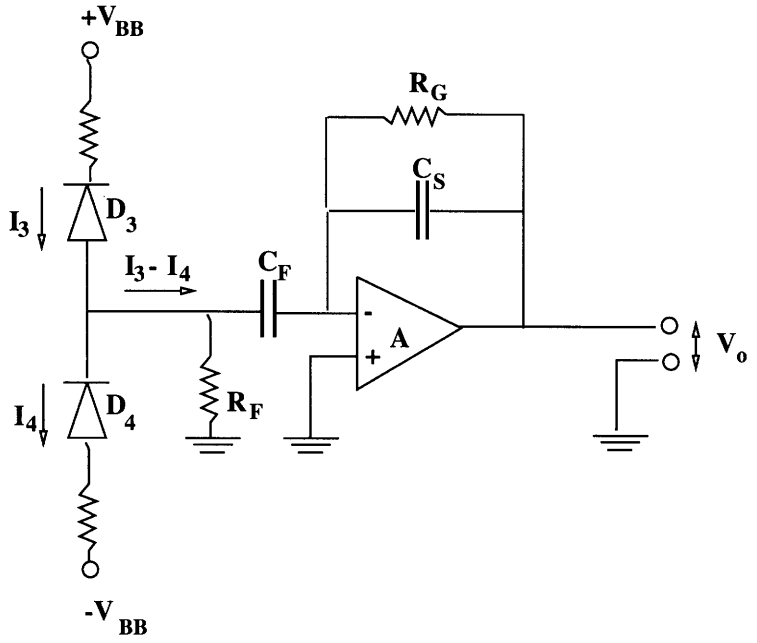


Figure 7-1: Electronic circuit of the balanced homodyne detector. $D_3$ and $D_4$ are EG+G C30808E PIN photodiodes. $A$ is an OP-27 op-amp. $R_G = 10k\Omega$, $C_S \simeq 1pF$, $R_F = 1k\Omega$ and $C_F = 1\mu F$.

electromagnetic field exciting the diodes, and provides a spectral noise density

$$I_{\text{shot}} = \sqrt{2e\bar{I}}, \tag{7.1}$$

where $e = 1.6 \times 10^{-19}C$ is the electric charge of an electron and $\bar{I}$ is the average photocurrent generated at each photodiode. Typically, $\bar{I} \simeq 10mA$, so that $I_{\text{shot}} \simeq 57pA/\sqrt{Hz}$. In squeezing experiments, the shot noise spectral density can be considered as the signal that one attempts to measure against the noise background provided by dark currents and amplifier noise. Dark currents arise when electron-hole pairs are spontaneously generated in the junction without a photon excitation. Dark currents flow through the feedback resistor of the amplifier and therefore experience the same gain as shot noise. The magnitude of these background counts increases with the surface of the diode, which should be kept small. The EG&G diode used in our circuit has a $5mm^2$ active area, leading to a dark current spectral noise density of $0.14pA/\sqrt{Hz}$. The excess noise in Fig 7-2 arises from the classical fluctuations of the

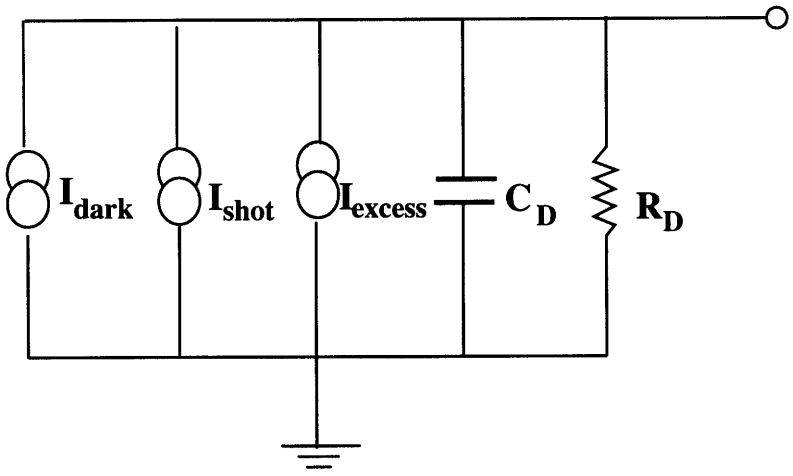


Figure 7-2: Noise model for the photodiodes.

laser. Contrary to the dark counts which occur independently at each detector, the excess noise at the two detectors is perfectly correlated and is therefore canceled in the subtraction process. In actual detectors, excess noise cannot be canceled perfectly due to the slightly different responses of the photodiodes. Excess noise therefore contributes to background noise in the balanced detection process. Since the contribution $I_{\text{excess}}$ grows linearly with $\bar{I}$, it dominates over shot noise at high enough intensities, the latter increasing only as $\sqrt{\bar{I}}$. Shot noise is however a white noise source, leading to a flat spectral noise density. Excess laser noise on the other hand rolls off beyond a few hundred kilohertz. Hence, by monitoring the output voltage $V_o$ at high enough frequencies, the excess laser noise can be made insignificant. The detector built in this thesis displayed a shot noise limited spectral density beyond about $400kHz$ for an average photocurrent of about $10mA$ per diode. The light source was a modelocked Ti:Sapphire laser pumped with an argon laser. This system is notoriously noisy due to the argon pump. Laser noise cancellation in excess of $35dB$ was observed.

The noise of the op-amp on the other hand can be modeled by the circuit of Fig. 7-3, and includes both a voltage and a current noise source. The current noise here is

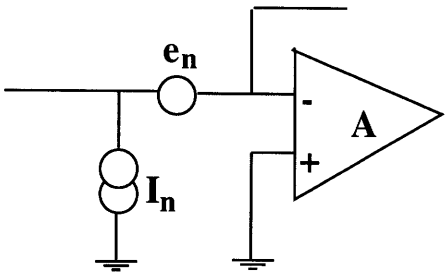


Figure 7-3: Noise model for an op-amp. $e_n$ is a voltage noise source and $I_n$ is a current noise source.

the shot noise corresponding to the input bias current $I_b$ and has a spectral density $\sqrt{2eI_b}$. One should therefore use an op-amp with a low bias current. In the case of the OP-27 used in our detector, $I_n$ was $0.4pA/\sqrt{Hz}$ for frequencies above $1kHz$, which is negligible compared to shot noise. The input voltage noise of the op-amp, which is generally of thermal origin, is one of the most important design parameter. In order to affect the voltage $V_o$, $e_n$ must generate a current flowing into the photodiode impedances. At low frequencies, the latter is dominated by the very large shunt resistance, so that the voltage gain, $1 + \frac{R_G}{R_D}$ where $R_G \simeq 10k\Omega$, is negligible. The capacitance $C_D$ of the diode alters the feedback at higher frequencies, leading to a significant gain for $e_n$. In fact, both $I_n$ and $e_n$ can be combined into a single frequency dependent amplifier current noise source [121]

$$I^2_{\text{amp}} \simeq I_n^2 + 4e_n^2\omega^2C_D^2, \tag{7.2}$$

where $R_D$ was neglected. The voltage noise is more than $10dB$ below shot noise when $I^2_{\text{amp}} < 0.2I^2_{\text{shot}}$. ( The extra factor 2 comes from the fact that the shot noise of

the two photodiodes add incoherently.) From the above condition and from (7.1), we find that shot noise dominates the amplifier noise for RF frequencies smaller than

$$\nu_0 \equiv \frac{\sqrt{0.4e\bar{\bar{I}}}}{4\pi e_n C_D}. \tag{7.3}$$

For the OP-27 used in our circuit, we have $e_n = 3nV/\sqrt{Hz}$, leading to $\nu_0 \simeq 38MHz$. This value is well beyond the open-loop gain bandwidth of the amplifier which is $8MHz$.

The bandwidth of the balanced detector is set by the open-loop gain bandwidth and by the shunt capacitance $C_s$. Stray capacitance typically contribute $1pF$ to $C_s$. The detector built around the OP-27 has a bandwidth of about $1.5MHz$. In principle, a wider bandwidth could be achieved with the OP-37 since this component has an open-loop bandwidth of $63MHz$. We however encountered gain peaking noise with this op-amp, and the shunt capacitance had to be increased to about $30pF$, reducing the bandwidth of the detector back to about $2MHz$.

## 7.2 Modelocked Titanium-Sapphire Laser

Most of the problem associated with guided acoustic wave Brillouin scattering (Section 6.1.3) can be eliminated by using a laser with a repetition rate superior to the GAWBS cut off frequency. In this case, the frequency range of the sidebands associated with each harmonic in (6.19) do not overlap, and GAWBS noise is confined to narrow peaks. Squeezing can be observed between these peaks. The feasibility of this approach was demonstrated experimentally by Bergman[33] at zero-dispersion. In order to carry out the same program at $830nm$, a modelocked titanium-sapphire laser with a high repetition rate was constructed. A modelocked bandwidth of about $3.1nm$ was observed for time intervals of about 5 minutes with $190mW$ of output power and a repetition rate of $700MHz$. Due to the unstable nature of our system, auto-correlation of the pulses was not attempted. A transform-limited pulse with the above bandwidth would however have a duration of $240fs$. The laser could not be

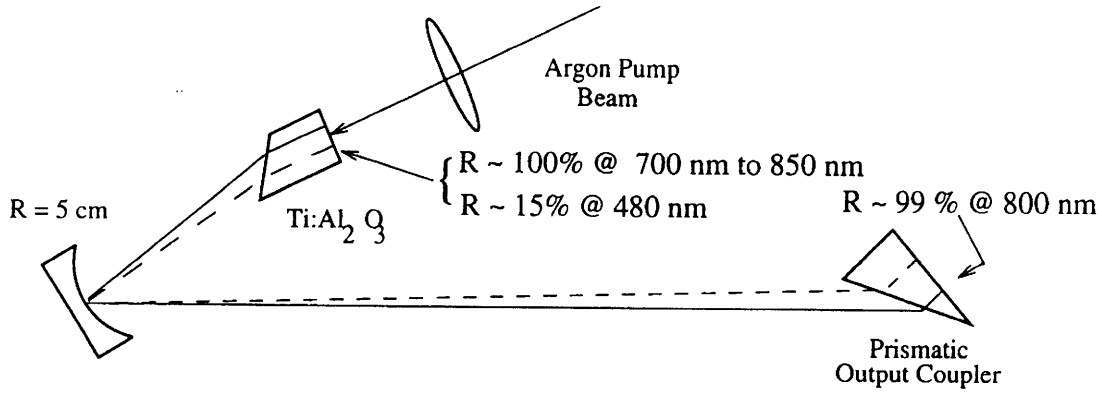


Figure 7-4: PRF High repetition rate titanium-sapphire laser(After Ref.[123]).

stabilized by changing the alignment of the optical components. The laser clearly needs a few modifications in order to become a useful tool. These modifications are not however of a fundamental nature since a similar system is operated very successfully by Bret Bouma at MIT. Spectral bandwidths around $7nm$, and output powers around $500mW$ were achieved with his system. The source of instability in my system is identified below.

A schematic of the laser is shown on Fig. 7-4, is based on the Payé-Ramaswamy-Fujimoto (PRF) design[122]. When the system is modelocked, a single pulse circulates between the mirrors and produces a periodic output each time it bounces on the partially transmitting output coupler. The repetition rate of the laser is inversely proportional to the cavity length. To achieve repetition rates around $1GHz$, cavity lengths of about $20cm$ must be used. To produce femtosecond pulses with Ti:Sapphire, one must compensate the positive dispersion acquired by the pulse in the gain medium by negative dispersion somewhere else in the cavity. In most lasers, a pair of prisms is introduced for that purpose in the cavity, resulting in repetition rates around $80MHz$. In the PRF laser, the prism are incorporated directly into

the gain medium and the output coupler, reducing considerably the cavity length. Repetition rates in excess of $1GHz$ can therefore be achieved with highly dispersive output couplers.

The pulse generating mechanism of our laser is Kerr-lens modelocking (KLM)[56]. In this approach, high intensities are encouraged in the cavity by maximizing the overlap of the corresponding field with the argon pump. The transverse extension of the modes in the cavity is modified at high intensities by self-focussing in the laser gain medium. The latter becomes equivalent to a linear gain medium in series with a lens having a radius of curvature increasing with intensity. Due to the weak Kerr effect, the action of the nonlinear lens requires long distances to produce a significant effect. For this reason, KLM is harder to implement in our short cavity, and larger intensities are required to reach stable operation.

The most important problem encountered with our laser is related to the coating on the gain medium. This stack of quarter-wave dielectric layers was designed to be highly reflective between 750nm and 950nm, and to be highly transmissive at the argon pump wavelength (480nm-515nm). The focal point of the pump and of the lasing mode occur almost on this coating which is therefore exposed to considerable optical power. Although the coating was designed to sustain these powers, it invariably burned when the pump exceeded $3W$ or when the laser was modelocked for more than 5 minutes with a $2.75W$ pump. Each time the coating burned, the cavity had to be realigned. The pump powers allowed by the coating were probably too low to achieve stable modelocking. The reasons for the poor performance of the coating are not clear since a similar coating is used in Bret Bouma's laser. It can be due to a manufacturing imperfection, to the trapping of dust particles in the argon beam, or to the formation of condensation on the crystal. In addition to the coating problem, the system stability would clearly benefit from better mounts and from enclosing the argon pump to shelter it from air currents.

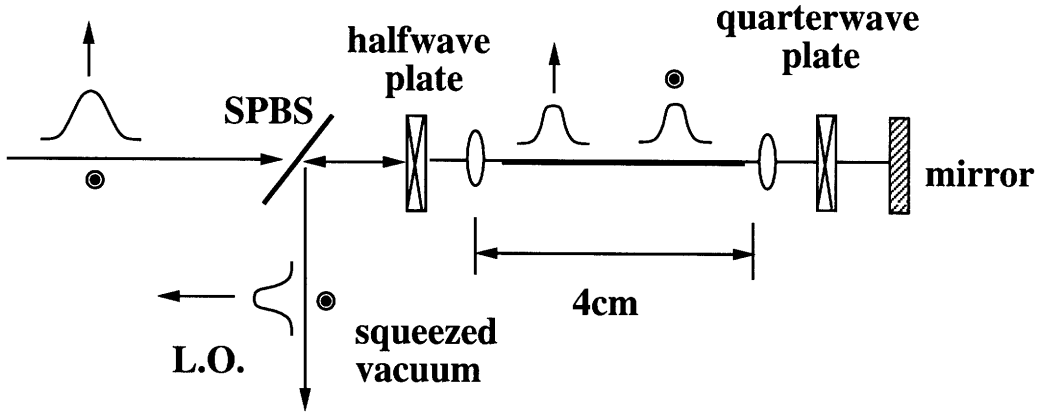


Figure 7-5: Self-stabilized Sagnac fiber squeezer.

## 7.3 Self-Stabilized Sagnac Squeezer

In the absence of a high repetition rate laser to "suppress" GAWBS noise, a different approach using short fibers was investigated. GAWBS noise decreases with fiber length and can eventually be reduced below shot noise. In addition, when the fiber is very short, GAWBS noise can drop off completely. As we mentioned previously, GAWBS imbalances the Sagnac interferometer by changing the index seen by the counterpropagating pulses, resulting in a non-reciprocal transfer matrix for the system. The frequency cut off for this process is about $1GHz$, so that during one high frequency GAWBS cycle, the pulse travels over $20cm$ in the silica fiber. Fiber loops much shorter than this length will not be imbalanced by GAWBS noise. In practice it is very hard to form a $5cm$-long fiber loop, and for this reason a different geometry must be used for the interferometer. Consider the set up of Fig.7-5. A linearly polarized pulse is coupled into a polarization maintaining fiber at $45^0$ with respect to its birefringence axis. Due to the high birefringence of the fiber, the pulse breaks into two orthogonally polarized pulses traveling through the fiber at different group velocities. At the fiber end, one uses a quarterwave plate and a mirror to exchange

the polarization states of the two pulses, which are coupled back into the fiber. On their way back, the slow pulse becomes the fast one, and *vice versa.* These pulses combine at the entrance of the fiber, where they interfere to form a linear polarization state identical to the input pulse. The incoherent squeezed fluctuations traveling with the pulses do not interfere however and produce a squeezed vacuum polarized perpendicularly to the pulse. This squeezed light is separated using a special polarization sensitive beamsplitter which also deflects part of the pump that is used as a local oscillator[35].

This device clearly behaves like a Sagnac interferometer and allows to separate the squeezed vacuum from the pump. The returning beams being spatially mode matched to the fiber propagating mode, the destructive interference in the squeezed port is very efficient, thus reducing the laser background in this port. The linear geometry of the interferometer affords the use of very short fibers. Our implementation of this device revealed however two shortcomings. The first one is related to losses occurring at the fiber end with a quarterwave plate. Although one attempts to couple back a beam perfectly matched to the fiber, we found that in practice coupling efficiency beyond 75% were very difficult to achieve. This 25% loss combined with additional losses in the rest of the system reduce considerably the squeezing that can be achieved. The other drawback of the above system arises from the narrow bandwidth of the zeroth order waveplates (CVI QW0 series). As a result, the energy of the pulse frequency components extending beyond $\pm 4nm$ of the carrier does not interfere properly at the fiber input and is mostly directed into the squeezed port. We found that when the bandwidth of the pulse was larger than about $6nm$, the energy scattered into the squeezed port prevented observation of squeezing due to the large classical noise background. We confirmed our diagnostic by looking at the power spectrum of the background light in the squeezed port. This spectrum showed a symmetric double-hump structure with a dip at the carrier frequency and humps at $\pm 5nm$. As the pulse bandwidth is increased, the humps extend further out and contain more energy, whereas the power spectrum density in the dip is constant. When the frequency of the laser is tuned without adjusting the setting of the waveplates, the spectrum becomes

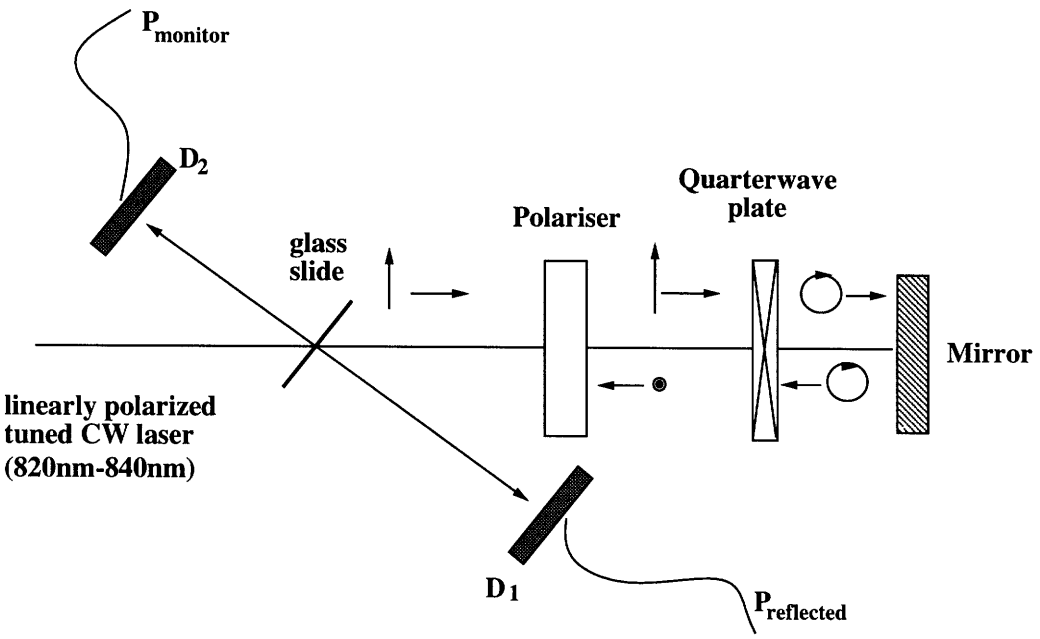


Figure 7-6: Set-up for the bandwidth measurement of the waveplates.

asymmetric, with one of the humps growing and the other one shrinking. Once again, the height of the dip stays constant. The bandwidth of the quarterwave plate was also measured independently using the set-up of Fig.7-6 which is somewhat similar to the use made of this waveplate in the squeezer. The Ti:sapphire laser was operated CW for these measurements, and its wavelength was tuned from $820nm$ to $840nm$. For a perfect quarterwave plate, the linear input polarization is rotated by $90^0$ on its way back to the polarizer. Hence, for an ideal waveplate, no light should be reflected on the glass slide and $P_{\text{reflected}} = 0$. In practice, some light is always detected by $D_1$. As the wavelength of the laser is tuned, the action of the quarterwave plate becomes less and less ideal and more light is reflected back to $D_1$. The photodetector $D_2$ is used to monitor and compensate for the change in input intensity for different wavelengths. By monitoring $P_{\text{reflected}}(\lambda)/P_{\text{monitor}}(\lambda)$, the bandwidth of the waveplate can be determined to be $\pm 4nm$.

# Chapter 8

# Summary and Future Research

In this thesis, we presented a theoretical framework within which fiber squeezing could be described and predicted. The aim of this work was to provide a tool in the design of better fiber squeezers. Special attention was paid to femtosecond pulses and to dispersive fibers. We developed a theory of quantum noise incorporating the finite response time of the Kerr effect and the associated Raman noise (Sections 3.2 and 4.1). We showed how the spectral properties of the response function and of Raman noise were related, and could be determined experimentally from Raman gain measurements (Section 4.1.2). The validity of the linearized theory was tested using both the zero-dispersion limit (Section 4.3) and the soliton regime (Section 5.3). We concluded that for almost any conceivable squeezing experiment, this approximation provided a faithful description of the quantum noise evolution. This is a very useful conclusion since in this simpler theory, the evolution of quantum noise can be thought of in classical terms. We showed for example in Section 3.3 how quantum propagation problems could be solved using Green's functions driven by the classical field.

As part of our investigation on the finite response time of the Kerr effect, we presented a fully nonlinear and self-consistent theory of pulse propagation in dispersionless fibers (Section 4.2). Although this situation is described by a simple classical equation, the straightforward quantization of the latter leads to a singular theory. We showed how the divergences of this theory were removed when the finite response time of the nonlinearity was incorporated. In this case, the high frequency zero

point fluctuations of the field can no longer create index changes in the fiber and thus do not affect the propagating pulse. Our treatment revealed the presence of a nonlinear Langevin noise source in the field equation. Such noise sources are fairly common in the description of systems interacting linearly with a heat bath. To our knowledge however, our treatment provides the first example of a fully characterized Langevin noise source arising from a nonlinear interaction. Our analysis suggests that all material-induced optical nonlinearities are accompanied by noise.

As a bonus, our treatment of dispersionless Raman active fibers lead to a closed-form solution of the field equation. This is somewhat unexpected as this equation is both integro-differential and stochastic. We took advantage of the availability of this solution to evaluate the mean field (Section 4.2.2) and the squeezing level (Section 4.2.3) of the field beyond the linearized approximation. We also probed the domain of validity of the discretized-time model. We showed that this theory predicts spurious quantum revivals and neglects Raman noise. It provides however a useful tool to monitor departures from the linearized theory when its time constant is chosen of the order of the electronic response time (Section 4.3). The discretized-time model is also self-consistent in the sense that the commutators of its dynamical variables are preserved. As such, it does not need a Raman noise source. We showed that even though Raman noise had observable effects in resonance-fluorescence (Section 4.2.1), its impact on fiber squeezing is rather modest.

In Chapter 5, we studied the Poisson-Gaussian soliton constructed as superposition of Bethe states. In addition to probing the limits of the linearized approximation in this case (Section 5.3), we considered the fluctuation levels of the four soliton operators. We showed that whereas coherent states cannot minimize these fluctuations, one can construct Poisson-Gaussian solitons for which the uncertainty on these variables is minimized (Section 5.4).

Our analysis of low birefringence fibers led to a new technique for the generation of squeezed vacuum (Section 6.1). This approach uses the parametric process responsible for nonlinear polarization rotation in these fibers. This effect, which is widely used today to modelock fiber lasers, should operate as well for fiber squeezers. The main

advantage of this technique is that it does not rely on an interferometric geometry to separate the squeezed vacuum from the pump. It therefore provides a potentially more rugged design. A second effect discussed in relation with low birefringence fibers is the nonlinear depolarization arising from the interaction of a linearly polarized pulse with the cross-polarized quantum noise (Section 6.2). Although this effect is weak for most situation, we argued that it could lead to measurable effects when pulses with peak powers in the megawatt range are considered.

The work presented in this thesis suggests many directions for further investigation of quantum noise in optical fibers. The most interesting opportunities are probably of an experimental nature. First, the enhancement in fiber squeezing at Ti:sapphire wavelengths is very promising. The technology of these oscillators is mature and very intense pulses can be generated with them. Unlike soliton squeezing where the peak power of the pulses is constrained by the dispersion of the fiber, positive dispersion squeezing can accommodate very intense pulses. The resulting squeezers can therefore be made very compact, thus reducing the effect of GAWBS. Positive dispersion squeezing was investigated experimentally as part of this thesis, but we were not yet successful at demonstrating shot noise reduction. The demonstration of appreciable degrees of squeezing at this wavelength would be very exciting.

So far, soliton squeezing experiments have led to disappointing results. It is not clear why these experiments fared so poorly. One hypothesis explains these results by the high noise level of the color-centered lasers that were used by both the MIT and IBM groups. In recent years, erbium-doped modelocked fiber lasers were developed to operate at $1.55\mu m$. As a gain medium, erbium is very quiet, particularly when pumped by a MOPA diode source. This arises from the slow response time of erbium ions which act as a low pass filter. A new experiment is under way at MIT to demonstrate soliton squeezing with this system. The outcome of this experiment will provide an important test to the soliton squeezing theory.

Fiber squeezers based on polarization XPM should be tested at zero dispersion or in the positive dispersion regime. Unless highly dispersive fibers are used, the weak power levels associated with solitons would require excessive fiber lengths in this case.

It is likely that the high repetition rate scheme used to localize GAWBS noise in the frequency domain will not be very helpful in this case unless a very quiet laser is used. Indeed, depolarized GAWBS produce noise sidebands within 1 or 2 MHz in the homodyne photocurrent spectrum (Section 6.1.3). A shot noise reduction window will occur below these sidebands only if the laser noise can be canceled at low enough frequencies.

The nonlinear depolarization of linearly polarized pulses is probably observable. In this thesis, we considered only the depolarization induced by quantum noise. This provides an upper bound on the distance over which an intense linearly polarized pulse can propagate in a low birefringence fiber. It is very likely however that the dominant depolarization process will have a classical origin. The pulsed component of the classical noise in particular probably acts very effectively at depolarizing the pulse because of its higher peak power. This contribution should be studied both theoretically and experimentally.

We showed in Section 4.3 that the response time of the electronic nonlinearity determines the length scale for the breakdown of the linearized theory at zero dispersion. The frequency dependence of the two-photon absorption spectrum of fused silica should therefore be used to determine the exact form of the electronic response function.

Theoretical avenues can also be pursued. Although self-consistent, the quantum theory of short pulse propagation developed in this thesis is far from complete. Short pulses are affected by self-steepening, which was not addressed at all here. As it turns out, Raman and self-steepening effects become important for pulses of roughly the same duration. As for the Raman effect, self-steepening terms do not preserve the commutators of the envelope and therefore require Langevin sources. Although we did not present these results, we found a family of nonlinear noise sources which can be used for that purpose. Unfortunately, a physical interpretation of these operators is still lacking.

On a more speculative note, quantized solitons have been investigated extensively by particle physics theorists as models for nuclear bound states. The availability of

a source of solitons made of bound photons is tantalizing and suggests that tests of the quantized soliton theory could be devised.

# Appendix A

# Reduction of squeezing by Losses

Losses can be model by the introduction of a beamsplitter in the path of a beam. This model allows one to evaluate the impact of losses on the amount of squeezing that can be achieved in actual systems. Suppose that the squeezed signal mode is described by the annihilation operator $\hat{a}_1$. Let $\hat{a}_4$ be the same signal after it experienced power losses of $1-\epsilon$. Using (2.31) with $t=\sqrt{\epsilon}$ and $r=\sqrt{1-\epsilon}$, we have

$$\hat{a}_4 = \sqrt{\epsilon}\hat{a}_1 - \sqrt{1-\epsilon}\hat{a}_2, \tag{A.1}$$

where the mode $\hat{a}_2$ is in vacuum. The noise reduction ratio for the quadratures of $\hat{a}_1$ and $\hat{a}_4$ are therefore related by

$$R_4 = \epsilon R_1 + 1 - \epsilon, \tag{A.2}$$

We see that if $\epsilon = 0.9$ and $R_1 = 0$ (infinite squeezing!), the noise reduction ratio increases to $R_4 = 0.1$ because of the losses, corresponding to $10dB$ of squeezing.

# Appendix B

# Quantization of the Electromagnetic Field in a Dispersive Single-Mode Fiber

In this Appendix, we review a number of results on the quantum theory of the electromagnetic field in dispersive single-mode fibers. Our presentation is inspired by [123]. We first remark that according to the Kramers-Krönig relations which enforce causality for dispersive media, a dispersive fiber must also be absorptive in some region of the spectrum. The assumption made in this thesis is that absorption is negligible over the narrow band of frequencies of interest. This approximation is excellent when considering fused silica fibers in the infrared wavelengths between 750nm and 1.8nm.

In the classical treatment of optical fibers, it is customary to use frequency to identify the propagating modes. This is a convenient choice since this parameter is controlled experimentally at the input of the waveguide by appropriate tuning of the laser source. This has led many authors to adopt a similar convention in their discussion of the quantum theory of optical waveguides. Quantum electrodynamics on the other hand usually uses the wavenumber to label the modes. This choice is natural when the initial state of the field is known and one seeks its final state. One can then decompose this initial field on the spatial eigenmodes and follow the time evolution of these modes. Within the slowly varying envelope, both approaches are

equivalent. In this Appendix we adopt the standard labeling convention of quantum electrodynamics and use the wavenumber to label the modes of the fiber. We indicate in the last paragraph of this Appendix how our approach relates to the frequency cnvention.

## B.1 Fiber Modes

Consider a mode of the fiber characterized by its wavenumber $\beta$. The electric and magnetic Hermitean field operators for this mode can be written

$$\hat{\mathbf{E}}(\mathbf{r},t,\beta) = \hat{\mathbf{E}}^{+}(\mathbf{r},t,\beta) + \hat{\mathbf{E}}^{-}(\mathbf{r},t,\beta) \tag{B.1}$$

$$\hat{\mathbf{H}}(\mathbf{r},t,\beta) = \hat{\mathbf{H}}^{+}(\mathbf{r},t,\beta) + \hat{\mathbf{H}}^{-}(\mathbf{r},t,\beta) \tag{B.2}$$

where the positive frequency parts are

$$\hat{\mathbf{E}}^{+}(\mathbf{r},t,\beta) = \mathbf{e}(x,y,\beta)\hat{a}(\beta,t)e^{i\beta z}, \tag{B.3}$$

$$\hat{\mathbf{H}}^{+}(\mathbf{r},t,\beta) = \mathbf{h}(x,y,\beta)\hat{a}(\beta,t)e^{i\beta z}, \tag{B.4}$$

and the "$-$" operators are the Hermitean conjugate of the "$+$" operators. In these expressions, we introduced the operator $\hat{a}(\beta,t)$ which creates photons in the mode $\beta$ at time $t$ and satisfies the equal-time commutation relations:

$$[\hat{a}(\beta,t),\hat{a}(\beta',t)] = 0 \;\; ; \;\; \left[\hat{a}(\beta,t),\hat{a}^{\dagger}(\beta',t)\right] = \delta(\beta-\beta'). \tag{B.5}$$

In the absence of nonlinearity, each annihilation operator evolves independently according to

$$\hat{a}(\beta,t) = \hat{a}(\beta,0)\exp(-i\omega(\beta)t). \tag{B.6}$$

The transverse mode profiles of the electric and magnetic fields, $\mathbf{e}$ and $\mathbf{h}$, satisfy Maxwell's equations where the $z$ and $t$ derivatives are replaced by $i\beta$ and $-i\omega$

respectively. Writing $\mathbf{e} = \mathbf{e}_t + e_z$ and $\mathbf{h} = \mathbf{h}_t + h_z$, we find

$$\begin{aligned}
\mathbf{e}_t &= -\left(\frac{\mu_0}{\epsilon_0}\right)^{1/2} \frac{c}{\omega n^2} \hat{\mathbf{z}} \times \{\beta \mathbf{h}_t + i \nabla_t h_z\}, \\
\mathbf{h}_t &= \left(\frac{\epsilon_0}{\mu_0}\right)^{1/2} \frac{c}{\omega} \hat{\mathbf{z}} \times \{\beta \mathbf{e}_t + i \nabla_t e_z\}, \\
e_z &= i \left(\frac{\mu_0}{\epsilon_0}\right)^{1/2} \frac{c}{\omega n^2} \hat{\mathbf{z}} \cdot \nabla_t \times \mathbf{h}_t, \\
h_z &= -i \left(\frac{\epsilon_0}{\mu_0}\right)^{1/2} \frac{c}{\omega} \hat{\mathbf{z}} \cdot \nabla_t \times \mathbf{e}_t,
\end{aligned} \tag{B.7}$$

where $n = n(x, y)$ is the refractive index profile. For a non-absorbing waveguide, $n$ is real and the above equations indicate that one can choose a phase convention where $\mathbf{e}_t$ and $\mathbf{h}_t$ are real and $e_z$ and $h_z$ are imaginary. These functions also include a normalization factor that will be determined in the next section. The parameter $\beta$ is free in the above set of equations and $\omega(\beta)$ must be chosen to satisfy the boundary conditions. In general, several solutions can be found for a given $\beta$. When the size of the core and the index discontinuity are chosen appropriately small, this degeneracy can be reduced to a minimum for a given range of wavenumbers. These fibers are called single-mode and we restrict the analysis below to these fibers. Even in this case, a given wavenumber supports two propagating modes corresponding to the two possible polarization states of the field. In standard single-mode fibers these two modes are degenerate in frequency, and travel at the same velocity. In polarization maintaining fibers, the degeneracy is lifted by breaking the circular symmetry of the core. This type of fiber is highly birefringent so that its eigenmodes have very different group velocities. This reduces the interaction between the polarization components and makes each polarization state very stable. Assuming that only one of these transverse modes is excited by an incoming pulse, the latter will travel at a group velocity

$$v_g(\beta) = \frac{\partial \omega}{\partial \beta} \tag{B.8}$$

where $\beta$ is taken as the carrier wavelength. Unless the fiber is dispersionless and perfectly linear, the intensity and phase profile of the pulse will evolve in addition to

moving at the group velocity.

The transverse mode profiles are defined for linear waveguides. It is clear that the Kerr nonlinearity will change the transverse characteristics of the field. One expects for example that very intense pulses will be better confined to the core since they increase its refractive index. For the intensities considered in this thesis however these effects are very small. Consider for example a pulse with a peak power $P_0 = 100kW$ confined to a core with an effective area $A_{eff} = 32\mu m^2$. The change in the refractive index of the core is

$$\Delta n_{NL} = n_2 P_0 / A_{eff} = 10^{-4}, \tag{B.9}$$

where we used $n_2 = 3.2 \times 10^{-16} cm^2/W$. This is a very small change compared to the refractive index difference between the core and the cladding ($\Delta n \simeq 0.01$). We shall therefore neglect the nonlinear change in transverse mode profile. Note that the Kerr effect cannot be neglected when the propagatin of the pulse is considered since even a small index change can have a significant effect when it accumulates over long distances.

## B.2 The Slowly-Varying Envelope Operator

We are interested in pulsed excitations where modes of the waveguide within a narrow band of wavenumbers around $\beta_0$ are excited. In this case, one can develop an approximate quantum field theory of reduced complexity based on a single scalar quantum field. Let $\omega_0$ be the corresponding carrier frequency. We define the slowly varying envelope operator by the expression:

$$\hat{A}(z,t) = e^{i\omega_0 t - i\beta_0 z} \int_{-\infty}^{\infty} d\beta \sqrt{\frac{v_g(\beta)}{2\pi}} \hat{a}(\beta,t) e^{i\beta z}. \tag{B.10}$$

An envelope operator can be defined for each transverse mode profile of the waveguide. The need for the weight factor inside the integral will be explained in Section B.4. For linear waveguides the time evolution of the annihilation operators is given by (B.6). In this case, the space-time evolution of $\hat{A}$ occurs only due to the bandwidth of the

superposition in (B.10).

The envelope operator provides a natural tool to describe the pulse evolution. The fast space-time dependence associated with the carrier wave is removed by the action of the prefactor in (B.10). The transverse mode profile, which is largely irrelevant to analyze the propagation of the field, has also been suppressed. The positive frequency part of the electric field operator for the excited modes, $\hat{\mathbf{E}}^+$, is given by

$$\hat{\mathbf{E}}^+(\mathbf{r},t) = \int_{-\infty}^{\infty} d\beta\, \mathbf{e}(x,y,\beta)\hat{a}(\beta,t)e^{i\beta z}, \tag{B.11}$$

It can be obtained from the envelope by the relation

$$\hat{\mathbf{E}}^+(\mathbf{r},t) = e^{-i\omega_0 t + i\beta_0 z}\mathbf{e}(x,y,\beta_0 - i\frac{\partial}{\partial z})\sqrt{\frac{2\pi}{v_g\left(\beta_0 - i\frac{\partial}{\partial z}\right)}}\hat{A}(z,t). \tag{B.12}$$

A similar expression holds for the magnetic field.

By assumption, the only modes excited should have wavenumbers very close to $\beta_0$. In particular, none of the modes with $\beta < 0$ should ever be excited. It is important to distinguish these modes from the backward propagating modes of the fiber which have been eliminated from the approximate theory. The modes with negative $\beta$ in (B.10) are unphysical and have negative frequencies by definition. They are added to the theory in order to endow it with a simple canonical structure (see Section B.4). Hence, the exact theory and the model based on the scalar field $A$ have different Hilbert spaces. The approximate theory provides a good physical description if and only if the added dimensions of its Hilbert space are left unexcited. Problems involving the coupling of forward and backward propagating pulses can also be treated in the slowly-varying envelope approximation if two independent envelopes with two distinct sets of unphysical modes are used.

## B.3 Poynting Vector and Photodetection

The normalization of the transverse mode function can now be established by considering the flow of power in the fiber. The $z$-component of the normal-ordered and time-averaged Poynting vector *integrated over the cross-section of the fiber* is given by:

$$\begin{aligned}\hat{S}_z(z,t) &= \int dA \left(\hat{\mathbf{E}}^+ \times \hat{\mathbf{H}}^- - \hat{\mathbf{H}}^+ \times \hat{\mathbf{E}}^-\right) \cdot \hat{z} \\ &= \int d\beta \int d\beta' \int dA \left\{\mathbf{e}(x,y,\beta) \times \mathbf{h}^*(x,y,\beta') + \mathbf{e}^*(x,y,\beta) \times \mathbf{h}(x,y,\beta')\right\} \cdot \hat{z} \\ &\quad \hat{a}^\dagger(\beta,t)\hat{a}(\beta',t) \exp\left[i(\beta-\beta')z\right], \end{aligned} \tag{B.13}$$

where $dA = dxdy$. The operator $\hat{S}_z(z,t)$ measures the power crossing the $z$ plane at time $t$. Upon integration over the whole fiber, we must find the total energy flow of the field

$$\int_{-\infty}^{\infty} dz \hat{S}_z(z,t) = \int_{-\infty}^{\infty} d\beta \, \hbar\omega(\beta) v_g(\beta) \hat{a}^\dagger(\beta,t)\hat{a}(\beta,t). \tag{B.14}$$

This requires that the transverse mode profiles be normalized so that

$$\int dA \left\{\mathbf{e}(x,y,\beta) \times \mathbf{h}^*(x,y,\beta) + \mathbf{e}^*(x,y,\beta) \times \mathbf{h}(x,y,\beta)\right\} \cdot \hat{z} = \frac{\hbar\omega(\beta)v_g(\beta)}{2\pi}. \tag{B.15}$$

This is our normalization condition. Using this expression, one can derive a useful approximate relation between the Poynting vector and the envelope. Noting that for the narrow bandwidth pulses considered here, the transverse mode profiles change little for the various excited wavenumbers, we can replace $\omega(\beta)v_g(\beta)$ by $\omega(\beta_0)v_g(\omega_0)$ in (B.15). We then find

$$\hat{S}_z(z,t) \simeq \hbar\omega_0 \hat{A}^\dagger(z,t)\hat{A}(z,t) \tag{B.16}$$

Hence, for narrow bandwidth pulses, $\hat{A}^\dagger(z,t)\hat{A}(z,t)$ can be interpreted as the photon flux operator.

In the electric dipole approximation, matter couples to the electromagnetic field through the electric field. Glauber showed that as a result, photodetectors measure the Poynting vector of this field integrated over its cross-section. In all cases con-

thesis, the photodetector response time is much longer than the pulse

noting by $\hat{I}$ the photocurrent operator generated by such a detector

ve have, from the previous expression,

$$\hat{I} = I_0 \int dt \hat{A}^\dagger(z,t)\hat{A}(z,t), \tag{B.17}$$

where the constant $I_0$ is the photocurrent generated by a single electron circulating in the electronic circuit.

## B.4 Equal-Space Commutation Relations

The addition of the unphysical modes allow to derive simple *equal-space* commutation relations for the scalar envelope. Consider first a linear waveguide where the annihilation operators obey (B.6). In this case one has has:

$$\begin{aligned}
[\hat{A}(z,t), \hat{A}^\dagger(z,t')] &= e^{i\omega_0(t-t')} \int d\beta d\beta' \frac{\sqrt{v_g(\beta)v_g(\beta')}}{2\pi} e^{i(\beta-\beta')z - i\omega(\beta)t + i\omega(\beta')t'} [\hat{a}(\beta), \hat{a}^\dagger(\beta')] \\
&= e^{i\omega_0(t-t')} \int_{-\infty}^{\infty} d\beta \frac{v_g(\beta)}{2\pi} e^{-i\omega(\beta)(t-t')} \\
&= e^{i\omega_0(t-t')} \int_{-\infty}^{\infty} \frac{d\omega}{2\pi} e^{-i\omega(t-t')} \\
&= \delta(t-t').
\end{aligned}$$

The true nature of the mode with $\beta < 0$ is revealed by the next to last step. If one were to use $\omega(-\beta) = \omega(\beta)$, which is appropriate for the backward propagating modes, the function $v_g(\beta)$ would be odd and the integral would vanish. The delta function arises only when the range of $\omega$ extends over the whole axis. A similar calculation can be done for $[\hat{A}(z,t), \hat{A}(z,t')]$ so that one has

$$[\hat{A}(z,\tau), \hat{A}(z,\tau')] = 0, \quad [\hat{A}(z,\tau), \hat{A}^\dagger(z,\tau')] = \delta(\tau - \tau'). \tag{B.18}$$

Note that the spatial coordinates being the same for both fields in the commutators, one can use either the time $t$ or the retarded time $\tau = t - z/v_g$ in these expressions.

Assume now that the region between $z = 0$ and $z = l$ contains a nonlinear medium. We will ignore any reflection occuring at the interface between the linear and nonlinear waveguides. The input envelope $\hat{A}(0,t)$ satisfies the equal-space commutators (B.18) since it is incident from a region where these relations are satisfied everywhere. At a distance $z$ inside the nonlinear waveguide, the envelope is given by the unitary transformation:

$$\hat{A}(z,t) = e^{-iz\hat{P}_z}\hat{A}(0,t)e^{iz\hat{P}_z}, \tag{B.19}$$

where the operator $\hat{P}_z$ measures the total momentum of the field and of the waveguide in the direction $z$. By assumption this system is closed so that $\hat{P}_z$ is a conserved quantity. One therefore has

$$\begin{aligned}[\hat{A}(z,t), \hat{A}^\dagger(z,t')] &= e^{-iz\hat{P}_z}[\hat{A}(0,t), \hat{A}^\dagger(0,t')]e^{iz\hat{P}_z} \\ &= \delta(t-t'),\end{aligned} \tag{B.20}$$

and a similar result for $[\hat{A}(z,t), \hat{A}(z,t')]$. The commutators (B.18) are therefore also satisfied in the nonlinear waveguide.

## B.5 The Frequency Convention

Due to the assumption of a one-to-one correspondence between frequencies and wavenumbers, one can trade the previous expressions based on a wavenumber decomposition for frequency expansions. We first Fourier transform the operators $\hat{a}(\beta,t)$

$$\begin{aligned}\hat{a}(\beta,\omega) &= \int_{-\infty}^{\infty}\frac{dt}{2\pi}\hat{a}(\beta,t)e^{i\omega t}, \\ \hat{a}(\beta,t) &= \int_{-\infty}^{\infty}d\omega\hat{a}(\beta,\omega)e^{-i\omega t}.\end{aligned} \tag{B.21}$$

When the medium is linear so that (B.6) applies, we find

$$\hat{\tilde{a}}(\beta,\omega) = \delta\left(\omega - \omega(\beta)\right)\hat{a}(\beta,0). \tag{B.22}$$

Defining the frequency annihilation operator by

$$\begin{aligned}\hat{a}(z,\omega) &= \int d\beta\sqrt{v_g(\beta)}e^{i\beta z}\hat{a}(\beta,\omega),\\ \hat{a}(\beta,\omega) &= \frac{1}{\sqrt{v_g(\beta)}}\int\frac{dz}{2\pi}e^{-i\beta z}\hat{a}(z,\omega).\end{aligned} \tag{B.23}$$

Using these definitions, one can write the envelope operator as

$$\hat{A}(z,t) = e^{i\omega_0 t - i\beta_0 z}\int_{-\infty}^{\infty}\frac{d\omega}{\sqrt{2\pi}}\,\hat{a}(z,\omega)e^{-i\omega t}. \tag{B.24}$$

The commutation relations of the frequency annihilation and creation operators can be obtained by Fourier transforming (B.18)

$$\begin{aligned}\left[\hat{a}(z,\omega),\hat{a}^{\dagger}(z,\omega')\right] &= \delta(\omega-\omega'),\\ \left[\hat{a}(z,\omega),\hat{a}(z,\omega')\right] &= 0.\end{aligned} \tag{B.25}$$

The positive frequency part of the electric field can be expressed as

$$\begin{aligned}\hat{\mathbf{E}}^{+}(\mathbf{r},t) &= \int d\beta\mathbf{e}(x,y,\beta)e^{i\beta z}\int d\omega\hat{a}(\beta,\omega)e^{-i\omega t}\\ &= \int d\omega e^{-i\omega t}\int dz'\hat{a}(z',\omega)\int d\beta\frac{\mathbf{e}(x,y,\beta)}{\sqrt{v_g(\beta)}}e^{i\beta(z-z')}.\end{aligned}$$

As can be seen from this expression, the relation between the electric field and the frequency operators is in general nonlocal. As the electric field itself is local, this indicates that $\hat{a}(z,\omega)$ is nonlocal. When the bandwidth of the modes is so narrow that the $\beta$ dependence of the group velocity and of the transverse profile can be neglected, the above relation becomes local

$$\hat{\mathbf{E}}^{+}(\mathbf{r},t) = \int d\omega e^{-i\omega t}\mathbf{e}(x,y,\omega)\hat{a}(z,\omega), \tag{B.26}$$

where the frequency mode profile are efined by

$$\mathbf{e}(x,y,\omega) = \frac{\mathbf{e}(x,y,\beta(\omega))}{\sqrt{v_g(\beta(\omega))}}. \tag{B.27}$$

Expression (B.120 can then be traded with

$$\hat{\mathbf{E}}^+(\mathbf{r},t) = e^{-i\omega_0 t + i\beta_0 z}\mathbf{e}(x,y,\omega_0 + i\frac{\partial}{\partial t})\hat{A}(z,t). \tag{B.28}$$

## B.6 Equation of Motion

Consider first a linear medium for which

$$\hat{a}(z,\omega) = e^{i\beta(\omega)z}\hat{a}(0,\omega). \tag{B.29}$$

Using this spatial dependence in (B.24), one can relate the spatial derivative of the envelope to its time derivatives

$$\frac{\partial \hat{A}}{\partial z} = -\frac{1}{v_g}\frac{\partial \hat{A}}{\partial t} + D\hat{A}(z,t) \tag{B.30}$$

where $D$ is given by (3.16). The Kerr effect creates a change in the local refractive index proportional to the intensity of the field. This change modifies dynamically the wavenumbers resulting in

$$\beta(\omega) \rightarrow \beta(\omega) + \Delta\hat{\beta}(z,t). \tag{B.31}$$

When the pulse bandwidth is large, the exact relation between the index change and the intensity of the envelope is complicated. This question will be partially addressed in Chapter 4. For narrow bandwidth pulses however the intensity of the field is proportional to $\hat{A}^\dagger\hat{A}$. Assuming that the index reacts instantaneously to the optical field, we find

$$\Delta\hat{\beta}(z,t) = \kappa\hat{A}^\dagger(z,t)\hat{A}(z,t), \tag{B.32}$$

where the constant $\kappa$ is the Kerr coefficient. This change in wavenumber leads to the envelope equation

$$\frac{\partial}{\partial z}\hat{A}(z,\tau) = \left(D + i\hat{N}(z,\tau)\right)\hat{A}(z,\tau), \tag{B.33}$$

where

$$\hat{N}(z,\tau) = \kappa\hat{A}^{\dagger}(z,\tau)\hat{A}(z,\tau) \tag{B.34}$$

where we introduced the retarded time $\tau = t - z/v_g$ to eliminate the first order time derivative. The above equation is the well-known quantized nonlinear Schrödinger equation (QNSE) in 1+1 dimensions.

One does not need to use space as the evolution parameter in the description of the envelope. Equation (B.30) was obtained by expressing $\beta$ in terms of $\omega$ in the envelope. Similarly, a time derivative of the envelope can be related to a series of spatial derivatives by expressing $\omega$ in terms of $\beta$. In this case, the envelope evolution is described by the QNSE with a first order time derivative and a second order spatial derivative. One is left with the problem of providing an initial condition for this system. The QNSE is a fairly universal equation which describes the nonlinear evolution of almost any scalar dispersive field for some range of intensities. Not surprisingly then, it is recovered when time or space is used for the evolution parameter.

# Appendix C

# Useful Formulae

In this Appendix, a number of useful formulas are summarized. The various expectation values of the continuous time self phase modulation operator are evaluated using:

$$\exp\left(\int ds\, g(s)\hat{A}_i^\dagger(s)\hat{A}_i(s)\right) =: \exp\left(\int ds\, h(s)\hat{A}_i^\dagger(s)\hat{A}_i(s)\right) :, \tag{C.1}$$

where $g(s)$ is an arbitrary function and $h(s) = e^{g(s)} - 1$. Here : $F(\hat{A}_i^\dagger, \hat{A}_i)$ : means that in the Taylor expansion of $F$, all creation operators are on the left of the annihilation operators. A simpler formula is used in the discretized theory to evaluate expectation values of the phase factor in (4.46) [83]:

$$\exp\left(g\hat{a}_n^\dagger(0)\hat{a}_n(0)\right) =: \exp\left(h\hat{a}_n^\dagger(0)\hat{a}_n(0)\right) :, \tag{C.2}$$

where this time $g$ is a complex number and $h = e^g - 1$.

Gaussian, sech and square pulses are defined in terms of the pulse time scale (4.57) by:

$$\alpha(\tau) = \sqrt{n_0/\tau_p}\, \exp\left(-\pi\tau^2/2\tau_p^2\right), \tag{C.3}$$

$$\alpha(\tau) = \sqrt{n_0/\tau_p}\, \mathrm{sech}(2\tau/\tau_p) \tag{C.4}$$

$$\alpha(\tau) = \sqrt{n_0/\tau_p}\left[u(\tau + \frac{\tau_p}{2}) - u(\tau - \frac{\tau_p}{2})\right] \tag{C.5}$$

respectively. Note that in all cases we have $\int d\tau |\alpha(\tau)|^2 = n_0$.

# Appendix D

# Expressions for $F_1$ and $F_2$

In this Appendix, we outline the derivation of expressions (4.48) and (4.50) for $F_1$ and $F_2$. Consider first the continuous theory. From (4.30) and (4.39), we have:

$$\left|\left\langle \hat{A}_o^\dagger(\tau_1)\hat{A}_o(\tau_2)\right\rangle\right|^2 = |\alpha(\tau_1)\alpha(\tau_2)|^2 \left|\left\langle e^{-i\hat{\phi}(\tau_1)}e^{i\hat{\phi}(\tau_2)}\right\rangle \left\langle e^{-i\hat{\theta}(\tau_1)}e^{i\hat{\theta}(\tau_2)}\right\rangle\right|^2. \tag{D.1}$$

The self phase modulation exponential are first brought into a form suitable for the use of the normal ordering formula (C.1). From $[\hat{\phi}(\tau_1), \hat{\phi}(\tau_2)] = 0$ and $e^A e^B = e^{A+B}e^{1/2[A,B]}$, we have:

$$e^{-i\hat{\phi}(\tau_1)}e^{i\hat{\phi}(\tau_2)} = \exp\left(\int ds g(\tau_1, \tau_2, s)\hat{A}_i^\dagger(s)\hat{A}_i(s)\right), \tag{D.2}$$

where $g(\tau_1, \tau_2, s) = il\{f(\tau_2 - s) - f(\tau_1 - s)\}$ and, by definition, $f(\tau)$ vanishes for negative $\tau$. The expectation value of (D.2) in a coherent state is obtained by replacing $\hat{A}_i$ and $\hat{A}_i^\dagger$ by $\alpha$ and $\alpha^*$ on the right hand side of (C.1). The real part of $h(\tau_1, \tau_2, s) = e^{g(\tau_1,\tau_2,s)} - 1$ then determines the norm of the expectation value of (D.2). We find:

$$\left|\left\langle e^{-i\hat{\phi}(\tau_1)}e^{i\hat{\phi}(\tau_2)}\right\rangle\right|^2 = \exp\left(-2n_0 + K_{cc}(\tau_1, \tau_2)\right)\exp\left(K_{ss}(\tau_1, \tau_2)\right), \tag{D.3}$$

where the $K$-integrals were defined by (4.49). The expectation value of the Raman noise exponentials in (D.1) is evaluated in the following way. We first note that $[\hat{\theta}(\tau_1), \hat{\theta}(\tau_2)] = il\{f(\tau_2 - \tau_1) - f(\tau_1 - \tau_2)\}$. One can then combine the noise expo-

nents without affecting the norm in (D.1): $\left|\left\langle e^{-i\hat{\theta}(\tau_1)}e^{i\hat{\theta}(\tau_2)}\right\rangle\right|^2 = \left|\left\langle e^{-i\hat{\theta}(\tau_1)+i\hat{\theta}(\tau_2)}\right\rangle\right|^2$. Using (4.5) and (4.32), we have:

$$\begin{aligned} -i\hat{\theta}(\tau_1)+i\hat{\theta}(\tau_2) &= \int_0^l dz \int_0^\infty d\omega \left\{\lambda(\omega)\hat{d}^\dagger_\omega(z) - \lambda^*(\omega)\hat{d}_\omega(z)\right\} \\ &= \lim_{\Delta z\Delta\omega\to 0}\sum_{i,j}\left\{L_j\hat{D}^\dagger_{i,j} - L^*_j\hat{D}_{i,j}\right\}, \end{aligned} \tag{D.4}$$

with $\lambda(\omega) = i\left(e^{i\omega\tau_2} - e^{i\omega\tau_1}\right)\sqrt{\tilde{f}''(\omega)/\pi}$. On the second line we expressed the integrals as the limit of a double sum, with $\hat{D}_{i,j} = \sqrt{\Delta z\Delta\omega}\hat{d}_{\omega_j}(z_i)$ and $L_j = \sqrt{\Delta z\Delta\omega}\lambda(\omega_j)$. Note that $[\hat{D}_{i,j}, \hat{D}^\dagger_{k,l}] = \delta_{i,k}\delta_{j,l}$, so that $\hat{D}_{k,l}$ are annihilation operators of independent harmonic oscillators. Since, from (4.13), these oscillators are in thermal equilibrium, we have:

$$\left|\left\langle e^{-i\hat{\theta}(\tau_1)}e^{i\hat{\theta}(\tau_2)}\right\rangle\right|^2 = \prod_{i,j}\left|Tr\left\{\rho_{BE}e^{L_j\hat{D}^\dagger_{i,j} - L^*_j\hat{D}_{i,j}}\right\}\right|^2, \tag{D.5}$$

where $\rho_{BE}$ is the density matrix for the Bose-Einstein distribution. The trace for each harmonic oscillator yields the characteristic function for its symmetrically ordered moments[94]. We therefore have:

$$\left|Tr\left\{\rho_{BE}e^{L_j\hat{D}^\dagger_{i,j} - L^*_j\hat{D}_{i,j}}\right\}\right|^2 = \exp\left(-|L_j|^2\coth\left(\frac{\hbar\omega_j}{2kT}\right)\right). \tag{D.6}$$

The product of the exponentials in (D.5) transforms into the exponential of an integral, so that:

$$\begin{aligned} \left|\left\langle e^{-i\hat{\theta}(\tau_1)}e^{i\hat{\theta}(\tau_2)}\right\rangle\right|^2 &= \exp\left(-l\int_0^\infty d\omega|\lambda(\omega)|^2\coth\left(\frac{\hbar\omega}{2kT}\right)\right) \\ &= e^{-\kappa l(M(0)-M(\tau_1-\tau_2))}. \end{aligned} \tag{D.7}$$

Using (D.3) and (D.7) into (D.1), we find:

$$\left|\left\langle \hat{A}^\dagger_o(\tau_1)\hat{A}_o(\tau_2)\right\rangle\right|^2 = e^{-\kappa l M(0)}|\alpha(\tau_1)\alpha(\tau_2)|^2 e^{-2n_0+K_{cc}(\tau_1,\tau_2)}e^{K_{ss}(\tau_1,\tau_2)+\kappa l M(\tau_1-\tau_2)}. \tag{D.8}$$

Following a similar procedure, one finds:

$$\left|\left\langle \hat{A}_o(\tau_1)\hat{A}_o(\tau_2)\right\rangle\right|^2 = e^{-\kappa l M(0)}|\alpha(\tau_1)\alpha(\tau_2)|^2 e^{-2n_0+K_{cc}(\tau_1,\tau_2)}e^{-K_{ss}(\tau_1,\tau_2)-\kappa l M(\tau_1-\tau_2)}. \quad \text{(D.9)}$$

This last result requires the use of the permutation formula:

$$\hat{A}_i(\tau_1)e^{i\hat{\phi}(\tau_2)} = e^{ilf(\tau_2-\tau_1)}e^{i\hat{\phi}(\tau_2)}\hat{A}_i(\tau_1), \quad \text{(D.10)}$$

which follows from (4.31) after normal ordering of the exponential using (C.1). The additional phase resulting from the permutation does not however affect the norm (D.9). Expressions (D.8) and (D.9) together with the definition (3.5), immediately yield $F_1$ in (4.48). The expression for $F_2$ is most easily derived when using the equality $\hat{A}_o^\dagger(\tau_2)\hat{A}_o(\tau_2) = \hat{A}_i^\dagger(\tau_2)\hat{A}_i(\tau_2)$. One then has:

$$\begin{aligned}
&\left\langle \hat{A}_o^\dagger(\tau_2)\hat{A}_o(\tau_2)\hat{A}_o(\tau_1)\right\rangle \left\langle \hat{A}_o^\dagger(\tau_1)\right\rangle \\
&\quad = |\alpha(\tau_1)|^2\alpha^*(\tau_2)\left\langle \hat{A}_i(\tau_2)e^{i\hat{\phi}(\tau_1)}\right\rangle \left\langle e^{-i\hat{\phi}(\tau_1)}\right\rangle \left|\left\langle e^{i\hat{\theta}(\tau_1)}\right\rangle\right|^2 \\
&\quad = |\alpha(\tau_1)\alpha(\tau_2)|^2 e^{ilf(\tau_1-\tau_2)}\left|\left\langle e^{i\hat{\phi}(\tau_1)}\right\rangle \left\langle e^{i\hat{\theta}(\tau_1)}\right\rangle\right|^2, \quad \text{(D.11)}
\end{aligned}$$

where we used (D.10) in the last equality. The norm of the expectation values are evaluated as before, with the result:

$$\left|\left\langle e^{i\hat{\phi}(\tau_1)}\right\rangle\right|^2 = e^{-2n_0+K_c(\tau_1)} \quad \text{(D.12)}$$

$$\left|\left\langle e^{i\hat{\theta}(\tau_1)}\right\rangle\right|^2 = e^{-\frac{\kappa l}{2}M(0)}. \quad \text{(D.13)}$$

Using the above expressions in (D.11) and taking the imaginary part, we find $F_2$ in (4.48).

The derivation of the discretized formulas (4.50) is simplified by the absence of Raman noise factors and by the independence of oscillators with different indices. One verifies, for example, that $F_1$ and $F_2$ can be written as:

$$F_1 = \sum_n \left\{\left|\left\langle \hat{a}_n^\dagger(0)\hat{a}_n(0)\right\rangle\right|^2 - \left|\left\langle \hat{a}_n^2(l)\right\rangle\right|^2\right\}, \quad \text{(D.14)}$$

$$F_2 = 4Im \sum_n \left\langle \hat{a}_n(0)^\dagger \hat{a}_n(0) \hat{a}_n(l) \right\rangle \left\langle \hat{a}_n^\dagger(l) \right\rangle . \tag{D.15}$$

One can then use the normal ordering formula (C.2) instead of (C.1) to evaluate the various factors arising from self phase modulation. We find:

$$\begin{aligned} \left| \left\langle \hat{a}_n^\dagger(0) \hat{a}_n(0) \right\rangle \right|^2 - \left| \left\langle \hat{a}_n^2(l) \right\rangle \right|^2 &= |\alpha_n|^4 \left\{ 1 - \exp\left( -4 \sin^2 \left( \frac{\kappa}{\Delta\tau} l \right) \right) \right\} \\ \left\langle \hat{a}_n(0)^\dagger \hat{a}_n(0) \hat{a}_n(l) \right\rangle \left\langle \hat{a}_n(l) \right\rangle &= |\alpha(\tau)|^4 \exp\left( -4 \sin^2 \left( \frac{\kappa l}{2\Delta\tau} \right) \right) \\ &\times \exp\left( i \frac{\kappa}{\Delta\tau} l \right), \end{aligned} \tag{D.16}$$

leading immediately to (4.50).

# Appendix E

# Matrix Elements Between n-Photon Soliton States

According to [104] we obtain for the matrix elements of the field operator between an $n$-photon soliton with momentum $p'$ and an $m$-photon soliton with momentum $p$

$$\begin{aligned} < n, p' | \hat{\phi}(x) | m, p > &= \delta_{m,n+1} \frac{\sqrt{1+1/n}}{2\sqrt{|c|}} e^{i((n+1)p - np')x} \mathrm{sech}\,(\pi a) \\ &\times \frac{\Gamma^2(n+1)}{|\Gamma(n+1/2+ia)|^2}, \end{aligned} \tag{E.1}$$

with $a = \frac{p-p'}{|c|}$ and where $\Gamma(x)$ is Eulers Gamma function. For large photon number we can expand the ratio between the Gamma functions in (E.1) according to [111]

$$\frac{\Gamma^2(n+1)}{|\Gamma(n+1/2+ia)|^2} = n\left(1 + \frac{1}{n}\left(\frac{1}{4} + a^2\right) + O(1/n^2)\right) \tag{E.2}$$

and obtain up to second order in the inverse number of photons

$$\begin{aligned} < n, p' | \hat{\phi}(x) | m, p > &= \delta_{m,n+1} \frac{n}{2\sqrt{|c|}} \mathrm{sech}\,(\pi a)\, e^{i((n+1)p - np')x} \\ &\times \left[1 + \frac{1}{n}\left(\frac{3}{4} + a^2\right) + O(1/n^2)\right] \end{aligned} \tag{E.3}$$

Employing the integrals derived in the appendices of refs.([104, 105]), we get for the matrix elements of the two point correlation function

$$\begin{aligned} < n,p'|\hat{\phi}(x)\hat{\phi}(x+\tau)|m,p > &= \delta_{m,n+2}\frac{\sqrt{1+2/n}}{2}\frac{i(n+1)}{\sinh(\pi a)} \\ &\times \; e^{i(p-p')nx+ip(2x+\tau)+\frac{c}{2}|\tau|}S(n) \end{aligned} \tag{E.4}$$

and

$$< n,p'|\hat{\phi}^{\dagger}(x)\hat{\phi}(x+\tau)|m,p >= \delta_{m,n}\frac{i}{2n}\frac{\exp[i(p-p')nx+ip\tau]}{\sinh(\pi a)}S(n-1) \tag{E.5}$$

with

$$S(n) = \frac{(-i)\Gamma^2(n+1)}{|\Gamma(n+1+ia)|^2}\sum_{l=0}^{n_0}(2l-n-ia)e^{i(n-l)(p-p')\tau+[-(l-\frac{n_0}{2})^2+\frac{n_0}{2}\left(1+\frac{n_0}{2}\right)]c\tau}, \tag{E.6}$$

In the limit of large photon number we can also expand the sum $S(n)$ with respect to the inverse photon number. For doing so we scale the time in units of the soliton width, i.e. we introduce $\tau_n = n|c|\tau/2$, $y = \tau_n(p-p')/|c|$ and change the summation in eq.(E.6) to $k = l - n/2$ where we assume for the moment that $n$ is an even number.

$$\begin{aligned} S(n) &= \frac{i\Gamma^2(n+1)}{|\Gamma(n+1+ia)|^2}e^{-\tau_n+iy}\sum_{k=-n/2}^{n/2}(2k-ia)e^{-i2ky/n}\exp\left[\left(k^2-(\frac{n}{2})^2\right)\frac{2\tau_n}{n}\right] \\ &= \frac{\Gamma^2(n+1)}{|\Gamma(n+1+ia)|^2}e^{-\tau_n+iy}\left(a-n\frac{\partial}{\partial y}\right) \\ &\times \left(e^{-\tau_n n/2}+2Re\left\{e^{-iy}\sum_{k=0}^{n/2-1}\exp\left[-i2ky/n-2\tau_n(k(n-k))/n\right]\right\}\right) \end{aligned} \tag{E.7}$$

The remaining sum in this equation can be evaluated by expanding the exponential with the $k^2$ dependence and performing the remaining geometric series

$$\begin{aligned} &\sum_{k=0}^{n/2-1}\exp\left[-i2ky/n-2\tau_n(k(n-k))/n\right] \\ &= \sum_{m=0}^{\infty}\frac{\left(-\frac{\tau_n}{2n}\right)^m}{m!}\left(\frac{\partial}{\partial\tau_n}\right)^{2m}\left[\frac{1-e^{-n\tau_n+iy}}{1-e^{-2\tau_n+2iy/n}}\right] \end{aligned} \tag{E.8}$$

This equation shows, that the sum consists of two parts. One which varies on a time scale of the order of the soliton width $\tau_n$ and one part which decays on a time scale $n\tau_n$. We can neglect this rapidly decaying part, expand the rest up to second order in the inverse photon number and arrive at the expression

$$\begin{aligned} & \sum_{k=0}^{n/2-1} \exp\left[-i2ky/n - 2\tau_n(k(n-k))/n\right] \\ = \; & \frac{e^{\tau_n}}{2\sinh(\tau_n)} + \frac{iy}{2n\sinh^2(\tau_n)} + \frac{\tau_n \cosh(\tau_n)}{2n\sinh^3(\tau_n)} \end{aligned} \tag{E.9}$$

Substitution of this result into eq.(E.7) and the asymptotic expansion [111]

$$\frac{\Gamma^2(n+1)}{|\Gamma(n+1+ia)|^2} = 1 + \frac{a^2}{n} \tag{E.10}$$

leads to

$$\begin{aligned} S(n) \;=\; & \left(1 + \frac{a^2}{n_0}\right) e^{ia\tau_n} \frac{\pi e^{ia\tau_n}}{\sinh(\pi a)} \\ \times \; & \left\{ n \frac{\sin(a\tau_n)}{\sinh(\tau_n)} + a \frac{\cos(a\tau_n)}{\sinh(\tau_n)} \right. \\ & -e^{-\tau_n} \left( \frac{a\tau_n \cos(a\tau_n) + \sin(a\tau_n)}{\sinh^2(\tau_n)} \right) \\ & \left. +\tau_n e^{-\tau_n} \frac{\cosh(\tau_n)\sin(a\tau_n)}{\sinh^3(\tau_n)} + O(1/n) \right\} \end{aligned} \tag{E.11}$$

One can easily test on a computer, that the error between (E.6) and (E.11) vanishes with $1/n^2$.

# Appendix F

# Poisson's Sum Formula

In this appendix we want to lay out how to perform the average over the photon number statistics, which are sums of the type

$$F = \sum_{n=0}^{\infty} \frac{1}{\sqrt{2\pi n_0}} e^{-(n-n_0)^2/2n_0} f(n) e^{i(an^2+bn)t}. \tag{F.1}$$

Poissons sum formula gives the connection between a periodic function generated by shifting a function $G(y)$ by multiples of $2\pi$ and the corresponding Fourier coefficients [113] according to

$$\sum_{n=-\infty}^{\infty} G(y + 2n\pi) = \sum_{m=-\infty}^{\infty} h(m) e^{imy} \tag{F.2}$$

with

$$G(y) = \int h(m) e^{imx} dm. \tag{F.3}$$

Since we are only interested in an approximation to eq.(F.1) valid up to second order in the inverse photon number, we can extend the sum over n to minus infinity and expand the function $f(n)$ in a Taylor series around the maximum of the Gaussian. Thus we are left with Gaussian integrals and obtain

$$F = \sum_{k=0}^{\infty} \sum_{l=-\infty}^{\infty} \frac{(-i)^k}{k!} f^{(k)}(n_0) \left(\frac{\partial}{\partial y}\right)^k G_\phi(y + 2\pi l)|_{y=0} \tag{F.4}$$

with

$$G(y) = \frac{e^{i(an_0^2+ibn_0)t}}{\sqrt{1-2ian_0t}} \exp\left\{-\frac{n_0}{2}\frac{[y+(2an_0+b)t]^2}{1-2ian_0t}\right\}. \tag{F.5}$$

# Appendix G

# Evaluation of the Mean Field

We use ref. [104] to determine the expectation value of the field operator but we expand the results up to second order in the inverse photon number. In appendix A we computed the matrix elements of the field operator for a fundamental soliton (E.1). With the expression for the asymptotic behavior of the matrix elements for large photon number (E.3) we obtain for the mean field with (5.7), (5.17) and (5.20)

$$
\begin{aligned}
< \psi(t)|\hat{\phi}(x)|\psi(t) > &= \sum_{n=0}^{\infty} p_n \frac{\sqrt{n_0}}{\sqrt{n+1}} \int dp\, dp' \frac{1}{\sqrt{2\pi}\Delta p} \\
&\times \exp\left\{ -\frac{1}{4\Delta^2 p}\left[(p-p_0)^2 + (p'-p_0)^2\right]\right\} \\
&\times \exp\left[ i\left( (n+\frac{1}{2})(p-p')(x-x_0) + \frac{1}{2}(p+p')(x-x_0)\right)\right] \\
&\times \left(1 + \frac{1}{4n}\left(1 + \frac{4(p-p')^2}{|c|^2}\right)\right) \exp\left[ i\frac{|c|^2}{4} n(n+1)t\right] \\
&\times \exp\left[ -i\left( (n+\frac{1}{2})(p^2 - p'^2) + \frac{1}{2}(p^2+p'^2)\right) t\right] \\
&\times \operatorname{sech}[\pi \frac{(p-p')}{|c|}]
\end{aligned}
\tag{G.1}
$$

Transformation to the new variables $u = (p-p')/2$ and $v = (p+p')/2$ gives us

$$
\begin{aligned}
< \psi(t)|\hat{\phi}(x)|\psi(t) > &= \sum_{n=0}^{\infty} p_n |c|^{-1/2} \sqrt{n_0 n} \exp\left[ i\frac{|c|^2}{4} n(n+1)t\right] \\
&\times \int dv g(v) e^{i(x-x_0)v - iv^2 t}
\end{aligned}
$$

$$\times \int du \exp\left[\frac{-u^2}{2\Delta p^2} - iu^2 t\right] \exp\left[i(2n+1)(x-x_0)u\right]$$
$$\times \left(1 + \frac{1}{4n}\left(1 + \frac{16u^2}{|c|^2}\right) + O\left(\frac{1}{n^2}\right)\right) \operatorname{sech}\left(\frac{2\pi u}{|c|}\right). \quad \text{(G.2)}$$

If we evaluate the integral over the variable $u$ we have to make sure that the resulting expression is consistent with the desired expansion in $1/n_0$. Using the expression for $\Delta p$ according to (5.22) we have to expand the Gaussian in $u$ up to first order to obtain a valid expansion

$$< \psi(t)|\hat{\phi}(x)|\psi(t) >= \sum_{n=0}^{\infty} p_n \frac{\sqrt{n_0|c|}}{2}\sqrt{n} \exp\left[i\frac{|c|^2}{4}n(n+1)t\right] \int dv g(v) e^{i(x-x_0)v - iv^2 t}$$
$$\times \left(1 + \frac{1}{4n} + \frac{x_n}{2n}\frac{\partial}{\partial x_n} + \left(\frac{\mu + 2i\Phi_{nl}/n_0}{8n_0} - \frac{1}{4n}\right)\frac{\partial^2}{\partial x_{n+1/2}^2} + O\left(\frac{1}{n^2}\right)\right)$$
$$\times \operatorname{sech}(x_n) \quad \text{(G.3)}$$

where we have introduced $x_n = \frac{|c|n}{2}(x - x_0 - 2v\,t)$ and made use of the nonlinear phase shift $\Phi_{nl} = \frac{n_0|c|^2}{4}t$.

To carry out the sum over $n$, the Poisson photodistribution is replaced by the Gaussian

$$p_n = \frac{1}{\sqrt{2\pi n_0}} \exp\left[-\frac{(n-n_0)^2}{2n_0}\right]. \quad \text{(G.4)}$$

This change is legitimate for large $n_0$ and does not affect the moments of the distribution up to second order in the inverse photon number. Using Poisson's sum formula (Appendix F), we find

$$< \psi(t)|\hat{\phi}(x)|\psi(t) >= \int dv g(v) e^{i(x-x_0)v - iv^2 t} F_\phi(x_{n_0}(v)) \quad \text{(G.5)}$$

with

$$F_\phi(x_{n_0}) = \sum_{l=-\infty}^{\infty} \sum_{k=0}^{\infty} \frac{1}{k!} f_\phi^{(k)}(n_0) \left(-i\frac{\partial}{\partial y}\right)^k G_\phi(y + 2\pi l)|_{y=0}, \quad \text{(G.6)}$$

where $f_\phi^{(k)}(n_0)$ denotes the k-th derivative with respect to $n_0$ of the function $f_\phi$ defined

by

$$f_\phi(n) = \frac{\sqrt{n_0|c|}}{2}\sqrt{n}\left(1+\frac{1}{4n}+\frac{x_n}{2n}\frac{\partial}{\partial x_n} + \left(\frac{\mu+2i\Phi_{nl}/n_0}{8n_0}-\frac{1}{4n}\right)\frac{\partial^2}{\partial x_n^2}+O\left(\frac{1}{n^2}\right)\right)\mathrm{sech}\,(x_n) \tag{G.7}$$

and

$$G_\phi(y) = \frac{e^{i\Phi_{nl}(1+1/n_0)}}{\sqrt{1-2i\Phi_{nl}/n_0}}\exp\left\{-\frac{n_0}{2}\frac{[y+(1+\frac{1}{2n_0})(\frac{2\Phi_{nl}}{n_0})]^2}{1-2i\Phi_{nl}/n_0}\right\}, \tag{G.8}$$

Since we restrict ourselve to moderate phase shifts, $\Phi_{nl} < n_0$, the only important term with in (G.6) has $l = 0$, the rest being exponentially suppressed. We can therefore use

$$F_\phi(x_{n_0}) = \sum_{k=0}^{\infty}\frac{(-i)^k}{k!}f_\phi^{(k)}(n_0)G_\phi^{(k)}(y)|_{y=0}. \tag{G.9}$$

We must retain only terms of order 1 and $1/n_0$ in this expression to be consistent with our approximation level. The maxima of the derivatives of the function $G_\phi$ and $f_\phi$ have the following scaling

$$\mathrm{Max}\{G^{(k)}\} \approx \sqrt{n_0}^k \tag{G.10}$$

and

$$\mathrm{Max}\{f^{(k)}\} \approx n_0^{-k} \tag{G.11}$$

In order to obtain a result correct up to second order in $1/n_0$ it is enough to keep the first three terms in (G.9). The function $G_\phi(0)$ describes the impact on the mean field of the phase spreading due to photon number fluctuations. The absolute value of this function is

$$|G_\phi(0)| = \frac{1}{\sqrt{1+(2\Phi_{nl}/n_0)^2}}\exp\left\{-\frac{4\Phi_{nl}^2}{n_0}\frac{[1+\frac{1}{2n_0}]^2)}{1+\left(\frac{2\Phi_{nl}}{n_0}\right)^2}\right\}. \tag{G.12}$$

Thus as long as $\Phi_{nl} \ll \sqrt{n_0}$ the phase spreading is negligible and does not decrease the mean field. Once the threshold $\Phi_{nl} = \sqrt{n_0}$ is reached the mean field is rapidly

suppressed. However, the phase spreading is only one quantum effect initiated by the photon number fluctuations. The other effect is position spreading due to fluctuations in momentum or center frequency of the soliton. We encounter this effect when we perform the average over the momentum distribution, where we have to remember that $x_{n_0}(v) = n_0|c|(x - x_0 - 2vt)/2$. In (G.5) we have to perform a Fourier transform over the product of a Gaussian with width $\Delta v = \Delta p = 1/(\sqrt{\mu n_0}\tau_0)$ and the function $F_\phi$ which has, for example at $x = 0$, a width $\Delta v = 1/(\Phi_{nl}\tau_0)$.

As long as $\Phi_{nl} \ll \sqrt{n_0}$ the Gaussian is much narrower than $F_\phi$ and the average over the momentum distribution will again result in a sech to leading order. For $\Phi_{nl} > \sqrt{n_0}$ the average over the momentum distribution will smear out the mean field in the same way as the enhanced phase fluctuations due to SPM do. This shows that quantum effects due to group velocity dispersion are equally important as the effect due to self phase modulation. As we have seen for $\Phi_{nl} \ll \sqrt{n_0}$ the phase and position spreading is negligible for the mean field which is then in leading order of $1/n_0$ that of the classical soliton.

For $\Phi_{nl} \ll \sqrt{n_0}$ we can expand $F_\phi$ in a Taylor series around $p_0$ and we can perform the remaining Gaussian integrals

$$< \psi(t)|\hat{\phi}(x)|\psi(t) >= \sum_{k=0}^{\infty} \frac{(2i\Phi_{nl})^k}{k!} H_\phi^{(k)}(x_{n_0}) F_\phi^{(k)}(x_{n_0}(p_0)) \tag{G.13}$$

with

$$H_\phi(x_{n_0}) = \frac{1}{\sqrt{1 + 2i\Phi_{nl}/(\mu n_0)}} \exp\left[-\frac{1}{2\mu n_0} \frac{x_{n_0}^2}{1 + 2i\Phi_{nl}/(\mu n_0)}\right] \tag{G.14}$$

The derivatives of $H_\phi$ with respect to $x_{n_0}$ scale like

$$H_\phi^{(k)} \approx 1/\sqrt{n_0}^k. \tag{G.15}$$

# Appendix H

# Second Order Correlation Functions

Analogously to Appendix G, we can compute the second order correlation functions by using the asymptotic expansion of the matrix elements (E.4), (E.5) and (E.11)

$$
\begin{aligned}
< \psi(t)|\hat{\phi}^{\dagger}(x)\hat{\phi}(x+\tau)|\psi(t) >= & \sum_{n=0}^{\infty} p_n \frac{n^2|c|}{4} \int dv\; g(v) e^{iv\tau} \\
& \left(1+\left(\frac{\mu}{4n_0}-\frac{1}{4n}\right)\frac{\partial^2}{\partial x_n^2}+O\left(\frac{1}{n^2}\right)\right) \\
\times & \left(\operatorname{sech}\left(x_n+\tau_n\right)\operatorname{sech}\left(x_n\right)+\frac{1}{2n}\left(|\tau_n|\cosh(\tau_n)-\sinh(|\tau_n|)\right)\operatorname{sech}^2\left(x_n\right)\operatorname{sech}^2\left(x_n+\tau_n\right)\right),
\end{aligned}
\tag{H.1}
$$

with $\tau_n = y_n - x_n$ and

$$
\begin{aligned}
< \psi(t)|\hat{\phi}(x)\hat{\phi}(x+\tau)|\psi(t) >= & \sum_{n=0}^{\infty} p_n \frac{n^2|c|}{4} \exp\left[i\frac{|c|^2}{2}n^2 t\right] \int dv g(v) e^{2iv(x-x_0+\tau/2)-2iv^2 t} \\
\times & \left(1-\frac{|\tau_n|}{n}+\left(\frac{\mu-4i\phi_{cl}/n_0}{8n_0}-\frac{1}{4n}\right)\frac{\partial^2}{\partial x_n^2}+O\left(\frac{1}{n^2}\right)\right) \\
\times & \left(\operatorname{sech}\left(x_n+\tau_n\right)\operatorname{sech}\left(x_n\right)+\frac{1}{2n}\left(|\tau_n|\cosh\left(\tau_n\right)-\sinh(|\tau_n|)\right)\operatorname{sech}^2\left(x_n\right)\operatorname{sech}^2\left(x_n+\tau_n\right)\right).
\end{aligned}
\tag{H.2}
$$

Using Poisson's sum formula from appendix F to perform the average over the photon number statistics results in

$$< \psi(t)|\hat{\phi}^{\dagger}(x)\hat{\phi}(x+\tau)|\psi(t) >= \int dv\, g(v) F_{\phi^*\phi}(x_{n_0}(v)) \tag{H.3}$$

for (H.1) with

$$F_{\phi^*\phi}(x_{n_0}) = f_{\phi^*\phi}(n_0) + \frac{n_0}{2} f^{(2)}_{\phi^*\phi}(n_0) \tag{H.4}$$

and

$$\begin{aligned} f_{\phi^*\phi}(n_0) &= \frac{n_0^2|c|}{4}\Bigg\{1 + \frac{\mu-2}{8n_0}\frac{\partial^2}{\partial x_n^2} \\ &+ \frac{1}{2n_0}(|\tau_{n_0}|\cosh(\tau_{n_0}) - \sinh(|\tau_{n_0}|)) \\ &\times \operatorname{sech}(x_{n_0}+\tau_{n_0})\operatorname{sech}(x_{n_0})\Bigg\} \\ &\times \operatorname{sech}(x_{n_0}+\tau_{n_0})\operatorname{sech}(x_{n_0}) \end{aligned} \tag{H.5}$$

with $\tau_{n_0} = y_{n_0} - x_{n_0}$. And

$$< \psi(t)|\hat{\phi}(x)\hat{\phi}(x+\tau)|\psi(t) >= \int dv\, g(v) F_{\phi\phi}(x_{n_0}(v)) \tag{H.6}$$

with

$$F_{\phi\phi}(x_{n_0}) = \sum_{k=0}^{2} G^{(k)}_{\phi\phi}(0) f^{(k)}_{\phi\phi}(n_0) \tag{H.7}$$

and

$$\begin{aligned} f_{\phi\phi}(n_0) &= \frac{n_0^2|c|}{4}\Bigg\{\left(1 + \frac{1-2|\tau_{n_0}|}{2n_0} + \frac{\mu-2+4i\Phi_{nl}/n_0}{8n_0}\frac{\partial^2}{\partial x_{n_0}^2}\right) + \frac{1}{2n}\Big(|\tau_{n_0}|\cosh(\tau_{n_0}) \\ &- \sinh(|\tau_{n_0}|)\Big)\operatorname{sech}(x_{n_0}+\tau_{n_0})\operatorname{sech}(x_{n_0})\Bigg\}\operatorname{sech}(x_{n_0}+\tau_{n_0})\operatorname{sech}(x_{n_0}) \end{aligned} \tag{H.8}$$

$$G_{\phi\phi}(y) = \frac{e^{2i\Phi_{nl}}}{\sqrt{1-4i\Phi_{nl}/n_0}} \exp\left\{-\frac{n_0}{2}\frac{(\frac{4\Phi_{nl}}{n_0}+y)^2}{1-4i\Phi_{nl}/n_0}\right\} \tag{H.9}$$

From those equations we can compute the noise covariances from definition (5.32).

# Bibliography


[1] W. Heisenberg, Z. Phys. **43**, 172 (1927)

[2] H. P. Yuen, "Two-photon coherent states of the radiation field", Phys. Rev. **A13**, 2226 (1976)

[3] R. E. Slusher, L. W. Hollberg, B. Yurke, D. C. Mertz, and J. F. Valley, "Observation of squeezed states generated by four-wave mixing in an optical cavity", Phys. Rev. Lett. **55**. 2409 (1985)

[4] D. F. Walls, "Squeezed states of the electromagnatic field", Nature, 324, 210 (1986)

[5] H. J. Kimble and D. F. Walls (guests eds.), *Special Issue on Squeezed States of the Electromagnetic Field*, J. Opt. Soc. Am. B4 1353-1741(1987)

[6] E. Giacobino and C. Fabre (guest eds.) *Special issue on Experimental Squeezing*, Appl. Phys. B**55**, 190-303 (1992)

[7] C. W. Gardiner, "Inhibition of phase decays by squeezed light: a direct effect of squeezing", Phys. Rev. Lett. **56**, 1917-1920 (1986)

[8] H. J. Carmichael, A. S. Lane and D. F. Walls, "Resonance-fluorescence from an atom in a squeezed vacuum", Phys. Rev. Lett. **58**, 2539-2542 (1987)

[9] A. S. Parkins, P. Zoller, and D. F. Walls, "Spectral linewidth narrowing in a strongly coupled atom-cavity system via squeezed light excitation of a vacuum Rabi resonance", Phys. Rev. A**48**, 758-763 (1993)

[10] S. Swain, "Anomalous resonance-fluorescence spectrum in a squeezed vacuum", Phys. Rev. Lett. **73**, 1493-1496 (1994)

[11] S. S. Hassan, O. M. Frege, N. Nayak, "Off-resonant squeezed vacuum effects on a driven two-level atom: absorption and intensity harmonics", J. Opt. Soc. Am. B**12**, 1177-1185 (1995)

[12] J. Gea-Banacloche, "Squeezing of spontaneous emission in a laser", Phys. Rev. Lett. **59**, 543-546 (1987)

[13] C. Ginzel, J. Gea-Banacloche, and A. Schenzle, "Linewidth of a laser with a squeezed reservoir", Phys. Rev. A**42**, 4164-4168 (1990)

[14] C. Ginzel, R. Schack, and A. Schenzle, "Dynamics and symmetry of a laser with a squeezed reservoir", J. Opt. Soc. Am. B**8**, 1704-1711 (1991)

[15] P. P. Rice, X. Yin, J. Walden, J. Gea-Banacloche, L. M. Pedrotti and J. E. Mullen, "Laser with injected squeezed vacuum: phase diffusion and intensity fluctuations", Phys. Rev. A**50**, 4176-4187 (1994)

[16] C. M. Caves, Phys. Rev. D**23**, 1693 (1981)

[17] M. Xiao, L.-A. Wu, and H. J. Kimble, "Precision measurement beyond the shot-noise limit" Phys. Rev. Lett. **59**, 278 (1987)

[18] P. Grangier, R. E. Slusher, B. Yurke, and A. LaPorta, "Squeezed-light-enhanced polarization interferometer", Phys. Rev. **59**, 2153-2156 (1987)

[19] M. Xiao, L.-A. Wu, and H. J. Kimble, "Detection of amplitude modulation with squeezed light for sensitivity beyond the shot-noise limit" Opt. Lett. **13**, 476 (1988)

[20] K. Bergman, C. R. Doerr, H. A. Haus, and M. Shirasaki, "Sub-shot-noise measurement with fiber-squeezed optical pulses", Opt. Lett., **18**, 643 (1993)

[21] B. Yurke, and E. A. Whittaker, "Squeezed-state-enhanced FM spectroscopy" Opt. Lett. **12**, 236-238 (1987)

[22] E. S. Polzik, J. Carri and H. J. Kimble, "Spectroscopy with squeezed light" Phys. Rev. Lett. **68**, 3020 (1992)

[23] M. I. Kolobov, and P. Kumar, "Sub-shot-noise microscopy: imaging of faint phase objects with squeezed light" Opt. Lett. **18**, 849-851 (1993)

[24] H. A. Haus, K. Bergman, and Y. Lai, "Fiber gyro with squeezed radiation", J. Opt. Soc. Am. B**8**, 1952-1957 (1991)

[25] C. R. Doerr, K. Tamura, M. Shirasaki, H. A. Haus, and E. P. Ippen, "Orthogonal polarization fiber gyroscope with increased stability and resolution", Appl. Opt. **33**, 8062-8068 (1994)

[26] R. Boyd, *Nonlinear Optics*, (Academic Press, New York, 1991)

[27] L.-A. Wu, H. J. Kimble, J. L. Hall, and H. Wu, "Generation of squeezed states by parametric down conversion", Phys. Rev. Lett. **57**, 2520-2523 (1986)

[28] C. Kim, and P. Kumar, "Quadrature squeezed light detection using a self-generated matched local oscillator", Phys. Rev. Lett. **73**, 1605-1608 (1994)

[29] A. Sizman, R. J. Horowicz, G. Wagner, and G. Leuchs, "Observation of amplitude squeezing of the up-converted mode in second harmonic generation", Opt. Comm. **80**, 138-142 (1990)

[30] D. F. Walls and G. J. Milburn, *Quantum Optics*, (Springer-Verlag, Berlin 1993)

[31] M. Shirasaki and H. A. Haus, "Squeezing of pulses in a nonlinear interferometer", J. Opt. Soc. Am. B**7**, 30 (1990)

[32] K. Bergman and H. A. Haus, "Squeezing in fibers with optical pulses", Opt. Lett., **16**, 663 (1991)

[33] K. Bergman, H. A. Haus, E. P. Ippen, and M. Shirasaki, "Squeezing in a fiber interferometer with a gigahertz pump", Opt. Lett., **19**, 290 (1994)

[34] M. Rosenbluh, and R. E. Shelby, "Squeezed optical solitons", Phys. Rev. Lett. **66**, 153-156, (1991)

[35] C. R. Doerr, I. Liubomirsky, G. Lenz, J. Paye, H. A. Haus, and M. Shirasaki, "Optical squeezing with a short fiber", in *Quantum Electronics and Laser Sciences*, Vol 12 of 1993 OSA Technical Digest Series (Optical Society of America, Washington, D. C., 1993), p.281

[36] X. Zhang, M. K. Udo and S. T. Ho, paper QFF3 in *Quantum Electronics and Laser Science Conference, Technical Digest*, page 283 (1993)

[37] T.-S. Ho, Y. Zhang, and M. K. Udo, "Single-beam squeezed state generation in semiconductor waveguides with $\xi^{(3)}$ nonlinearity at below half-band gap", J. Opt. Soc. Am. B**12**, 1537-1549 (1995)

[38] A.M. Fox, J. S. Braumberg, M. Dabbico, B. Huttner, and J. F. Ryan, "Squeezed light generation in semiconductors", Phys. Rev. Lett., **74**, 1728-1731 (1995)

[39] C. Cohen-Tannoudji, B. Diu, and F. Laloë, *Quantum Mechanics*, (Hermann, Paris 1977)

[40] R. J. Loudon, *The Quantum Theory of Light*, (Clarendon Press, Oxford, 1983)

[41] M. J. Sparnaay, Physica, **24**, 751 (1958)

[42] H. P. Yuen and V. W. S. Chan, "Noise in homodyne and heterodyne detection", Opt. Lett. **8**, 177-179 (1983)

[43] G. L Abbas, V. W. S. Chan, and T. K. Lee, "A dual-detector heterodyne receiver for local oscillator noise suppression", J. Ligthwave Techn. **LT-3**, 1110 (1985)

[44] W. K. Lai, V. Buzek and P. L. Knight, Phys. Rev A **43**, 6323 (1991)

[45] H. A. Haus, *Waves and Fields in Optoelectronics*, (Prentice Hall, Englewood Cliffs, 1984) p.65

[46] B. Yurke, "Wideband counting and homodyne detection", Phys. Rev. A**32**, 311-323 (1985)

[47] B. Yurke, P. Grangier, R. E. Slusher, and M. J. Potasek, "Generating and detecting short duration pulses of squeezed light", Phys. Rev **A35**, 3586-3589 (1987)

[48] M. Shirasaki, "Squeezing performance of a nonlinear symmetric Mach-Zehnder interferometer using forward degenerate four-wave mixing", J. Opt. Soc. Am. B8, 672-680, (1991)

[49] M. Shirasaki, "Quantum noise reduction in a phase-sensitive interferometer using nonclassical light produced through Kerr media", Opt. Lett., **16**, 171-173 (1991)

[50] M. Shirasaki, I. Lyubomirsky, and H. A. Haus, "Noise analysis of a Mach-Zehnder squeezer for nonclassical input states", J. Opt. Soc. Am B (1993)

[51] L. Boivin, "Sagnac-loop squeezer at zero dispersion with a finite response time for the Kerr nonlinearity", Phys. Rev. A**52**, 754 (1995)

[52] F. X. Kärtner, private communication.

[53] Y. Kodama and A. Hasegawa, "Nonlinear pulse propagation in monomode dielectric", IEEE, J. Quant. Elec., QE-**23**, 510-524 (1987)

[54] G. P. Agrawal, *Nonlinear Fiber Optics* (Academic Press, San Diego, 1989)

[55] A. C. Newell and J. V. Moloney, *Nonlinear Optics*, (Addison-Wesley, Redwood, 1992)

[56] H. A. Haus, E. P. Ippen and J. G. Fujimoto, "Structure for additive pulse modelocking", J. Opt. Soc. Am. B**16**, 1502 (1991)

[57] H. A. Haus, E. P. Ippen and J. G. Fujimoto, "Analytic theory of Kerr lens modelocking", J. Opt. Soc. Am. B**28**, 2086-2096 (1992)

[58] S. J. Carter, P. D. Drummond, M. D. Reid and R. M. Shelby, "Squeezing of quantum solitons", Phys. Rev. Lett. **58**, 1841 (1987).

[59] P. D. Drummond and S.J. Carter, "Quantum theory of squeezing in solitons", J. Opt. Soc. Am. **4**, 1565 (1987).

[60] H. A. Haus and Y. Lai, "Quantum theory of soliton squeezing: a linearized approach", Opt. Soc. Am B**7**, 386 (1990).

[61] A. Hasegawa and F. Tappert, Appl. Phys. Lett. **23**, 142 - 144 (1973).

[62] L. F. Mollenauer, R. H. Stolen and J. P. Gordon, Phys. Rev. Lett. **45**, (1980) 1095 - 1098.

[63] V. E. Zakharov and A. B. Shabat, "Exact theory of two-dimensional sel-focusing and one-dimensional self-phase modulation of waves in nonlinear media", Zh. Eksp. Teor. Fiz. **34**, 61 (1971), [Sov. Phys. - JETP **34**, 62 (1972).

[64] Y. Lai, "Quantum theory of soliton propagation: a unified approach based on the linearization approximation", J. Opt. Soc. Am. B**10**, 475-484 (1993)

[65] L. Boivin, F. X. Kärtner and H. A. Haus, "Analytical solution to the quantum field theory of self-phase modulation with a finite response time" Phys. Rev. Lett., **73**, 240 (1994)

[66] J. H. Shapiro and L. Boivin, "Raman noise limit for four-wave mixing", Opt. Lett. **18**, 925-927 (1994)

[67] R. N. Thurston, J. Sound Vib. **159**, 441 (1992)

[68] J. K. Bounds and H. A. Haus, "Quantum noise of Raman amplification", Quantum Opt. **6**, 79-85 (1994)

[69] T. Mizunami and K. Takagi, " Wavelength dependence of two-photon absorption properties of silica optical fibers", Opt. Lett., **19**, 463 (1994)

[70] M. Kitagawa and Y. Yamamoto, "Number-phase minimum uncertainty state with reduced number uncertainty in a Kerr nonlinear interferometer", Phys. Rev A**34**, 3974 (1986)

[71] R. K. John, J. H. Shapiro and P. Kumar, *XV International Conference on Quantum Electronics, 1987 Technical Digest* (Opt. Soc. Am., Washington D. C., 1987), p.204

[72] F. X. Kärtner, L. G. Joneckis and H. A. Haus, "Classical and quantum dynamics of a pulse in a dispersionless nonlinear fiber", Quantum Opt. **4**, 379 (1992)

[73] L. G. Joneckis and J. H. Shapiro, "Quantum propagation in a Kerr medium: lossless, dispersionless fiber", J. Opt. Soc. Am. B**10**, 1102 (1993)

[74] F. M. Mitschke and L. F. Mollenauer, "Discovery of the soliton self-frequency shift", Opt. Lett., **11**, 659 (1986)

[75] R. J. Glauber and M. Lewenstein, "Quantum optics of dielectric media", Phys. Rev. A **43**, 467 (1991)

[76] K. J. Blow, R. Loudon and S. J. D. Phoenix, "Exact solution for quantum self-phase modulation" J. Opt. Soc. Am. B**8**, 1750 (1991)

[77] K. J. Blow, R. Loudon and S. J. D. Phoenix, Phys. Rev. A**45**, 8064 (1992)

[78] F. X. Kärtner, D. J. Dougherty, H. A. Haus and E. P. Ippen, "Raman noise and soliton squeezing", J. Opt. Soc. Am., B**11**, 1275 (1994)

[79] R. H. Stolen and E. P. Ippen, Appl. Phys. Lett. **22**, 276 (1973)

[80] R. H. Stolen, J. P. Gordon, W. J. Tomlinson and H. A. Haus, "Raman response function of silica core fibers", J. Opt. Soc. Am. B**6**, 1159-1166 (1989)

[81] D. Dougherty, F. X. Kärtner, H. A. Haus and E. P. Ippen, "Measurement of the Raman gain of optical fibers", Opt. Lett. **19**, 31-35 (1995)

[82] A. Yariv, *Optical Electronics*, 4th edition, Chap. 10, (Saunders College Publishers, Orlando, 1991)

[83] W. H. Louisell, *Quantum Statistical Properties of Radiation*, (Wiley, New York, 1973)

[84] It is interesting to note that the linearized expressions for $F_1$ and $F_2$, when taken on their own, do not require a finite response time for the

Kerr nonlinearity. These functions being independent from $\tau_q$, they stay well defined when this time constant vanishes or, equivalently, when part of the nonlinearity is instantaneous, as in (4.75).

[85] P. D. Drummond and A. D. Hardman, "Simulation of quantum effects in Raman active waveguides", Europhys. Lett., **21**, 279 (1993)

[86] S. J. Carter and P. D. Drummond, "Squeezed quantum soliton and Raman noise", Phys. Rev. Lett., **67**, 3757 (1991)

[87] Y. Lai, "Quantum theory of soliton propagation: a unified approach based on the linearized approximation", **10**, 475-484 (1993)

[88] Y. Lai and S. S. Yu, "General quantum theory of nonlinear optical-pulse propagation", Phys. Rev. A**51**, 817-829(1994)

[89] D. Yevick and B. Hermansson, Opt. Commun. **47**, 101 (1983)

[90] H. E. Hernández-Figueroa, "Improved split-step schemes for nonlinear optical propagation", J. Opt. Soc. Am. B**11**, 798-803 (1994)

[91] C. R. Doerr, M. Shirasaki, F. I. Khatri "Simulation of pulsed squeezing in optical fiber with chromatic dispersion", J. Opt. Soc. Am. B, **11**, 143 (1994)

[92] L. Boivin, C. R. Doerr, K. Bergman and H. A. Haus, "Quantum noise reduction using a Sagnac loop with positive dispersion", in *Quantum Communications and Measurement*, edited by V. P. Belavkin, O. Hirota and R. L. Hudson, pp. 489-496 (Plenum Press, New York 1995)

[93] F. X. Kärtner and L. Boivin "Quantum Noise of the Fundamental Soliton", to appear in first issue of Phys. Rev. A**53** (1996)

[94] C. W. Gardiner, *Quantum Noise*, (Springer Verlag, Berlin 1992), p. 121-124.

[95] E. H. Lieb, and W. Linger, "Exact analysis of an interacting Bose gas I and II" Phys. Rev. **130**, 1605 (1961)

[96] I. B. McGuire, "Study of exactly solvable one dimensional n-body problems", J. Math. Phys. **5**, 622 (1964)

[97] C. N. Yang, "Some exact results for the many body problem in one dimension with repulsive delta-function interactions", Phys. Rev. Lett. **19**, 1312 (1967)

[98] C. N. Yang, "S matrix for the one-dimensional n-body problem with repulsive or attractive $\delta$-function interaction", Phys. Rev. **168** (1967)

[99] H. B. Thacker and D. Wilkinson, "Inverse scattering transform as an operator method in quantum field theory", Phys. Rev. D**19**, 3660 (1979).

[100] P. Garbaczewski, *Classical and Quantum Field Theory of Exactly Soluble Nonlinear Systems* (World Scientific, Singapore, 1985).

[101] C. R. Nohl, "Semiclassical quantization of the nonlinear Schrödinger equation", Ann. Phys. (N.Y.) **96**, 234 (1976).

[102] M. Wadachi and M. Sakagami, "Classical soliton as the limit of the quantum field theory", J. Phys. Soc. Japan **53**, 1933 (1984).

[103] Y. Lai and H.A. Haus, "Quantum theory of soliton in optical fibers I: time-dependent Hartree approximation", Phys. Rev. A**40**, 844 (1989)

[104] Y. Lai and H.A. Haus, "Quantum theory of soliton in optical fibers II: exact solution", Phys. Rev. A**40**, 854 (1989)

[105] F. X. Kärtner and H. A. Haus, "Correspondance principle for quantized solitons", Phys. Rev. A.**48**, 2361 (1993).

[106] F. Calogero and A. Degasperis, Phys. Rev. A **11**, 265 (1975).

[107] B. Yoon and J. W. Negele, "Time-dependent Hartree approximation for a one-dimensional system of bosons with attractive $\delta$-function interactions", Phys. Rev. A **16**, 1451 (1977).

[108] H. A. Haus and F. X. Kärtner, "Quantization of the nonlinear Schrödinger equation", Phys. Rev. A **46**, R1175 (1992).

[109] E. M. Wright, Phys. Rev. A**43**, 3836 (1989).

[110] I. G. Gochev and V. J. Draganova, Phys. Rev. A**49**, 5139 (1994).

[111] M. Abramowitz and I. A. Stegun, Handbook of Mathematical Functions, Dover publications, Inc. New York, p.257 (1965).

[112] I. S. Gradshteyn and I. M. Ryshik, Tables of integrals series and products, Academic Press (1980).

[113] R. Courant and D. Hilbert, Mathematische Methoden der Physik I, Berlin, Springer, p.64 (1968).

[114] L. Boivin and H. A. Haus, "$\chi^{(3)}$-Squeezed vacuum generation without a Sagnac interferometer", Opt. Lett., **21**, January 15 (1996)

[115] R. M. Shelby, M. D. Levenson and P. W. Bayer, "Guided acoustic wave Brillouin scattering", Phys. Rev. B**31**, 5244-5252 (1985)

[116] K. Bergman et al., "Analysis and measurement of GAWBS spectrum in a nonlinear fiber ring" Appl. Phys. B**55**, 242-249 (1992)

[117] N. Nishizawa, S Kume, M. Mori and T. Goto, "Experimental analysis of guided acoustic wave Brillouin scattering in PANDA fibers", J. Opt. Soc. Am. B**12**, 1651-1655 (1995)

[118] G. Lenz *et al.* , "Stretched-pulse mode-locked erbium-fiber laser amplified by KCl:$TI^{+}$ color center crystals", in *Technical Digest, CLEO 1995*, **15**, paper CWI3, p.237 (1995)

[119] J. T. Chen, Q. D. Liu, P. P. Ho, and R. R. Alfano, "Comparison of nonlinear effect of linearly and circularly polarized picosecond pulses propagating in optical fibers", J. Opt. Soc. Am. B**12**, 907 (1995)

[120] M. Born, and E. Wolf, *Principles of Optics* (Pergamon, Oxford 1990)

[121] S. Alexander, "Design of a wide band heterodyne balanced mixer receiver", J. Lightwave Techn. LT-**5**, 523-537 (1991)

[122] M. Paye-Ramaswamy and J. G. Fujimoto, "Compact dispersin compensated geometry for Kerr-lens modelocked lasers", Opt. Lett **19**, 590 (1994)

[123] K. J. Blow, R. Loudon, and S. J. D. Phoenix, "Continuum fields in quantum optics", Phys. Rev. A **42**, 4102-4114, (1990)

[124] F. Matera, A. Mecozzi, and M. Settembre, "Light depolarization owing to ASE and Kerr nonlinearity in long-haul fiber links close to zero-dispersion", Opt. Lett. **20**, 1465 (1995)

[125] A. Owyoung, R. W. Hellwarth, and N. George, Phys. Rev. B**5**, 628 (1972)

[126] R. W. Hellwarth, J. Cherlow and T.-T. Yang, Phys. Rev. B**11**, 964 (1975)

[127] H. G. Winful, "Self-induced polarization changes in birefringent optical fibers", Appl. Phys. Lett. **47**, 213 (1985);

[128] For example the *3M Technical Overview and Product Catalog* indicates that the FS-LB-3211 fiber has a beat length of more that $36m$.